



HAL
open science

Elasticity of self assembling bio-materials

Hugo Le Roy

► **To cite this version:**

Hugo Le Roy. Elasticity of self assembling bio-materials. Biological Physics [physics.bio-ph]. Université Paris-Saclay, 2021. English. NNT : 2021UPASP097 . tel-03416951

HAL Id: tel-03416951

<https://theses.hal.science/tel-03416951>

Submitted on 5 Nov 2021

HAL is a multi-disciplinary open access archive for the deposit and dissemination of scientific research documents, whether they are published or not. The documents may come from teaching and research institutions in France or abroad, or from public or private research centers.

L'archive ouverte pluridisciplinaire **HAL**, est destinée au dépôt et à la diffusion de documents scientifiques de niveau recherche, publiés ou non, émanant des établissements d'enseignement et de recherche français ou étrangers, des laboratoires publics ou privés.

Thèse de doctorat de l'Université Paris-Saclay

École doctorale n° 564, Physique en Île-de-France

Spécialité de doctorat: Physique

Unité de recherche: Université Paris-Saclay, CNRS, LPTMS, 91405, Orsay, France

Référent : Faculté des sciences d'Orsay

Thèse présentée et soutenue à Paris-Saclay
le 04/10/2021

Hugo LE ROY

Composition du jury

Emmanuel TRIZAC

Professeur, LPTMS

Greg GRASON

Professeur, University of Massachusetts Amherst

Emanuela ZACCARELLI

Professeure, CNR ISC

Thibaut DIVOUX

Chargé de recherche CNRS, ENS Lyon

Zorana ZERAVCIC

Maitre de conférence ESPCI

Président

Rapporteur & Examineur

Rapporteuse & Examinatrice

Examineur

Examinatrice

Direction de la thèse

Martin LENZ

Directeur de recherche CNRS, Université Paris-Saclay

Directeur

Élasticité des bio-matériaux auto assemblés

Hugo Le Roy

October 2021

Dans cette thèse, nous étudions les interactions entre les propriétés mécaniques des matériaux biologiques et leur organisation. En effet, les systèmes biologiques régulent leur forme ainsi que leur taille, eux même. Cette régulation peut se faire grâce à un réseau de réactions chimiques interdépendantes, l'expression de gènes ou grâce à des communications mécaniques appelées allostérie. En outre, les propriétés mécaniques des matériaux biologiques dépendent aussi de leur structure. Ici, nous étudions des hydrogels synthétiques inspirés de la colle synthétisée par les moules. Les moules peuvent se coller à quasiment n'importe quel surface, et en particulier sous l'eau. En y regardant de plus près, cette colle est en fait un hydrogel fait de chaînes polymériques que l'on retrouve dans la plupart des hydrogels, liés entre eux par des ions métalliques. Nous étudions l'influence du nombre de polymères qui peuvent se fixer à un ion, appelé valence, sur la réponse mécanique d'un tel gel.

1 Influence de l'élasticité sur l'auto-assemblage de particules géométriquement frustrées.

Les systèmes biologiques ont une remarquable capacité d'auto-organisation. Les protéines, par exemple, sont repliées de multiples fois de manière très contrôlée avant de s'assembler entre elles sous forme de complexe. La moindre erreur dans ce processus engendre des maladies telles qu'Alzheimer ou Parkinson. Parmi les mécanismes qui permettent le contrôle de la taille et de la forme de la machinerie cellulaire, nous étudions ici l'influence de l'élasticité des particules qui composent un agrégat. Plus précisément, nous considérons ici l'assemblage de particules dont la forme n'est pas optimisée pour s'emboîter les unes dans les autres. Ce genre d'incompatibilité géométrique est connu comme participant à la régulation de la taille de ballot de fibre par exemple. Plus récemment il a été montré que ce type de mécanisme peut aussi entraîner la formation d'agrégat fibreux, alors même que les particules qui le composent, ont une forme sans symétrie particulière.

Les particules auto-assemblées sont modélisées par une forme géométrique simple comme représenté Fig 1 (a). L'élasticité de ces particules est modélisé par des ressorts linéaires représentés Fig 1 (b). Leur forme ne leur permet pas de s'agréger sans se déformer comme représenter Fig 1 (c). Finalement lorsque

ces particules forment un agrégat macroscopique, elles doivent nécessairement se déformer en un hexagone régulier représenté Fig 1 (d). L'agrégation de ces particules est favorisée par l'ajout d'une énergie de tension de surface qui correspond à un coût énergétique constant pour chaque côté d'hexagone libre noté : J . Notre étude tente principalement de déterminer la forme ainsi que la taille

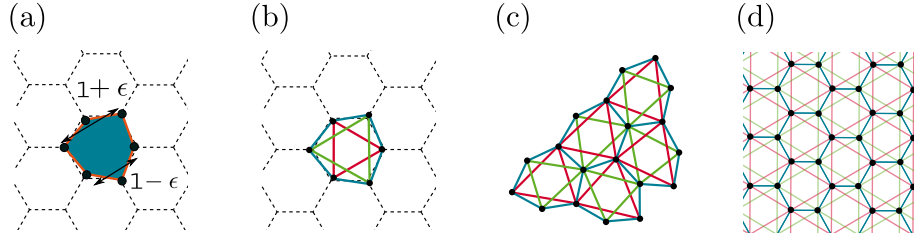


Figure 1: **Modèle de particules hexagonales :** (a) Les particules ont la forme d'un hexagone déformé, obtenu en déplaçant les nœuds (points noirs). ϵ quantifie l'inadéquation entre les différentes particules. La position des particules est repérée sur un réseau hexagonal qui apparaît en pointillé (b) Chaque ligne est un ressort qui permet de modéliser l'élasticité de la particule. (b) L'agrégation de plusieurs de ces particules engendre une déformation élastique. (c) La seule forme que peuvent adopter ces particules dans un large agrégat est celle d'un hexagone régulier appelé configuration de masse.

des agrégats formés à l'équilibre thermodynamique à partir de la connaissance des caractéristiques mécaniques des particules individuelles. De tels exemples sont représentés Fig 2. Chaque forme et taille représente un différent compromis entre la tension de surface et la frustration géométrique. Au cours de cette étude, nous avons pu dériver une version continue de ce modèle de particules frustré. Cette approximation continue nous a permis de calculer analytiquement l'énergie de plusieurs ansatz de forme tels que des disques ou des fibres. Nous avons identifié les deux paramètres importants de ce problème qui permettent de distinguer quel forme est la plus stable : le coefficient de Poisson ν et la tension de surface, écrite sans unité Γ . Un diagramme de phase récapitule les domaines pour lesquels les fibres, ou les disques sont les plus stables, représenté Fig 3. En plus de cette analyse basée sur la comparaison d'Ansatz de forme, nous avons utilisé une méthode d'optimisation sans biais : simulation de recuit Monte-Carlo. Cette méthode permet de trouver une estimation de l'état fondamental de notre système en simulant les propriétés thermodynamique d'un gaz de particules et en diminuant progressivement la température. Au fur et à mesure que la température diminue, l'énergie du système diminue elle aussi, jusqu'à atteindre l'état fondamental. En combinant ces deux méthodes, nous pouvons confirmer deux principaux phénomènes émergents de la frustration géométrique. Tout d'abord, l'émergence d'une échelle caractéristique qui fixe la taille d'agrégat de taille finie. Ensuite la mise en évidence de l'importance de la compressibilité des particules auto-assemblées, à travers le coefficient de Poisson.

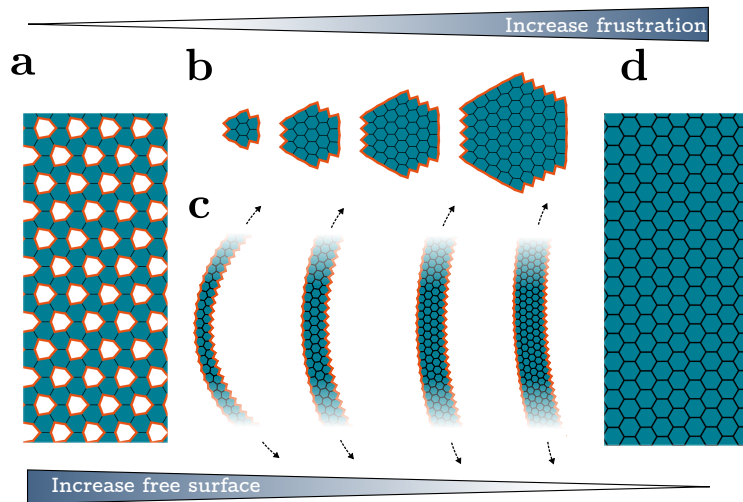


Figure 2: **Exemples d'agrégats** : (a) agrégat macroscopique lacunaire. Il est possible d'assembler un tel agrégat sans déformer les particules. Les côtés d'hexagones libres sont représentés par une ligne orange. (b) exemples de disques de tailles finis. (c) exemples de fibres, de différentes épaisseurs. (d) Agrégat de taille macroscopique.

Ce modèle de particule auto-assemblées frustrées permet de mettre en évidence des mécanismes simples à l'application vaste concernant l'assemblage de particules aux formes non-optimisées. En utilisant un modèle d'élasticité linéaire simplifié nous avons pu déterminer les caractéristiques mécaniques importantes pour déterminer la forme de l'agrégat final. Bien que simplifié, le modèle produit des résultats qui ne dépendent pas des spécificités du modèle. Dans le dernier chapitre de cette première partie, nous proposons une manière d'étendre l'application de nos résultats en utilisant des particules dont les propriétés mécaniques sont générées de manière aléatoire.

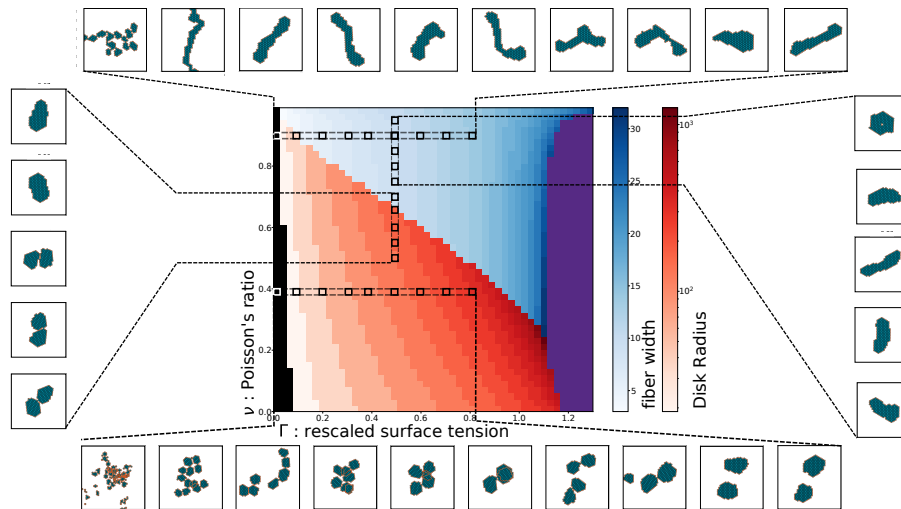


Figure 3: **Diagramme de phase** : les régions de différentes couleurs représente les domaines de stabilité de chaque forme. bleu correspond aux fibres, rouge aux disques, violet agrégat macroscopique, noir agrégat macroscopique lacunaire. Les images autour du diagramme de phase correspondent aux simulations de recuit Monte-Carlo qui attestent de la cohérence avec le diagramme de phase.

2 Contrôler la relaxation non-exponentielle des contraintes dans les hydrogels.

Un hydrogel est un réseau de polymères hydrophiles connectés entre eux. Un tel réseau absorbe et gonfle au contact d'eau, créant ainsi un hydrogel composé majoritairement d'eau. Les hydrogels sont généralement des matériaux viscoélastiques. L'élasticité entropique des polymères confère au matériau son aspect solide, tandis que la reptation des polymères entre eux permet un comportement liquide. Dans notre situation, on considère des polymères connectés par des liens éphémères à des ions. Ainsi, la relaxation des contraintes dans le gel est dû à la dynamique de déconnexion, relaxation, reconnexion des polymères avec les ions. Nous étudions trois gels, chacun fabriqué à partir d'ions différents, comme représenter Fig 4. Pour sonder la réponse mécanique de ces systèmes,

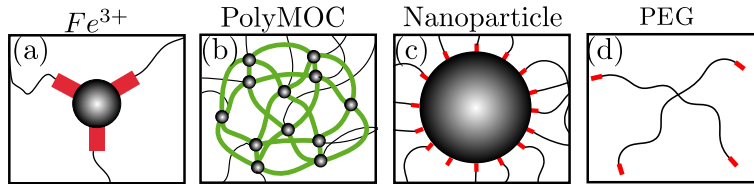


Figure 4: **Constituants du gel** :(a) ion Fe^{3+} sur lequel trois polymères peuvent s'attacher. (b) Nanocages, aussi appelé PolyMOC (polymer metal-organic cages) de valence 14. (c) Nanoparticule d'oxyde de fer, sur lesquels environ 80 polymères peuvent s'attacher. (d) Polymères en étoile, qui constituent le réseau du gel.

des collaborateurs du MIT ont effectués des mesures d'échelon de déformation. En utilisant un rhéomètre, ils appliquent une déformation constante au gel et mesure la contrainte résultante. De part, le caractère viscoélastique du gel, la contrainte diminue avec le temps. Dans le cas des hydrogels connectés par des ions à faible valence, la contrainte dans le matériau relaxe selon une exponentielle simple avec un temps de relaxation caractéristique correspondant au temps de déconnexion des polymères. Cependant, dans le cas des gels connectés par des ions à large valence, d'une part la relaxation n'a rien d'exponentielle et d'autre part, le temps de relaxation augmente de plusieurs ordres de grandeurs.

Pour comprendre ce phénomène, on considère un mécanisme microscopique de relaxation des contraintes centré autour de la connexion entre deux ions. Pour que deux ions puissent diffuser librement, il ne doit y avoir aucune connexion entre les deux. Dans le cas de deux ions connectés par un lien unique, le temps nécessaire à leur diffusion mutuel correspond au temps de déconnexion du lien. Dans le cas de deux ions connectés par plusieurs liens, alors on peut montrer que le temps nécessaire à leur diffusion mutuel s'écrit :

$$\tau_N \propto \frac{1}{N p_{\text{off}}^N} \quad (1)$$

avec p_{off} la probabilité pour chacun des liens uniques d'être déconnecté et N le nombre de liens qui lient les deux ions.

à l'aide de ce mécanisme microscopique de relaxation nous sommes capable de dériver une fonction analytique pour la relaxation d'hydrogels connectés par de multiples liens. La cohérence entre les expériences effectués par nos collaborateurs, et notre modèle est illustrés Fig 5

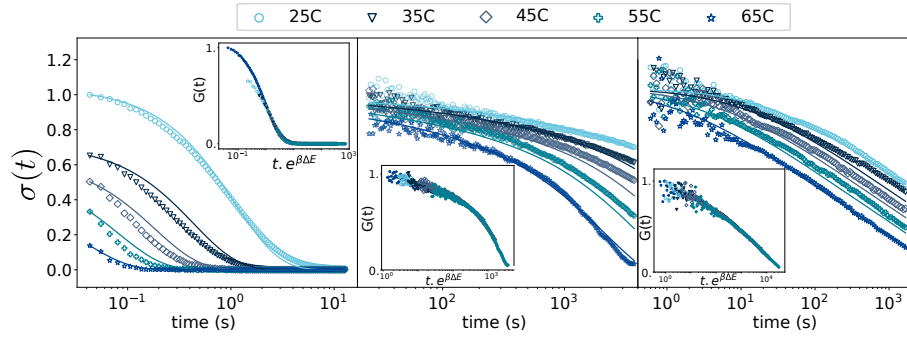


Figure 5: **Courbes de relaxations** : De la gauche à la droite : Fe^{3+} , PolyMOC, Nanoparticules. Les inserts montrent qu'il est possible de changer l'échelle de temps de manière à compresser les courbe de relaxations effectués à différentes températures en une unique courbe maitresse. Ce type de compression montre qu'une unique échelle d'énergie est impliqué dans le processus et soutient notre mécanisme.

Contents

I	Frustrated assembly	7
1	Introduction to self-assembly	9
1.1	Microscopic self-assembling systems	10
1.1.1	Assembly of protein complex	10
1.1.2	Assembly of virus capsid	10
1.1.3	Engineering specific interactions	12
1.2	Finite-size self-assembly	14
1.2.1	Thermodynamics of micelle assembly	15
1.2.2	Patchy particles model	16
1.2.3	Short-range attractive, long-range repulsive colloids	17
1.3	Frustrated self-assembly	20
1.3.1	Blue phase liquid crystal	20
1.3.2	Crystallization on a curved space	20
1.3.3	Modeling the frustration	23
1.4	Objectives	25
2	Model of assembling particles	29
2.1	Choosing the correct shape	30
2.1.1	Pentagon case	30
2.1.2	Lattice-inspired irregular particle	32
2.2	Full computation of the squared model	36
2.2.1	Continuum limit	37
2.2.2	Equilibrium limited size assembly	39
2.3	Continuum model	41
3	Shape Ansatz phase diagram	45
3.1	Mapping of the parameters	45
3.2	The algorithm	47
3.2.1	Topology relation	47
3.2.2	Equilibration of an aggregate	48
3.3	Discrete Ansatz of shape	50

3.3.1	Continuum disk to discrete hexagon	50
3.3.2	Numerical infinite fiber	50
3.3.3	Sparse bulks	52
3.4	Phase diagram	52
4	Monte-Carlo simulated annealing	55
4.1	About simulated annealing in general	56
4.2	Implementation of the simulated annealing	57
4.3	Restricting the phase space to improve efficiency	58
4.4	Comparing Monte-Carlo results and shape Ansätze	60
4.4.1	Increase in radius with Γ	60
4.4.2	Increase in width with Γ	63
4.4.3	Increase in anisotropy with ν	64
5	Mechanisms that stabilize assembly	67
5.1	A more general model: the random hexagons	68
5.2	On the boundary layer of stress relaxation	70
5.2.1	Measuring the boundary layer	70
5.2.2	Correlation with the equilibrium size	72
5.3	Mechanisms that stabilize the fibers	75
II	Non-exponential relaxation	81
6	Introduction to hydrogels	83
6.1	The hydrogel family	83
6.2	Experimental setup	84
6.3	Model for viscoelastic relaxation of transient hydrogels	86
6.3.1	Maxwellian relaxation	86
6.3.2	Ideal network theory	87
6.3.3	Stretched exponential relaxation	88
7	Modeling of the microscopic relaxation process	91
7.1	Dynamic of a single bond	91
7.2	A collection of single bonds: the superbond	92
7.3	Computation of the survival probability of a superbond	95
7.3.1	Quick argument	95
7.3.2	Numerical argument	96
7.4	Calculation of $\bar{\tau}(N)$	97

8	Two mechanisms can limit a super-bond lifetime	101
8.1	Polymer availability limitation	101
8.2	Valency limitation	102
8.3	Derivation of the relaxation modulus	103
8.4	The $\alpha(T)$ paradox	107
8.5	About power-law stress relaxation	107
9	Comparison with the experiment	111
9.1	Valency and N_{cut}	111
9.2	Collapsing of the relaxation curves	112
9.3	Fit the master curve	114

Introduction

Living organisms that we observe today are the result of millions of years of evolution. From this perspective, it is natural to consider them as a gigantic source of inspiration. Engineering, for instance, often follows the path traced by our growing understanding of living systems. While we may be impressed by our progress to understand and mimic biological systems, we must also focus our attention on our limits in this domain. Even everyday materials such as leather are yet to have a synthetic rival to their flexibility, robustness, and longevity. Living matter is extremely exotic to some extent. It is both fluid and solid. It is disordered in an organized fashion but also durable while constantly reshaping. In this thesis, we study the interplay between the mechanical response of living matter and its organization. Clearly, the microscopic structure of a material determines its mechanical properties, but more interestingly, living systems also use mechanics to self-organize. This document is articulated around two major projects that each tackle one of the two ways of this interplay. In the first part, we study how mechanics control self-assembly by focusing on the role of geometric frustration. We use a coarse-grained model of ill-fitting particles to investigate the influence of mechanical properties of the assembling units on the resulting aggregate structure. In the second part, we study the macroscopic effect of a specific microscopic organization by looking at the mechanical relaxation of a hydrogel. This project is the result of a collaboration with an experimental team that is able to synthesize hydrogels with remarkable rheological properties, the origins of which remain unclear. We designed a model using simple tools from statistical physics to provide practical answers to fundamental questions.

Part I

Part I : Elastically frustrated self-assembly of protein-like particles

Chapter 1

Introduction to self-assembly

Living systems demonstrate a remarkable ability to self-organize. From the scale of a protein that must be folded multiple times in a precise way, up to the control of tissue growth. Any mistake can lead to serious disease in the case of protein misfolding [1], or cancer proliferation in the case of unregulated tissue growth. The regulation of the size, shape, or gene expression of multicellular organisms can be achieved through complex networks of interlinked chemical reactions. Concerning the organization of elements of the size of the order of a molecule, they have to obey simpler physics laws. Nonetheless, even at the nanoscale, living systems display a wide variety of structures with different symmetries, ranging from the filaments of the cell – actin, microtubules, intermediate filaments – to empty shells of virus capsids or even molecular motors like myosin. In this first part of the thesis, we consider the self-assembly of microscopic elements of the size of a large molecule, such as a protein or a small colloid. Our goal is to derive general guiding principles for the assembly of simple objects. This is why our approach focuses on equilibrium self-assembly processes. At this scale, electrostatics and Van der Waals interactions, or chemical bonds, are responsible for the cohesion of the particles. In addition, the geometry of the assembling particles imposes a local order that propagates at a larger scale, similar to liquid crystals.

Sometimes, however, self-assembly fails and the self-assembling process occurs in a non-optimal way. In this part, we are interested in this non-optimal assembly. The first chapter starts by defining the microscopic objects we will study in section 1.1. We then state the meaning of “non-optimal assembly” by defining frustration in self-assembling systems in section 1.3. Throughout the thesis, we will see that remarkable phenomena emerge from the frustration. To properly understand why these phenomena are interesting, we introduce the usual theory of equilibrium micelle assembly in section 1.2, and then review a few existing models in which similar behavior has been observed.

1.1 Microscopic self-assembling systems

Here we start by introducing the type of system that we will study. Starting with proteins and their structures section 1.1.1, we then explain how they can create large structures with the example of virus capsid 1.1.2. Finally, we look at the nanoengineering techniques used to create specific interactions between self-assembling particles section 1.1.3.

1.1.1 Assembly of protein complex

Proteins are the carrier of most cellular mechanisms. They are macromolecules organized at several scales. The first scale, known as the primary structure, is a sequence of amino acids bound together by peptide bonds. This sequence then usually folds into secondary structures that are either β -sheet or α -helix, which are two ways of optimizing hydrogen bonding between the amino acids of a protein. Non-specific hydrophobic interactions then lead a given sequence to fold several β -sheets and α -helices together to form the tertiary structure of a protein. Finally, several polypeptide chains usually assemble to form a complex called quaternary structure. The quaternary structure of a protein is a way to create an object with a fixed symmetry. Fig 1.1 (a) illustrates how to create 2-fold, 3-fold symmetric objects or helical structures with multiple copies of the same protein. Going one step further Fig 1.1 (b) shows the larger symmetry group accessible by using several polypeptide chains in the same complex. The stability of such complexes, sometimes made of a few dozens of proteins, is not due to a single cohesive energy. Instead, specific regions of a protein share affinity: hydrophobicity or disulfide bonds.

1.1.2 Assembly of virus capsid

Going one step further in the complexity of assembling proteins, we now look at the assembly of virus capsids. Viruses encapsulate their genetic code – RNA or DNA– into a viral capsid Fig 1.2. A viral capsid is a closed structure of proteins whose synthesis is triggered by the virus in the infected cell.

Viral capsids are a great example of a simple self-assembling system in biology. Most capsids that have been observed exhibit icosahedral symmetry. The ubiquity of icosahedral symmetry can be understood with the Caspar-Klug theory. It shows how it is possible to create various types of icosahedron using only a limited number of nonequivalent particles [5]. In vitro experiments have shown that the assembly of certain capsids happens spontaneously whenever the components are in solution [6]. This shows that the assembly of viral capsids occurs at equilibrium, although it is not a reversible process. To understand this, a simple model has been introduced

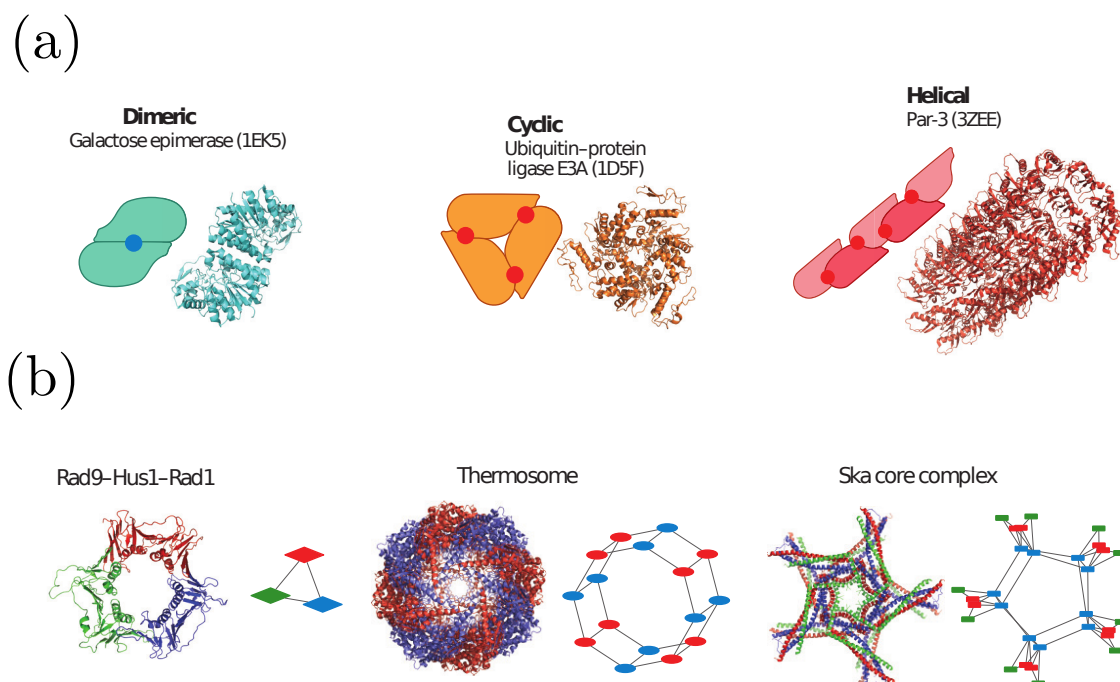


Figure 1.1: **Example of protein quaternary structure** : (a) three complexes made of copy of one type of protein, with different symmetry. The blue/red dots are interactions points - blue when the same region of the proteins interact together twice and red when two distinct parts of the protein interact. (b) three complexes made of several proteins, that give rise to different symmetries. adapted from [2]

[7], which gives a first answer to the irreversible nature of this type of assembly. Fig 1.3 illustrates the sequential assembly of a dodecahedral shell. The mechanism can easily be generalized to an icosahedron. We notice that the final steps of the assembly are very favorable, almost irreversible. If ϵ was too high – as compared to $k_B T$ –, the assembly could be stuck in a bad configuration. The high value of the interaction energy would not allow for thermal equilibration to converge to the optimal structure. Instead, it is only whenever the dodecahedron fully completes itself that the reaction becomes irreversible. Such a process still requires the first 9-10 steps to occur. An even bigger virus would require many more preliminary steps before the assembly turns into an irreversible process.

More recent works [8] suggest that the assembly of a capsid can be followed by a maturation process. It consists in a conformational change of the protein constituting the virus capsid that changes their interaction energy and locks the assembly. However, for such a process to happen, the information of the completion of the capsid must propagate to each protein. This type of maturation process also

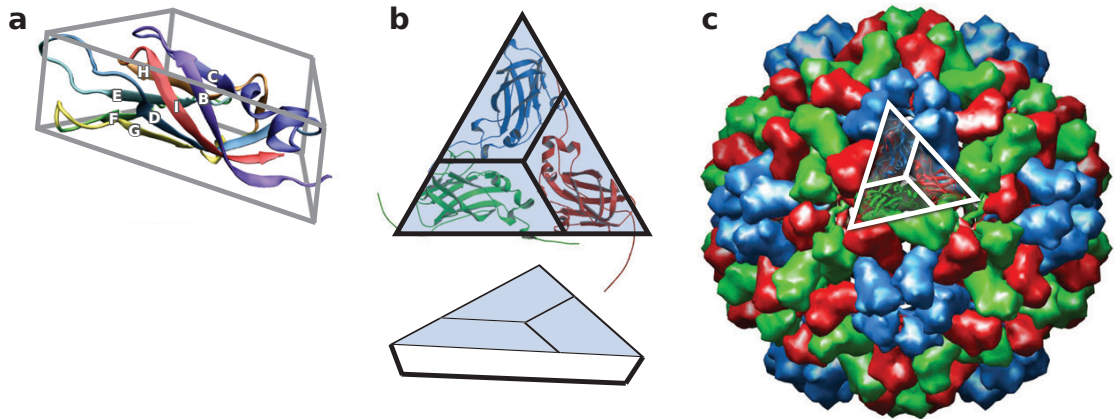


Figure 1.2: **Example of viral capsid** : (a) folded capsid protein, the trapezoidal shape of the protein creates. (b) The triangular subunit of the virus capsid -here *Cowpea chlorotic mottle virus*. the triangle subunit has no up-down symmetry, which creates a curved surface when assembled. (c) Viral capsid fully assembled. Adapted from [3] and [4]

happens in protein assembly [2] and is called allostery. Allostery is the transmission of information through a protein or a complex of proteins by the propagation of a mechanical deformation. To successfully transmit the message, the mechanical stiffness of the protein complex must be fine-tuned [9]. This suggests that biological systems not only have to regulate their shape, but also have to exert a tight control over the mechanical properties of their constituents.

1.1.3 Engineering specific interactions

Modern techniques have enabled the design of nanostructures with exceptional control over their shape and size. This includes techniques using coiled-coil peptide modules [10], or single DNA strands for DNA origami [11, 12] that are great examples of state-of-the-art technology. In this section, we present one experimental strategy to synthesize controllable self-assembling units: the design of specific interactions using DNA-coated droplets. Unlike DNA origami, or the assembly of viral capsids, DNA coated droplet interactions are isotropic. DNA coated droplets use mobile single strand DNA that are grafted onto a droplet or a colloid of a few micrometers in size to induce short-range, specific interactions with the complementary strands [13, 14], as shown in Fig 1.4. Being able to design an arbitrary number of specific attractive interactions is, however, not sufficient to build any target structure. Let us consider a specific arrangement of neighboring droplets that we call a target structure. It is defined by a binary adjacency matrix, whose

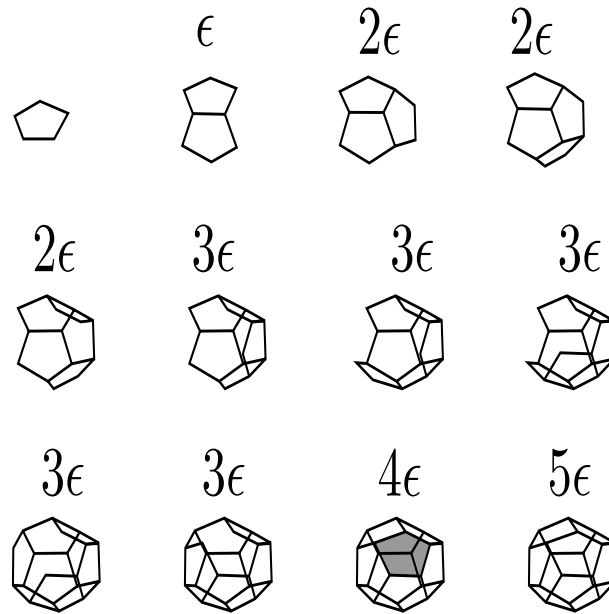


Figure 1.3: **Assembly of a dodecahedral virus capsid** : the shell is made of pentagons that are being added one by one. The energetic gain for sticking two edges together is constant and equal to ϵ . As the assembly takes place and the dodecahedron closes itself, the energetic gain for adding a pentagon increases, which stabilizes the final closed shell. Adapted from [7].

entries are A_{ij} . If the particles i and j are neighbors, then $A_{ij} = 1$, otherwise $A_{ij} = 0$. If A is an irreducible matrix, then it defines a unique arrangement of neighboring particles up to its mirror symmetry. From this, it is possible to design a set of specific interactions for which this arrangement of droplets is the ground state. Because the interaction between droplets only depends on the neighboring droplet and not the orientation, such a set of interactions can be represented as an interaction matrix: E . The entries E_{ij} of the interaction matrix are the interaction's energies between the particles i and j . To achieve a target structure with high yield, we must think of fine-tuning the strength of each interaction. On the one hand, having an interaction energy -in the unit of $k_B T$ - too high could trap the system into any undesired local minimum. On the other hand, a too low interaction energy would not allow for a steady final structure. The assembly process would be followed by a disassembly. Therefore, this strategy works to achieve target structure made of a few hundreds of particles [15]. Ultimately, however, the number of undesired structures that are a local minimum of energy grows rapidly with the total number of particles. This effect imposes a limit on the size of the structure that can be assembled using only isotropic specific interactions. Now

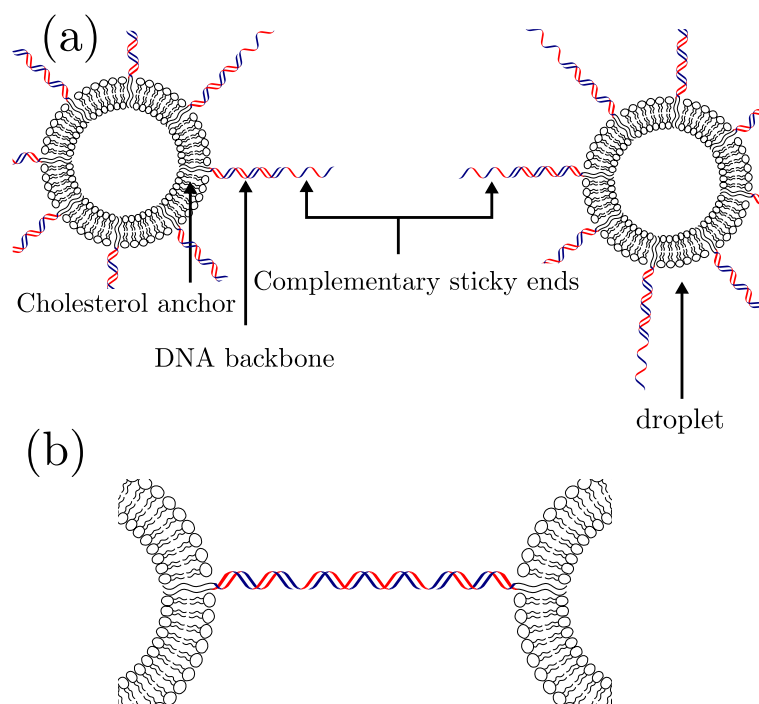


Figure 1.4: **DNA coating technique** : (a) two lipid droplets are being coated with DNA strands. A single DNA strand is attached to a DNA backbone -double strand- which is then attached to a cholesterol end. The cholesterol end can be integrated into the lipidic droplet, which makes DNA strands mobile on the surface of the droplet. (b) Binding of two complementary sticky ends. It is possible to synthesize a selected sequence of the sticky end. Only strands that have complementary interactions can bind together making it possible to create multiple selective interactions between droplets.

that we have introduced the type of objects we are going to study, let us be more specific about the type of assembling mechanism that we are going to be interested in.

1.2 Finite-size self-assembly

Living systems have the ability to self-regulate their size. To understand how this is possible, we start by introducing a naive model of self-assembly in section 1.2.1, that shows how self-limited aggregation is not trivial. We then look at two slightly more elaborate models that display self-limited aggregation, starting by using interactions with a specific geometry in section 1.2.2. We then study an interaction potential made of two components: a short-range attractive and a long-range re-

pulsive one in section 1.2.3. Using simple scaling laws, we show how self-limited aggregation can emerge.

1.2.1 Thermodynamics of micelle assembly

Here, we present the usual theory that describes the thermodynamics of micelle self-assembly [16, 17]. However, we consider here a more general situation. Let us consider anisotropic particles in solution that interact through an attractive short-range interaction. The attractive interaction eventually leads them to stick together and form an aggregate. We model the interaction as a fixed energy decrease whenever two particles are in contact. The energy of an aggregate made of n particles is denoted $E(n)$. In the middle of an aggregate, a given particle benefits from the interactions with each of its neighbors. We denote $-e_\infty$ the energy of a particle in the middle of an aggregate. The interaction is attractive, so $e_\infty > 0$. The particles that are at the surface of the aggregate do not interact with as many neighbors as the ones in the middle. This introduces an energetic cost for the interface between the aggregate and the solution, just like a surface tension. Typically, when forming a 3D anisotropic spherical aggregate, the function $E(n)$ takes the form :

$$E(n) = ne(n) = n \left(-e_\infty + \frac{n^{2/3}\delta e}{n} \right) = n \left(-e_\infty + \frac{\delta e}{n^{1/3}} \right) \quad (1.1)$$

δe is the cost for a particle to be at the border of the aggregate. The number of particles that are on the border of the aggregate is proportional to its surface: $n^{2/3}$. We denote the volume fraction of aggregates that contains n particles by $C(n)$. In the ideal/dilute solution approximation, we can write the free energy of the system per volume unit :

$$\frac{F}{V/v_0} = \sum_{n=1}^{\infty} E(n)C(n) + C(n)/\beta \{ \ln[C(n)] - 1 \} + \mu \left(\sum_{n=1}^{\infty} nC(n) - \mathbf{C} \right) \quad (1.2)$$

where v_0 is the volume of a single particle, and $\beta = 1/(k_B T)$ the inverse temperature. The first term is the energy of the aggregates and the second term is the translational entropy of the aggregates (assuming that the aggregates do not interact with each other). The last term ensures a fixed total volume fraction of particle of \mathbf{C} with μ the associated Lagrange multiplier. Minimizing the free energy of the system with respect to each aggregate volume fraction $C(n)$ leads to :

$$\forall n \in \mathbb{N} \quad \frac{\partial F/V}{\partial C(n)} = 0 \Leftrightarrow C(n) = \exp [\beta(-E(n) + \mu n)] = C(1)^n e^{-\beta E(n)} \quad (1.3)$$

Here we set the energy of the single particle: $E(1) = 0$. Using Eq (1.1), we write the volume fraction of aggregates of size n :

$$C(n) = C(1)^n e^{\beta(ne_\infty + \delta en^{2/3})} \quad (1.4)$$

We write $C_\infty = e^{-\beta e_\infty}$ to finally get :

$$C(n) = \left(\frac{C(1)}{C_\infty} \right)^n e^{\delta en^{2/3}} \quad (1.5)$$

Finally, we write the total volume fraction of particles in the system as :

$$\mathbf{C} = \sum_n n C(n) = \sum_n n \left(\frac{C(1)}{C_\infty} \right)^n e^{-\beta \delta en^{2/3}} \quad (1.6)$$

Let us now assume that $C(1) < C_\infty$ then the series Eq (1.6) converges to a fixed value. This means that a relation exists between \mathbf{C} and $C(1)$, where the relation between the two is an increasing function given Eq (1.6). Now if \mathbf{C} increases, the single particle volume fraction increases too, until the limit $C(1) = C_\infty$. At this point, we define a total volume fraction of saturation :

$$\mathbf{C}_s = \sum_n e^{-\beta \delta en^{2/3}} \quad (1.7)$$

If more particles are added to the solution, the total volume fraction of particle in solution remains bounded by \mathbf{C}_s . To satisfy this constrain, the system must phase separate into an aggregate of infinite size.

This simple model of self-assembly using only isotropic short-range interactions tells us that assembling finite-size aggregates is impossible beyond a volume fraction that decays exponentially with size, as shown in Eq (1.5). In the next section, we introduce a more refined interaction to achieve structures more complex than an infinite bulk.

1.2.2 Patchy particles model

Patchy particles are spherical objects similar to colloids, on which small patches are grafted at a fixed position. Patches define attractive interaction spots on specific regions of the particle. Unlike in section 1.1, all the patchy particles in solution are identical, which make such a system far easier to engineer. Defining a set of patches on a particle defines the geometry of the interactions between the colloids. We show two examples of such particles in Fig 1.5 (a,c). The assembly of these particles is then simulated using molecular dynamics at a fixed volume fraction. The patches attract each other through a Lennard-Jones potential characterized

by an interaction strength ϵ . Upon equilibrating, when the temperature is not too high compared to the interaction energy ($kT/\epsilon \approx 1$), these particles assemble to form remarkable structures. We represent two examples of such structures in Fig 1.5 (b), where the particles form sheet-like aggregates, or clusters with a finite number of particles in Fig 1.5 (c). In each of these examples, it is the geometry of the patch that generates a size limitation, either on one of the dimensions, or it even limits the number of particles in the aggregate. Other structures, such as empty liquids, that is, liquid states with vanishing volume fraction of particles [18] or gels [19] can be generated using patchy particles. It is important to keep in mind, however, that the self-limitation exhibited by patchy particles always remains of the order of the particle size. Indeed, to generate larger scale structures, one needs to introduce another characteristic length scale in the system.

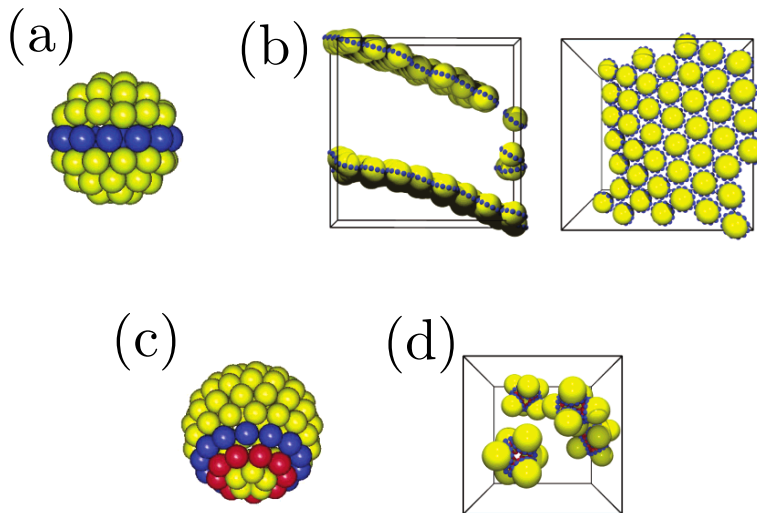


Figure 1.5: **Example of self-assembly of patchy particles:** (a) Particle with a ring shape of patches represented in blue. Yellow beads are atoms with hard core repulsion. (b) Face and side view of the equilibrium sheet structure formed by (a). (c) Double ring of patches where red beads attract red beads, and blue attract blue. (d) Corresponding closed finite-size aggregate. Adapted from [20].

1.2.3 Short-range attractive, long-range repulsive colloids

To overcome the limitations of size control of the previous system, we now introduce another system of assembling spherical particles that do have a characteristic lengthscale built in. We show that this allows for self-limited aggregation over a size larger than the particle size.

Let us consider spherical particles that interact via a two-component potential: a short-range attractive one and a long-range repulsive one. A way to achieve such a potential could be to consider colloids of the same charge that thus repel each other via electrostatic interactions, in a solution with small polymers that create depletion attractive interactions. We model the short-range attractive interaction like in section 1.2 Eq 1.1, and model the electrostatic interaction with a longer range potential with a screening. For instance, we can use a truncated Yukawa potential as in [17, 21, 22]

$$u_{\text{LR}}(r) = \frac{q^2}{r} e^{-r/\xi} \quad (1.8)$$

where q is the charge of the colloids, and ξ is the screening length of the solution. To understand how the competition between these two energies can generate finite-size assembly, let us consider simple scaling laws using the argument presented in [17]. We write the total energy per particle in an aggregate of radius R :

$$e(R) = -e_\infty + \frac{\delta e}{R} + \underbrace{A \int_0^R \text{d}\mathbf{r} \text{d}\mathbf{r}' u_{\text{LR}}(|\mathbf{r} - \mathbf{r}'|)}_{e_{\text{LR}}(R)} \quad (1.9)$$

where the first part is similar to Eq 1.1, and the second part is the sum of all long-range repulsive interactions in the aggregate, with A a geometric constant, and R the radius of the aggregate considered. Assuming ξ is very large compared to the colloid size, we consider two regimes :

- $R \ll \xi$: Each particle in the aggregate interacts with all others via the long-range potential $e_{\text{LR}} \propto R^2$
- $R \gg \xi$: Each particle of the aggregate interacts with all others within a sphere of radius ξ , except the particles close to the boundary of the aggregate. This gives the scaling: $e_{\text{LR}} = e_{\text{LR},\infty} - \delta e_{\text{LR}}/R$, with $e_{\text{LR},\infty}$ the energy of a particle in the middle of the aggregate, and δe_{LR} a geometric parameter corresponding to the lack of interaction at the boundary.

We represent these two scalings in Fig 1.6 and draw a schematic extrapolation of the energy in between. This qualitative picture shows how in some regimes of the parameters $-e_\infty$, $e_{\text{LR},\infty}$, δe δe_{LR} – these two types of potential can lead to a minimum of energy for an aggregate of radius R^* .

By using a more detailed model, it is possible to show that specific models of short-range attractive, long-range repulsive particles can lead to an equilibrium aggregate of arbitrary large size [23, 21]. However, our analysis relies on the assumption ξ is very large compared to the colloid size. Relaxing this approximation can generate an elongated and branched cluster [22].

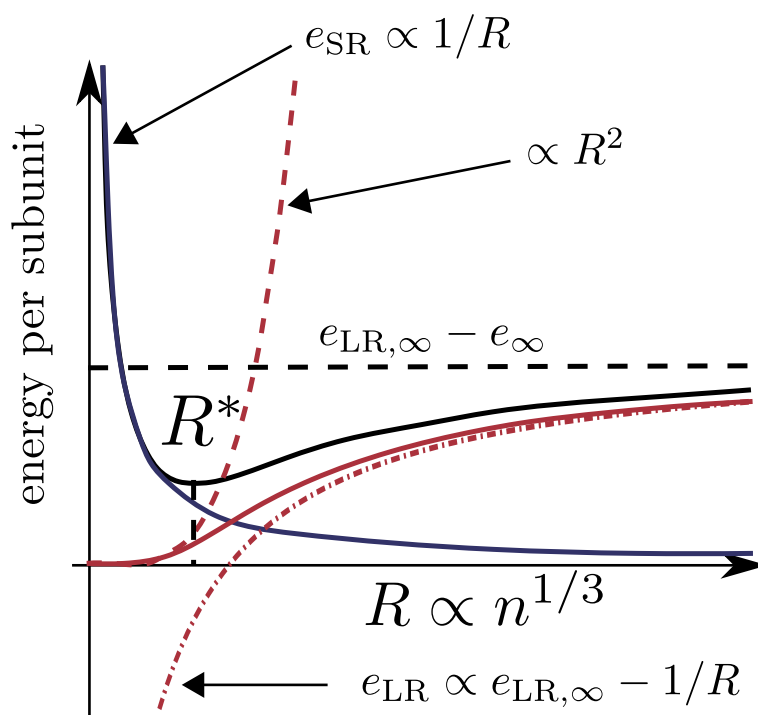


Figure 1.6: **Schematic representation of the energy in an aggregate of size R :** The two red dotted curves represent the scaling of the long-range repulsive interaction at low aggregate radius, and large aggregate radius. The solid red is the extrapolated long-range interaction. The blue line is the short-range attractive energy with the scaling indicated. The dashed black line is the asymptotic value of the total energy for $R \rightarrow \infty$. The solid black line is the total energy with R^* the equilibrium aggregate size.

1.3 Frustrated self-assembly

We have seen that assembling thousands of particles into a precise structure using exclusively short-range interactions is a major challenge. In a different context, cells are able to self-organize to create tissues. In many situations, the growth of tissues comes with a build-up of stress in the tissue. This stress that can only be partially relieved by a deformation is called residual stress [24]. Residual stress appears to play a role in regulating certain biofunctions [25], and in particular, growth. Here, we take a step back from cellular assembly and look at molecular size systems that self-assemble at equilibrium. Even in this simple case, the assembly process of particles can generate residual stress in the structure. In this section, we start by defining frustration in the context of self-assembly and provide an example taken from liquid crystal in section 1.3.1. We then look at a different system of colloidal particles that assemble onto a spherical surface to provide another example of frustrated self-assembly in section 1.3.2. Finally, we introduce the current model and a classification of geometric frustration in section 1.3.3.

1.3.1 Blue phase liquid crystal

Liquid crystals are an intermediate state of matter in which particles display an orientational order similar to a crystal but no positional order similar to a liquid. Their orientation is characterized by a vector director $\hat{\mathbf{n}}$ aligned with the elongated direction of the particles. If the particles are chiral, they may form cholesteric phases, characterized by a twist of the director of the particles along the perpendicular direction, as illustrated in Fig 1.7 (a,b). Under certain conditions of temperature, some of these liquid crystals exhibit a double twist of their director called blue phase, as illustrated in Fig 1.7 (c,d). It turns out that the double twist of the director is not compatible with a long-range order [26]. Therefore, the system must accommodate and organize into tube domains separated by disclination lines, as illustrated in Fig 1.7 (e). The blue phase is an example of frustrated self-assembly, which we can now define. A frustrated self-assembling system is a system of particles whose order parameter follows local rules that are incompatible on a global scale. In this case, the double twist of the director is a local rule that can be achieved locally or along a tube but cannot propagate to the whole system. In the next section, we provide another example of frustrated self-assembly driven by curvature.

1.3.2 Crystallization on a curved space

Here we introduce frustration driven by metric incompatibility. Fig 1.8 (a) shows the clustering of colloids at the surface of a droplet. In this experiment, water

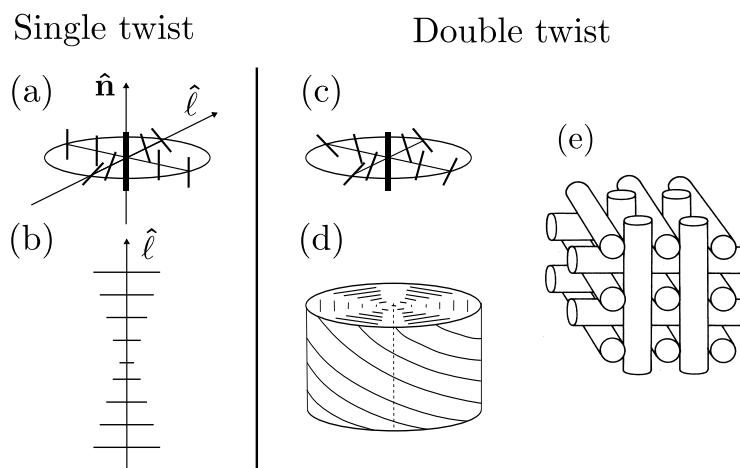


Figure 1.7: **Illustration of single twist vs double twist:** (a) illustration of the single twist of the director: $\hat{\mathbf{n}}$. The thick black line is a reference of the director. The director of the neighboring particle is represented in two directions, one rotating, the other remaining aligned. (b) planar projection of the director in the direction of the twist axis: $\hat{\ell}$. (c) represent a situation similar to (a) but with a double twist. (d) illustration of a tube with a double twist. The rotating lines outside the tube represent the rotation of the director along the tube. (e) organization of tubes with one another to form the so-called blue phase. adapted from [26], and http://en.wikipedia.org/wiki/Blue_phase_mode_LCD

droplet in oil contains colloidal beads and a depletant that pushes the beads towards the surface of the droplet. The depletion interaction moreover promotes the tight packing of the colloids into a regular triangular lattice crystal structure. However, the crystal structure must accommodate the Gaussian curvature. In general, periodic orders are incompatible with Gaussian curvature. To understand this, we represent a few geodesics on a sphere in Fig 1.8 (b). A geodesic is the equivalent of a straight line in a curved space. It represents the shortest distance between points. Meridians, for instance, intersect at the pole of an ellipsoid, which would translate into defects in the crystal structure. An ordinary geodesic is also plotted to give an intuition of the difficulty of propagating a positional order on a curved space. On top of the ordering of the colloidal particles into a regular crystal structure, the depletion interaction promotes the formation of aggregates with an isotropic disk shape. A disk shape would minimize the length of the border of the aggregate. In this example, the emergence of ribbon-like domains results from a trade-off between the free energy cost of deforming the crystal structure and the free energy cost for the aggregate to have a free edge. The emergence of an elongated structure also appears here as a limitation of the propagation of the order parameter in one direction. The free energy change due to deformation of the crystal structure is reminiscent of what stress is at a microscopic level [27]. This type of example suggests that the emergence of patterns due to residual stress in a structure is a general mechanism that may apply in many microscopic situations.

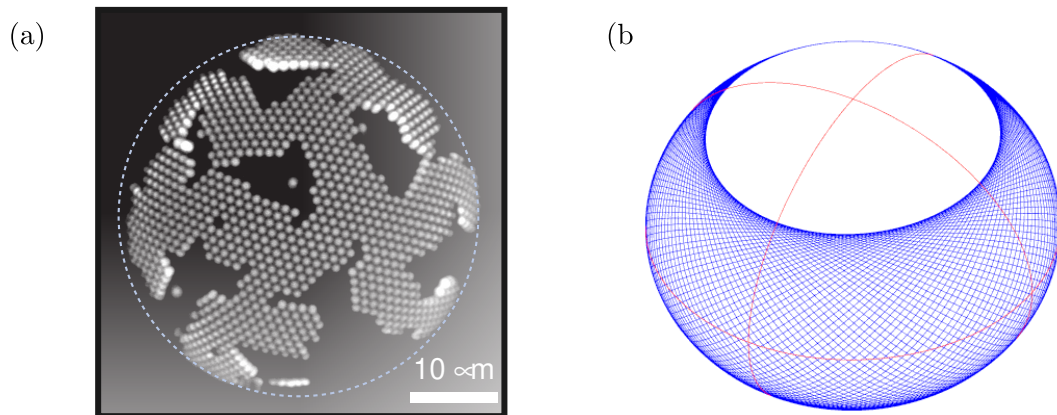


Figure 1.8: **Frustrated self-assembly on a sphere** : (a) colloidal particles assembled on the surface of a spherical droplet. They interact by depletion attraction. Adapted from [28]. (b) Plot of four geodesics on an ellipsoid, three simple closed geodesic – geodesics, which close on themselves without intersection – are represented in red: the equator, and two meridians. An ordinary geodesic in plot in blue that oscillates between two latitudes. <https://geographiclib.sourceforge.io/1.29/triaxial.html>

1.3.3 Modeling the frustration

The examples previously introduced reveal that geometric frustration can lead to self-limited aggregation or the emergence of anisotropic structures. We now present some generic properties of geometrically frustrated systems and review existing models.

As presented before, geometric frustration introduces an energetic cost to the process of aggregation due to the impossibility to propagate the local organization rules to larger scales. This cost is antagonistic to the attractive interaction that initially drives the aggregation. We write the energy per particle in such a system by distinguishing the two phenomena. In the case of a 3D anisotropic spherical aggregate :

$$e(n) = -e_{\infty} + \frac{\delta e}{n^{1/3}} + e_{\text{ex}}(n) \quad (1.10)$$

where the first term corresponds to the short-range attractive energy, written similar to Eq 1.1, the energy associated with frustration is denoted $e_{\text{ex}}(n)$, using the notation from [17]. For the frustration to influence the structure, or the size of an aggregate, its associated energy e_{ex} must satisfy certain constraints.

In [29], the authors distinguish what they refer to as cumulative vs non-cumulative frustration. Cumulative frustration corresponds to a situation where the energetic cost of frustration grows super extensively, i.e faster than the size of the aggregate. This means that the energy per particle $e_{\text{ex}}(n)$ is an increasing function of n . If this condition is not respected, the frustration energy e_{ex} becomes equivalent to a rescaling of the short-range interaction and can be merged into the e_{∞} term. A similar idea has been introduced in [30], in which the authors show that in some cases the frustration appears to be irrelevant since it can be eliminated through a coarse graining of the system. Cumulative frustration implies a fast growth of the energy of the system with its size. If no mechanism limits the growth, the frustration mechanism is said to be hard or rigid, otherwise it is a soft frustration.

To help us classify the type of frustration due to geometric incompatibilities, we use a toy model of shape flattening initially introduced in [31]. Fig 1.9 (A) shows a model of assembling particles that interact via specific interactions. Their shape is such that the assembly of a row is bent and thus a 2D tiling requires the deformation of the assembling particles. Fig 1.9 (B) shows the evolution of the energy as the aggregate size increases. After a first regime where the energy increases super-extensively – cumulative frustration – the energy reaches a plateau that corresponds to the energy required to fully flatten the rows. Despite the simplicity of this model, the emergent phenomenology has also been observed in systems of self-assembling twisted bundles [32, 33]. Mainly, this model reproduces a transition between rigid to soft frustration as the aggregate size increases that

is usually observed in geometrically frustrated assembling systems. Indeed, the shape of the e_{ex} is reminiscent of the energy function introduced in section 1.2.3. Similar to the short-range attractive long-range repulsive model, the transition from cumulative to non-cumulative frustration results from a boundary layer in which particles have an additional freedom to relax the stress accumulated by the aggregation. Such a boundary layer defines a characteristic length scale that sets the size of the assembly. This analogy between shape flattening and frustration

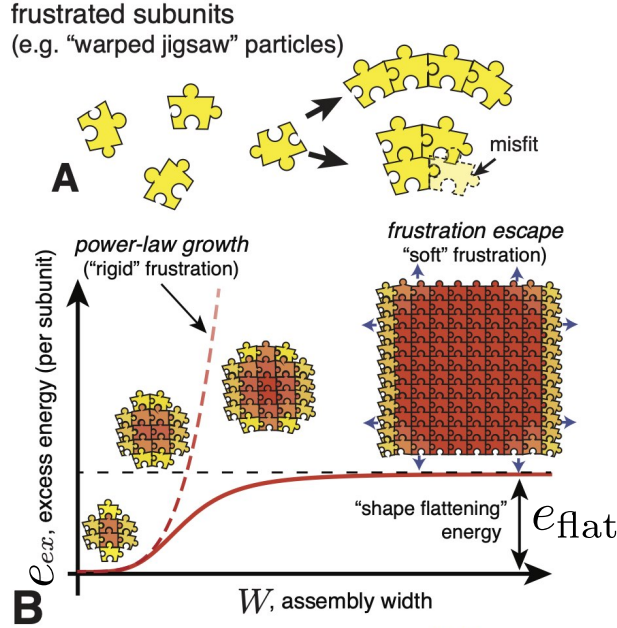


Figure 1.9: **Warped jigsaw model** : (A) The assembly of jigsaw particles via specific interactions promote the formation of a 1D curved aggregate. Assembling a 2D structure requires a deformation corresponding to the flattening of each row. (B) Illustration of the energetic growth due to frustration with aggregate size. Initially the energy e_{ex} grows super-extensively, here modeled as a power law, which corresponds to a regime of cumulative frustration. This energetic growth then reaches an upper bound: e_{flat} . It is the energetic cost associated to the process of flattening the rows of the aggregate, which has to remain finite. In this regime, the frustration has become non-cumulative. Adapted from [31]

goes beyond the illustration given here. To understand why shape flattening is a generic model for residually stressed systems, we introduce the metric description of elasticity [34]. Let us consider a body to which we endow curvilinear coordinates: $\bar{x} \subset \mathbb{R}^3$ that is attached to the body, and thus deforms with it. A point tracked by a set of three coordinates (x_1, x_2, x_3) in an undeformed state will have the same coordinates in any deformed state. We then associate to each point of the body

- or similarly to each \bar{x} - a coordinate in the real space: $\bar{r}(\bar{x})$. And we define the metric tensor as :

$$g_{ij} = \partial_{x_i} \bar{r} \partial_{x_j} \bar{r} \quad (1.11)$$

The metric tensor can be used to compute the infinitesimal distance ds , using the generalized Pythagorean theorem:

$$ds^2 = g_{ij} dx^i dx^j \quad (1.12)$$

In the scope of linear elasticity, the elastic energy density e of a body can be expanded up to second order around a stress-free metric: $\epsilon = \frac{1}{2}(g - \tilde{g})$, where g is the current metric of the body, and \tilde{g} is the target metric.

$$e = A^{ijkl} \epsilon_{ij} \epsilon_{kl} + \mathcal{O}(\epsilon^3) \quad (1.13)$$

A^{ijkl} is a rank four tensor that is fully determined by the target metric and the elastic constants of the body: Young's modulus, and Poisson's ratio. Eq 1.13 is reminiscent of Hooke's law. In fact, the Hooke's law can also be written in terms of metric elasticity. The body is in a stress-free state if $g = \tilde{g}$. However, if \tilde{g} can be any matrix, g , on the contrary, is constrained by the fact that it has to define a flat Euclidean space to be embeddable in a real space. It is possible that \tilde{g} defines a curved metric [35] which is a specific case of non-embeddable metric. In this case, the body cannot reach the target metric: the body is residually stressed.

This framework has been used, for instance, to compute the energy of twisted nano ribbon structures [36]. As we will show in section 2.1.1, unlike the warped jigsaw model that is intrinsically softly frustrated, the energy required to flatten a 2D metric grows super extensively, which provides an example of hard frustration. In the case of nano ribbons, as in most geometrically frustrated systems, the super extensive growth of the energy is ultimately balanced by another mechanism, in this case, a change in configuration. Fig 1.10 shows the transition from a twisted to helical shape, and finally tubular configuration as the width of the ribbon increases.

1.4 Objectives

In this chapter, we have introduced the type of self-assembling units we are interested in: proteins, small colloids, folded single strands of DNA. In the rest of this part, we call them without distinction: particles. These assembling particles interact together via short-range interactions. As demonstrated in section 1.2, building an aggregate of finite size using short-range interactions is not trivial. However, we provided examples where specific interactions between particles can achieve finite-size assembly by creating closed structures, as it is the case of virus capsids. We

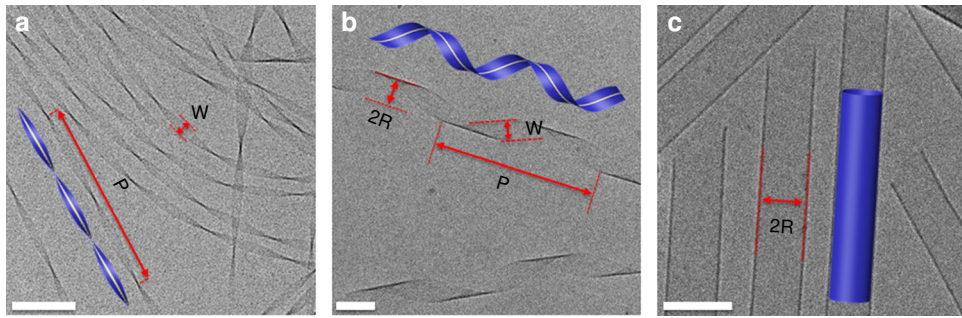


Figure 1.10: **Conformation change of nano ribbons** : (a): shows the twisted configuration of ribbons at small width. As the width increases, the ribbons turns into (b): a helical shape, and ultimately a tubular shape represented in (c). The width is noted W , the pitch P , and the radius for helices tubules is denoted as R . adapted from [36]

have then introduced the notion of frustration in self-assembly as being a global incompatibility to achieve a prescribed local order. The nature of frustration can be diverse [37, 38], but in the two examples we have given, a lengthscale emerges. In the case of the blue phase, the tube domains have a fixed radius and in the case of colloidal crystals assembled on a curved surface, the ribbon-like domains have a well-defined width.

In this first part of the thesis, we will study another type of frustration. In cells, proteins that are normally soluble in their functional state start to aggregate and form fibrils. These fibrils can cause severe diseases such as Alzheimer's disease, Parkinson's disease and sickle cell anemia. [39, 1]. Despite a wide diversity of mechanisms explaining the formation of fibrous aggregates [40], and their polymorphism [41], the ubiquity of these fibrous structures suggests that they share a common physical origin. However, such proteins have not been optimized to fit together since it is not their primary function.

Inspired by these experimental observations, we develop an alternative generic model for frustration that exhibits a phenomenology similar to the jigsaw model. We aim at providing a way of modeling frustration in a system that does not require non-euclidian metrics, and allow for analytical computation of the stress field in the aggregate. We are using a general mechanism for the assembly of particles whose shape has not been optimized to fit together. Because proteins are also an elastic material, they can deform to satisfy both local assembling rules and global order. However, this deformation comes at an energetic cost that causes residual stress in the assembly. The shape of the aggregate results from the competition between short-range attractive interactions and long-range elastic stress in the aggregate. Previous work suggests that such a mechanism can lead to

the formation of fibrous structures [42]. However, the protocol they used only gives rise to metastable fibers and does not explain the stability of fibrous structures. Using a simpler model for ill-fitting self-assembling particles, we investigate two phenomena previously described :

- The emergence of a characteristic length that sets the size of the equilibrium aggregate.
- The formation of equilibrium fibrous aggregates.

Chapter 2

Assembling particles can be modeled using simple geometrical shapes

In this chapter, we explain how we designed a model for frustrated self-assembling particles. We are interested in modeling isotropic particles that interact via specific short-range interactions, but whose shape is not optimized to tile the space. Particles – proteins, colloids, or folded DNA single strands, for instance – are modeled as a simple, ill-fitting geometrical shape. In the work previously reviewed, two mechanisms are introduced to create frustration: The incompatibility of long-range order with curvature or with chirality. These approaches have demonstrated the importance of frustration in the self-assembling process through the build-up of residual stress but none of the two directly apply here. Instead, we will use a simple model, fully solvable, to understand better how geometrical frustration can lead to self-limited aggregation and symmetry breaking via the formation of fibrous structures.

We model the elastic rigidity of particles using harmonic springs. These springs have to be stretched or compressed to tightly pack the particles. The short-range interactions are modeled by 1: an assembling rule, 2: a surface tension. The assembling rule, which reproduces the specificity of the interactions, defines the regions of the particles that interact together. The surface tension is a fixed cost for a particle to have an edge without a neighbor. Fine-tuning the surface tension regulates the intensity of the interactions between particles.

We start by explaining how we chose the geometrical shape that represents the assembling particles in section 2.1. We then fully derive the energy of a simplified model of particle in section 2.2. Despite its simplicity, most of the interesting phenomena are already emerging in this 1D model. Finally, in section 2.3 we present the results of a 2D continuum limit analytic theory of the frustration generated by two incompatible flat spaces.

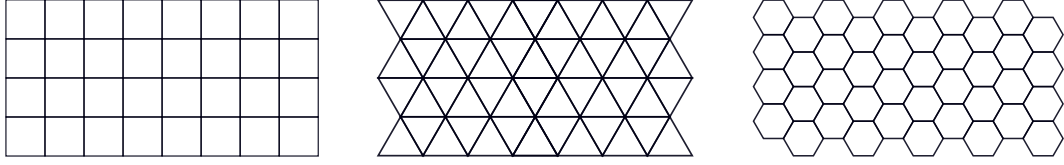


Figure 2.1: **The three regular tiling of the plane**

2.1 Choosing the correct shape

Before we dive into a specific model of frustrated assembly, we will consider the various options we have to design the geometry of an ill-fitting particle. Because we are interested in the emergence of fibrous structures, we want to use particles with at least a three-fold symmetry. Moreover, we focus on the aggregation of similar particles to avoid the formation of dimers, for instance, that would break the three-fold symmetry. Ultimately, our goal is to design a model of frustrated particles which can create a homogeneous packing over a finite deformation. The homogeneity of the packing is required to develop a continuum theory of our system. The condition of packing over a finite deformation will prevent any non-physical divergence of the energy. There exist only three regular tillings – meaning identical regular tiles and identical regular vertices – with a single geometrical shape that are possible [43]: triangular lattice, square lattice, and the hexagonal lattice Fig 2.1. This means that most three-fold symmetric particles should be ill-fitting. We start by naively considering pentagons and show that the above two conditions – homogeneity or finite deformation – cannot be satisfied together in section 2.1.1. We then introduce the shapes we will be using in section 2.1.2.

2.1.1 Pentagon case

If only a few shapes can tile the plane, let see how we choose the design of ill-fitting particles. We use the example of pentagons to show a major issue that may appear if we do not choose a shape thoughtfully. In our model, the short-range interaction between particles requires to pack them tightly. Fig 2.2 (a) shows the mismatch between pentagons when we try to assemble them. Pentagons can create a tight assembly in a curved space, as illustrated by the regular dodecahedron represented in Fig 2.2 (b). Let us now think of the pentagon as a deformable particle. Fig 2.2 (c) shows how deforming pentagons can be a way to create a tight tiling of particles. One must keep in mind that deforming a pentagon to tile a flat space requires a deformation corresponding to the process of flattening the assembly of the pentagon from a curved space. This deformation turns out to diverge as the number of pentagons aggregated increases. To understand this, we

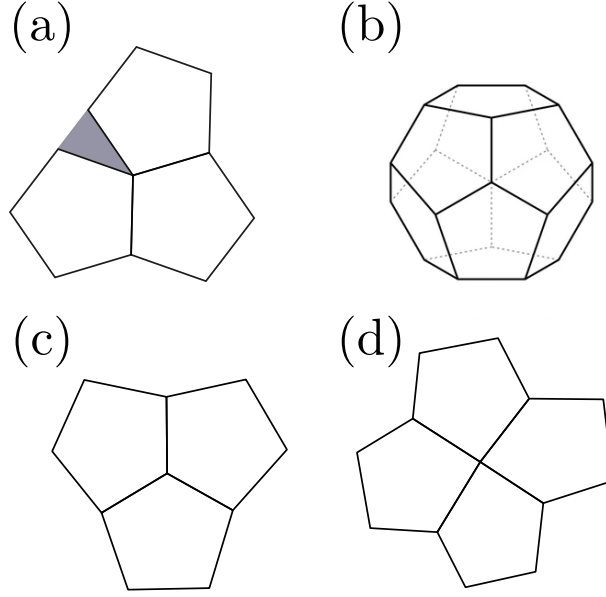


Figure 2.2: **Assembling pentagons** : (a) The inner angle of a pentagon (108°) is not a divisor of 360, no regular tiling is thus possible with pentagons. (b) Pentagons can also assemble in curve space without deformation, as in a dodecahedron. (c) A tight assembly of the pentagon can be achieved through deformation of the pentagons. (d) assembling deformed pentagons can also be achieved by introducing vertices with 4 pentagons. The assembly of many pentagons can be achieved with a combination of vertices with three and four pentagons.

consider a 2D assembly that aggregates with a preferred radius of curvature \mathcal{R}_0 . Let us consider the outer layer of the aggregate represented in gray in Fig 2.3. The area of this region is given by

$$d\mathcal{A}_{\text{sphere}} = 2\pi\mathcal{R}_0^2 \sin\theta d\theta \quad (2.1)$$

Now consider flattening this spherical cap. The radius of the flattened disk is the curvilinear distance radius of the cap: $\theta\mathcal{R}_0$. The area of the outer layer is given by :

$$d\mathcal{A}_{\text{disk}} = 2\pi\mathcal{R}_0^2\theta d\theta \quad (2.2)$$

If we compute the ratio of these two areas :

$$\frac{d\mathcal{A}_{\text{disk}}}{d\mathcal{A}_{\text{sphere}}} = \frac{\theta}{\sin\theta} \xrightarrow{\theta \rightarrow \infty} \infty \quad (2.3)$$

As the aggregate grows, θ increases and the relative area of the outer layer of the flattened assembly diverges. In the situation of tight packing, the density of

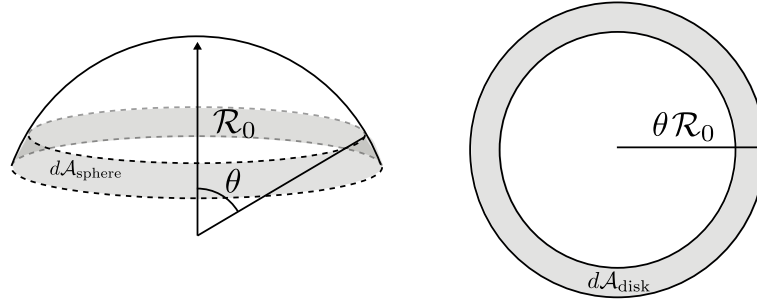


Figure 2.3: **Flattening of a sphere** : On the left, a spherical cap that corresponds to an aggregation process with a preferred curvature radius

particles remains the same in both situations, which means that the particles are increasingly stretched as the size of the aggregate increases. There are, however, multiple ways to deform pentagons to produce a tight tiling. Fig 2.2 (d) illustrates how it is possible to introduce vertices made of 4 pentagons. A way to avoid the divergence of the deformation – which implies a divergence of the elastic energy – is to introduce topological defects of 4-pentagon vertices into a 3-pentagon vertex arrangement. The drawback of defects is that it introduces point-like disruption of the order parameter, which is hard to capture with a continuous limit theory.

2.1.2 Lattice-inspired irregular particle

We have shown that using any kind of geometrical shapes that do not tessellate to model a protein may induce surprising behaviors: divergence of the energy with the number of particles or defects. To avoid this type of complication, we are going to use particles inspired by shapes that do tessellate. For each of the three lattices represented in Fig 2.1 we derive a corresponding frustrated particle represented in Fig 2.4 (a,b,c). They are actually lattice models and particles thus assemble according to the same topology as their associated lattices. We introduce a small irregularity (ϵ) compared to the lattice's mesh size (δ), differently for each particle type. Tight packing of such particles requires them to deform, and the deformation required increases as the number of particles aggregated grows. However, unlike the pentagons, the deformation required for tight packing has to remain bounded. Each of these particles can be turned into a lattice's unit cell through a deformation of the order of ϵ . When an aggregate becomes big, the only way for these particles to tightly pack while keeping the lattice topology – imposed by construction – is to adopt the shape of the lattice unit cell itself. We call this configuration, the bulk configuration of a particle and the associated elastic energy, the bulk energy.

The deformation imposed by the aggregation is translated into an energy variation by using linear springs as represented in Fig 2.4 (d,e,f). We distinguish two

kinds of springs: the main springs and the coupling springs. The main springs have been designed to generate two similar networks with different mesh sizes. The rest lengths of all small main springs –represented in red in Fig 2.4– have a rest length $\delta - \epsilon$, while the big main springs –green in Fig 2.4– have a rest length $\delta + \epsilon$. These two networks are coupled together via coupling springs -represented in blue in Fig 2.4- whose rest length is adjusted for each system to guarantee stress-free single particles.

A particle also comes with its own aggregation rule represented in Fig 2.4 (g,h,i). Indeed, we consider particles that interact via short-range specific interactions. It results from the specificity of the interactions that the particles are effectively not allowed to rotate. Ultimately, springs of the same color have to connect. In a large aggregate, we consider two sets of main springs – red and green – and they both form a spring network with different mesh sizes – red: $\delta - \epsilon$ and green: $\delta + \epsilon$ –. Each spring network is yet coupled by coupling springs – blue – which introduce a residual stress in the structure. In an infinite size aggregate, these two spring networks have to match the symmetry of the network, and therefore have to match their mesh size. It is the bulk configuration represented in Fig 2.4 (j,k,l). It is worth to mention that in each of these models, the frustration in an aggregate results from two networks of incommensurable lattice sizes – red and green – that are coupled by blue springs. In a large aggregate, the two networks have to adopt the same lattice spacing. In other words, they become commensurable.

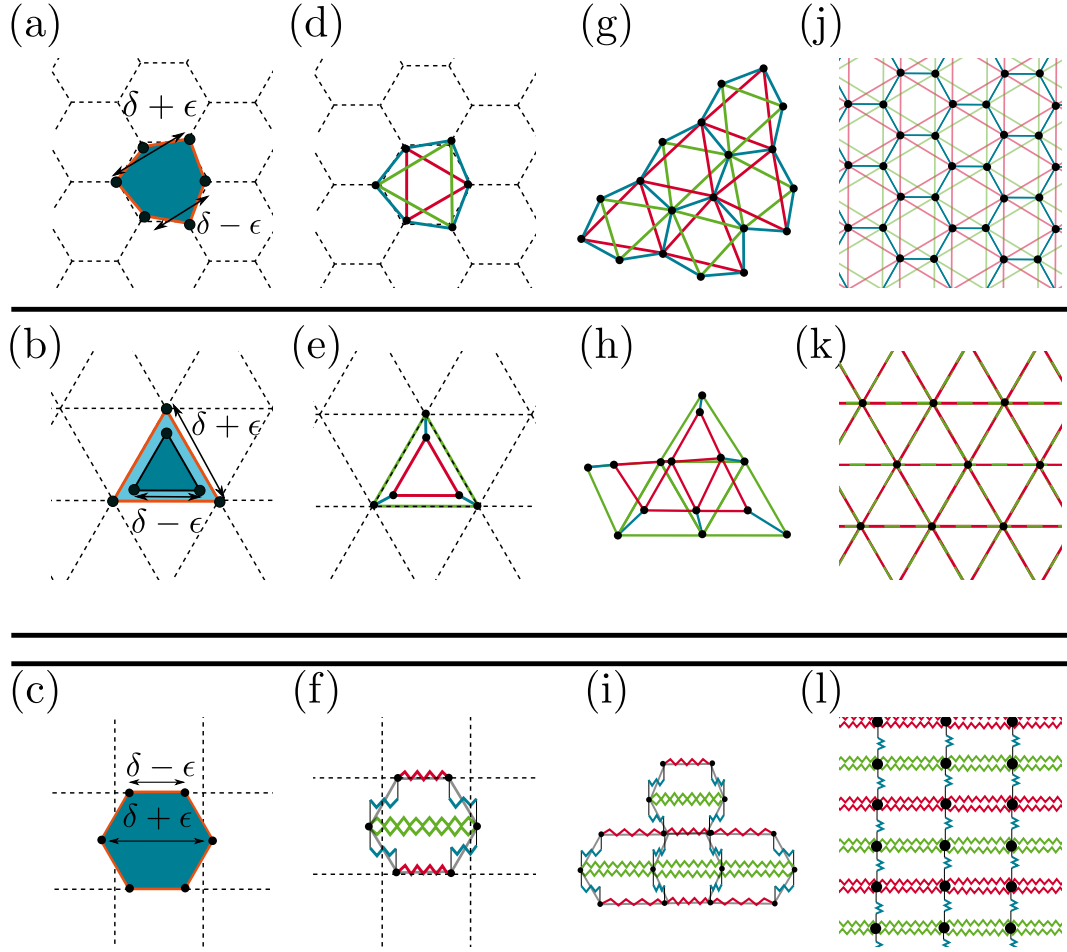


Figure 2.4: **Lattice-inspired ill-fitting particles:** (a,b,c) Respectively hexagonal, triangular, and squared ill-fitting particle. ϵ quantifies the amount of frustration. Black dots represent the nodes of the particles. Nodes are the elastic degree of freedom. (d-e-f) The elasticity of the particles is modeled by linear springs, each line representing a spring. Green and red springs are called main springs, have a stiffness k and the blue springs are coupling springs of stiffness k_c . (f) The squared particles are elastically rigid only in the horizontal direction. (h) Triangular particle aggregation requires both the nodes of the big, and of the small triangle to merge together. (g,h,i) The aggregation process consist of merging the nodes that belong to the same vertex. We show how particles have to deform when they aggregate. Notice that only the nodes merge and two parallel springs are equivalent to a single one by summing the stiffness. Therefore, we represent parallel springs as one spring. The aggregation rule is binary: if two particles are neighbors, they necessarily stick together. Moreover, it is always total, which means that no crack or partial binding is allowed. It can be translated as not allowing particles to rotate, which forces red springs to connect with red springs and similarly for green springs. (j,k,l) When in a large aggregate, the particles are deformed up to the lattice's unit cell – half a unit cell for the triangle – which sets a bound to the deformation.(k) The dashed red/green line means that both small and big triangles overlap.

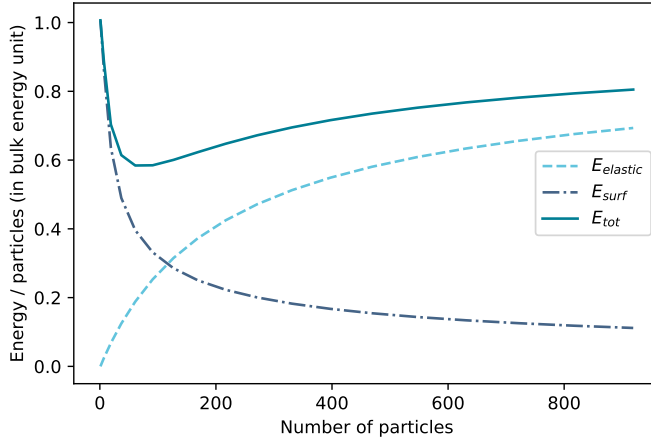


Figure 2.5: **Schematic of the two antagonist energies in an aggregate:** The elastic energy comes from the frustration. It increases with the size of the aggregate but has to remain bounded by the bulk energy. The surface energy per particle decreases with the number of particles $E_{surf} \propto 1/\sqrt{n}$, where n is the number of particles.

Finally, we set the strength of the sticky interactions equal and the energy of a particle with all its interacting neighbors to 0. Therefore, instead of counting the number of interactions satisfied, we count the interactions non-satisfied. This way, the sticky interaction energy takes the form of a surface tension that we will keep calling surface tension. This means that there is a constant cost for every edge without a neighboring particle, represented as an orange line in Fig 2.4 (a,b,c) and denoted J . Two energies are thus competing. A sticky, short-range interaction drives the aggregation process. However, the geometry of the particles does not allow for the satisfaction of all interactions. To do so, the particles need to deform, which induces an energetic cost related to the elasticity of the particles. Let us consider the energy per particle in a 2D aggregate –squared or circular– made of n particles. In this case, the surface tension decreases as the size of the aggregate increases:

$$E_{surf}(n) = \gamma \frac{\sqrt{n}}{n} \quad (2.4)$$

The elastic deformation, however, increases until the particles are deformed into their bulk configuration as represented Fig 2.5. Finally, the size of the aggregate results from a compromise between surface tension minimization and elastic frustration.

2.2 Full computation of the squared model

In this section, we detail the computation for the square 1D model of elastically frustrated self-assembling particles in Fig 2.4(c,f,i,l). Despite its simplicity, this model captures the emergence of finite size self-assembly through geometric frustration, in addition to providing an intuitive understanding of it. The model is said to be 1D because the particles are only mechanically rigid in the horizontal direction. However, the particles are living on a 2D square lattice.

We now consider an ideal situation for full computation of the model represented in Fig 2.6. The aggregate is infinite in the vertical direction and made of w particles in the horizontal direction. Such an aggregate will be called a fiber in the following. It is important, however, to keep in mind that the particles are anisotropic by construction, thus every aggregate is a fiber. First, we can quickly compute the surface tension energy per particle :

$$e_{\text{surface}} = \frac{2J}{w} \quad (2.5)$$

where J is the energetic cost associated with a free edge. We then compute the elastic energy. Fig 2.6 represents the chain of coupled springs corresponding to this situation. The system is invariant along the vertical axis and so, we restrain our computation to the energy of a single layer. The positions of the extremities – the nodes – of the small red springs of the particle are tracked on the x axis and the position of the large, green one on the y axis as represented in Fig 2.6. We introduce the coordinates associated with the particle i as represented in Fig 2.6.

$$\begin{cases} x_i = x - i(\delta - \epsilon) \\ y_i = y - i(\delta + \epsilon) \end{cases} \quad (2.6)$$

Using this, we write the force balance equation for a point on the red network x_i and its corresponding coupled point y_i :

$$\begin{cases} k(x_{i+1} + x_{i-1} - 2x_i) + 2k_c(y_i - x_i) = 0 \\ k(y_{i+1} + y_{i-1} - 2y_i) + 2k_c(x_i - y_i) = 0 \end{cases} \quad (2.7)$$

The k terms correspond to the force of the main springs – red and green – and the k_c terms correspond to the force of the coupling springs – blue. The same force balance at the boundary gives the associated boundary conditions at the right of the fiber. We placed the origin of the particle number, $i = 0$ in the middle of the fiber. The symmetry of the fiber, $i \rightarrow -i$ guarantees the solution for x_i and y_i to

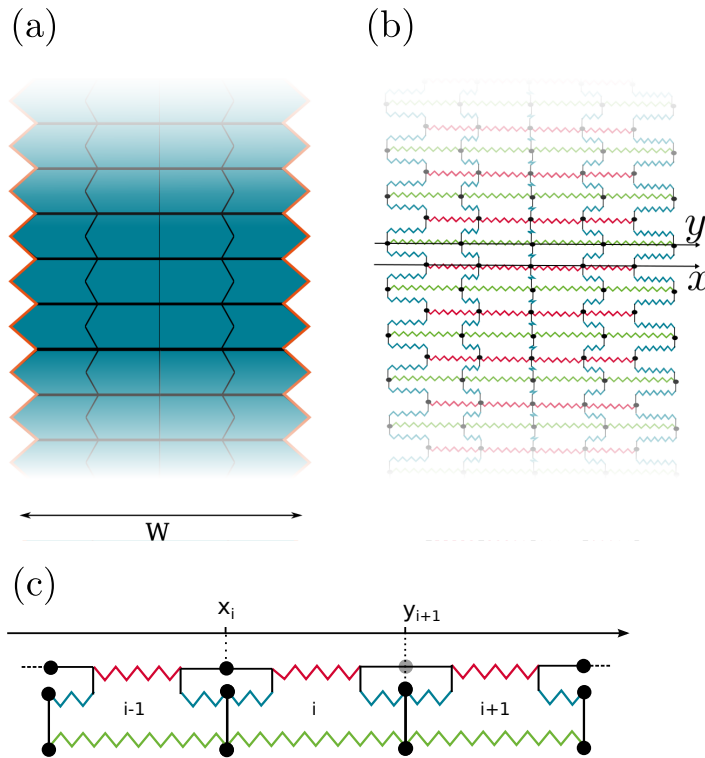


Figure 2.6: **configuration of an infinite fiber** : (a) Arrangement of a fiber of horizontal width W and infinite on the vertical direction. (c) Corresponding arrangement of the springs. (d) The vertical invariance, allows us to only consider a slice of the aggregate. The coordinates of the node associated to the particle i are also given.

be odd. The boundary condition on the left of the fiber is thus redundant.

$$\begin{cases} k(x_{w/2-1} - x_{w/2} + 1 - \epsilon) \\ + k_c(y_{w/2} - x_{w/2} - \epsilon) = 0 \\ k(y_{w/2-1} - y_{w/2} + 1 + \epsilon) \\ + k_c(x_{w/2} - y_{w/2} + \epsilon) = 0 \end{cases} \quad (2.8)$$

Now that we have a set of discrete equations for the mechanical equilibrium of such an aggregate, we will show how to solve them.

2.2.1 Continuum limit

To solve this system of equations, we consider the continuum limit. The system approaches the continuum limit when the typical size of the particle goes to 0:

$\delta \rightarrow 0$ with a fixed density of particles. To do so, we transform the discrete space parameters into their continuum equivalents. As δ goes to zero, the stiffness of the different springs – k , k_c – and the mismatch ϵ changes too. Thus, we define a new set of parameters, which stay constant during the transition $\delta \rightarrow 0$:

$$\begin{cases} E = k \cdot \delta \\ \kappa = k_c / \delta \\ \eta = \epsilon / \delta \\ \gamma = J / \delta \end{cases} \quad (2.9)$$

E is the Young modulus of a particle, κ a continuum coupling, η is the relative mismatch, γ the surface tension. We define the new coordinates of space ξ and the total width of the fiber \mathcal{W} as

$$\begin{cases} \xi = i\delta \\ \mathcal{W} = w\delta \end{cases} \quad (2.10)$$

Expanding Eq (2.7) and (2.8) up to the second order in δ we get Eq (2.11) for the bulk and its associated boundary condition Eq (2.12).

$$\begin{cases} E\partial_\xi^2 x + 2\kappa \cdot (y(\xi) - x(\xi)) = 0 \\ E\partial_\xi^2 y + 2\kappa \cdot (x(\xi) - y(\xi)) = 0 \end{cases} \quad (2.11)$$

$$\begin{cases} \partial_\xi x|_{\mathcal{W}/2} - 1 - \eta = 0 \\ \partial_\xi y|_{\mathcal{W}/2} + 1 + \eta = 0 \end{cases} \quad (2.12)$$

We can write the associated solution $x(\xi)$ and $y(\xi)$.

$$\begin{aligned} x(\xi) &= \xi - \eta \cdot \ell_0 \cdot \frac{\sinh\left(\frac{\xi}{\ell_0}\right)}{\cosh\left(\frac{\mathcal{W}}{2\ell_0}\right)} \\ y(\xi) &= \xi + \eta \cdot \ell_0 \cdot \frac{\sinh\left(\frac{\xi}{\ell_0}\right)}{\cosh\left(\frac{\mathcal{W}}{2\ell_0}\right)} \end{aligned} \quad (2.13)$$

with $\ell_0 = \frac{1}{2}\sqrt{\frac{E}{\kappa}}$. Eq (2.13) reveals two terms, the first one – $x(\xi) \propto \xi$ – means that the particles have adopted their bulk configuration: a square shape. The second term, proportional to the mismatch η , decays as we move away from the boundary $\pm\mathcal{W}/2$. The characteristic size of the region affected by this term is given by ℓ_0 . The emergence of this characteristic length is reminiscent of the transition

between two phases, commensurate/incommensurate [44]. To better understand what is happening, let us compute the local elastic energy density:

$$e_{el}(\xi) = E\delta\eta^2 \left(1 - \frac{\cosh(\xi/\ell_0)}{\cosh(\frac{W}{2\ell_0})} \right) + 4\kappa\delta\eta^2\ell_0^2 \frac{\sinh(\xi/\ell_0)}{\cosh(\frac{W}{2\ell_0})} \quad (2.14)$$

The first term is the elastic energy due to the deformation of the main springs, and the second is the energy of the coupling springs. If we focus on the first term – the elastic energy of the main springs – we observe that the energy is maximum in the center of the fiber $-\xi = 0$ and decays to vanish on the boundary. The characteristic length over which this decay happens is the characteristic length ℓ_0 . We call this region: the stress relaxation boundary layer.

2.2.2 Equilibrium limited size assembly

We integrate Eq (2.14) for $\xi \in [-W/2, W/2]$ to compute the average elastic free energy density Eq (2.15) on the fiber.

$$f_{elastic} = E\eta^2 \left(1 - \frac{\tanh(W \cdot \sqrt{\frac{\kappa}{E}})}{W \cdot \sqrt{\frac{\kappa}{E}}} \right) \quad (2.15)$$

Adding the surface tension energy and using the dimensionless parameter leads to obtain Eq (2.16).

$$\frac{f_{tot}}{f_b} = \frac{\Gamma}{W} - \frac{\tanh(W)}{W} \quad (2.16)$$

with

$$\begin{cases} f_b = E \cdot \eta^2 \\ \Gamma = \frac{\gamma \sqrt{\kappa}}{E^{3/2} \cdot \eta^2} \\ W = \mathcal{W} \cdot \sqrt{\frac{\kappa}{E}} \end{cases} \quad (2.17)$$

where f_b is the energy of a particle in a bulk configuration, W is the rescaled width. This function has a minimum of energy only for $\Gamma \in [0, 1]$. Fig 2.7 shows the evolution of the energy function as the surface tension Γ increases. We see a minimum of energy for a finite value of W , which corresponds to an equilibrium finite-size self-assembly. The value of W for which the energy is minimum increases as Γ increases, and disappears for $\Gamma \geq 1$. This simple model reveals the existence of equilibrium limited size self-assembly in a range of surface tension $\Gamma \in [0, 1[$ through the emergence of a characteristic length scale: ℓ_0 . ℓ_0 is the length over which the stress in the system relaxes around the free boundary, which stabilizes

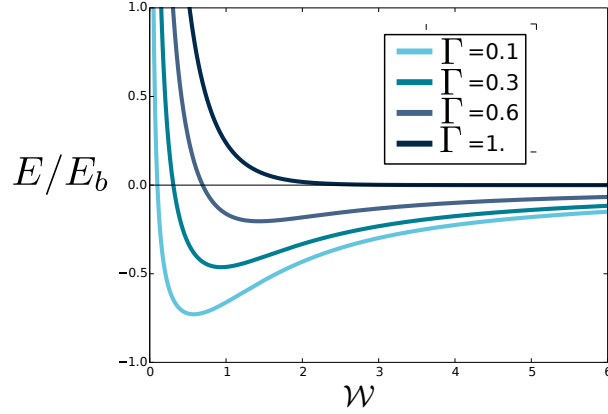


Figure 2.7: **Evolution of the minimum of the energy as the rescaled surface tension Γ increases**

finite-size aggregates. If the surface tension is strong enough to build an aggregate of width too large, which means $\mathcal{W}_{eq} \gg 2\ell_0$ then boundary relaxation layer turns out to scale like a surface term – in Eq (2.16): $\tanh(W) \rightarrow 1$ gives $f_{elastic} \propto 1/W$ – and nothing limits the increase of width anymore. Thus, we observe a transition to bulk. Fig 2.8 recapitulates this transition.

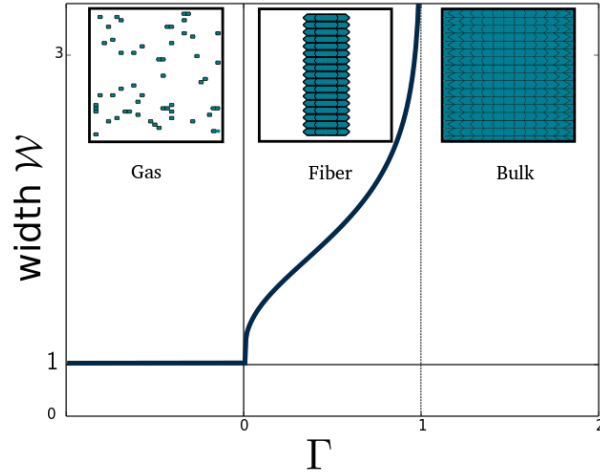


Figure 2.8: **Equilibrium width of the finite-size assembly as a function of the surface tension:** $\Gamma \leq 0$ means that the interaction between particles is repulsive and the particles do not aggregate together. $\Gamma \in [0, 1[$ is the situation that we just described. The equilibrium width diverges as Γ approaches 1. For $\Gamma \geq 1$ the surface tension is so strong that nothing limits the aggregation.

2.3 Continuum model

The analytical computation of the simple square particle model revealed the emergence of a characteristic length scale. This length turns out to define the characteristic size of equilibrium self-limited aggregates. We now present a continuum theory for the computation of the energy of the triangular and hexagonal particle model that has been developed by M. Mert Terzi postdoc in the group. The computations are essentially similar to the one of the previous section and so, we do not present every detail. The approach is different, however, we do not derive a continuum limit from the discrete spring model. Instead, we build a general continuum model and later show how it applies to the specific spring model. One of the differences with the square particle model comes from the fact that the triangular/hexagonal particles have been designed to be three-fold symmetric. The aggregate shape is thus expected to display the same symmetry. However, we show here that under certain conditions, symmetry breaking occurs, and the fibrous-like aggregate turns out to be energetically favored over three-fold symmetric aggregates. As explained in section 2.1.2, a large aggregate can be viewed as two regular spring networks with incompatible lattice sizes. Coupling springs are forcing these two networks to coexist, which induces residual stresses. Here we consider two elastic sheets on top of each other of respective area A_{\uparrow} – for the upper sheet – and A_{\downarrow} – for the lower one. The mismatch is defined as :

$$\eta = \sqrt{\frac{A_{\downarrow}}{A_{\uparrow}}} \quad (2.18)$$

We introduce ξ , the coordinate of the undeformed sheet. \mathbf{x}_{\uparrow} and \mathbf{x}_{\downarrow} are the coordinates of the deformed sheets. Each point of the upper sheet is continuously coupled to a point of the lower one. However, because the two sheets do not have the same surface, a point of coordinate ξ in the upper sheet is coupled to a point of coordinate $\eta\xi$ in the lower one:

$$\mathbf{x}_{\uparrow}(\xi) \leftrightarrow \mathbf{x}_{\downarrow}(\eta\xi) \quad (2.19)$$

We are introducing a continuous free energy coupling between the two sheets :

$$F_c = \int \frac{1}{2} \kappa_{\uparrow} [\mathbf{x}_{\uparrow}(\xi) - \mathbf{x}_{\downarrow}(\eta\xi)]^2 dA_{\uparrow} \quad (2.20)$$

where the integral is over the area of the undeformed upper sheet. Due to the mismatch, the point with rest coordinate ξ on the upper sheet is coupled to the point with rest coordinate $\eta\xi$ on the lower sheet. Note that we distinguish the coupling constant of the upper and lower sheets to guarantee the force balance

between the upper and lower sheet. Due to the area mismatch, the coupling constants are not equal. Writing the force balance gives the relation between the coupling constants of the two sheets :

$$\kappa_{\uparrow} dA_{\uparrow} = \kappa_{\downarrow} dA_{\downarrow} \Rightarrow \frac{\kappa_{\uparrow}}{\kappa_{\downarrow}} = \eta^2 \quad (2.21)$$

Each sheet also has its intrinsic rigidity that we characterize by its Poisson ratio and shear modulus: ν and μ , respectively, equal for both sheets. To compute the elastic energy in such a system, we must solve the force balance equation in each sheet:

$$\nabla_{\alpha} \sigma_{\alpha\beta} = f_{\beta} \quad (2.22)$$

We used implicit summation over repeated indices. $\sigma_{\alpha\beta}$ is the stress tensor of the system and f_{β} is the external force applied to a given sheet. In our case, the external force is the coupling force exerted by the other sheet. The stress tensor is related to the strain within the sheet by :

$$\sigma_{\alpha\beta} = \frac{2\mu\nu}{1-\nu} u_{\eta\eta} \delta_{\alpha\beta} + 2\mu u_{\alpha\beta} \quad (2.23)$$

where $u_{\alpha\beta}$ is the usual strain tensor of the upper or lower sheet. The set of equations Eq (2.22), Eq (2.20), Eq (2.23) defines the strain tensor in the system.

We introduce a similar surface tension as described previously by adding a fixed energy cost to the free edges, which we write as:

$$F_{\gamma} = \gamma \int_{\delta A_{\uparrow}} d\ell_{\uparrow} \quad (2.24)$$

At this point, we must emphasize that the surface tension introduced here is isotropic. Which is not the case of the model of discrete particles. We will discuss later the effect of this difference, where the integral runs over the border of the undeformed upper sheet. Finally, we write the total free energy of the system:

$$\begin{aligned} F = & \gamma \int_{\delta\Omega_{\uparrow}} ds_{\uparrow} + \int_{A_{\uparrow}} \left(\frac{1}{2} \lambda u_{\eta\eta}^2 + \mu u_{\alpha\beta}^2 \right) dA_{\uparrow} + \int_{A_{\downarrow}} \left(\frac{1}{2} \lambda u_{\eta\eta}^2 + \mu u_{\alpha\beta}^2 \right) dA_{\downarrow} \\ & + \int_{A_{\uparrow}} \frac{1}{2} [\mathbf{x}_{\uparrow}(\xi) - \mathbf{x}_{\downarrow}(\eta\xi)]^2 dA_{\uparrow} \end{aligned} \quad (2.25)$$

It is possible to compute this integral for a given shape of the two sheets once the strain tensor has been computed. We consider three shapes in Fig 2.9 – An infinite size bulk, a fiber of width \mathcal{W} , and a disk of radius \mathcal{R} . For each shape it is possible

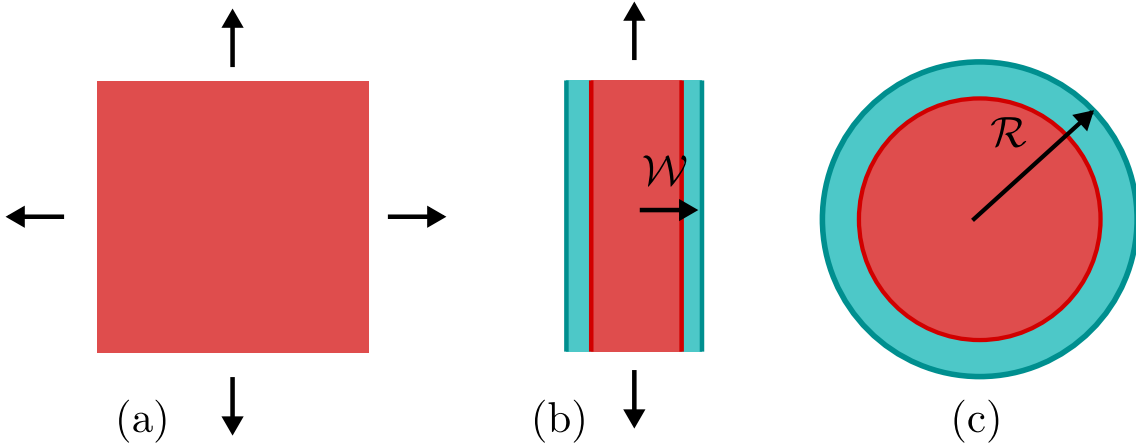


Figure 2.9: **Three shape Ansätze:** (a) bulk shape, (b) fiber shape, (c) disk shape

to compute the free energy per particle as a function of the radius/width. We first introduce several rescaling parameters. We define a characteristic length as:

$$\ell_0 = \sqrt{\frac{\mu}{(1-\nu)\kappa_{\uparrow}}} \quad (2.26)$$

Then the rescaled surface tension:

$$\Gamma = \frac{\gamma}{\ell_0 f_B (1+\nu)} \quad (2.27)$$

The free energy of the bulk configuration is given by:

$$f_B = \mu \frac{1+\nu}{1-\nu} \left(\frac{2\eta}{1-\eta} \right)^2 \quad (2.28)$$

Similarly, we get the free energy per area for a fiber of dimensionless width $W = \frac{\mathcal{W}_{max}}{\ell_0}$

$$\frac{f_F}{f_B} = \frac{\Gamma(1+\nu)}{W} + \left[1 - (1+\nu) \frac{\tanh(W/2)}{W} \right] \quad (2.29)$$

Eq (2.29) is very similar to Eq (2.16). Finally, we write the disk free energy per area of dimensionless radius $R = \frac{\mathcal{R}}{\ell_0}$.

$$\frac{f_D}{f_B} = \frac{\Gamma(1+\nu)}{R} + \left[1 - (1+\nu) \frac{I_0(R) - I_2(R)}{I_0(R) + I_2(R) + \nu(I_0(R) - I_2(R))} \right] \quad (2.30)$$

where I_0 , I_2 are, respectively, the first and second modified Bessel functions. The

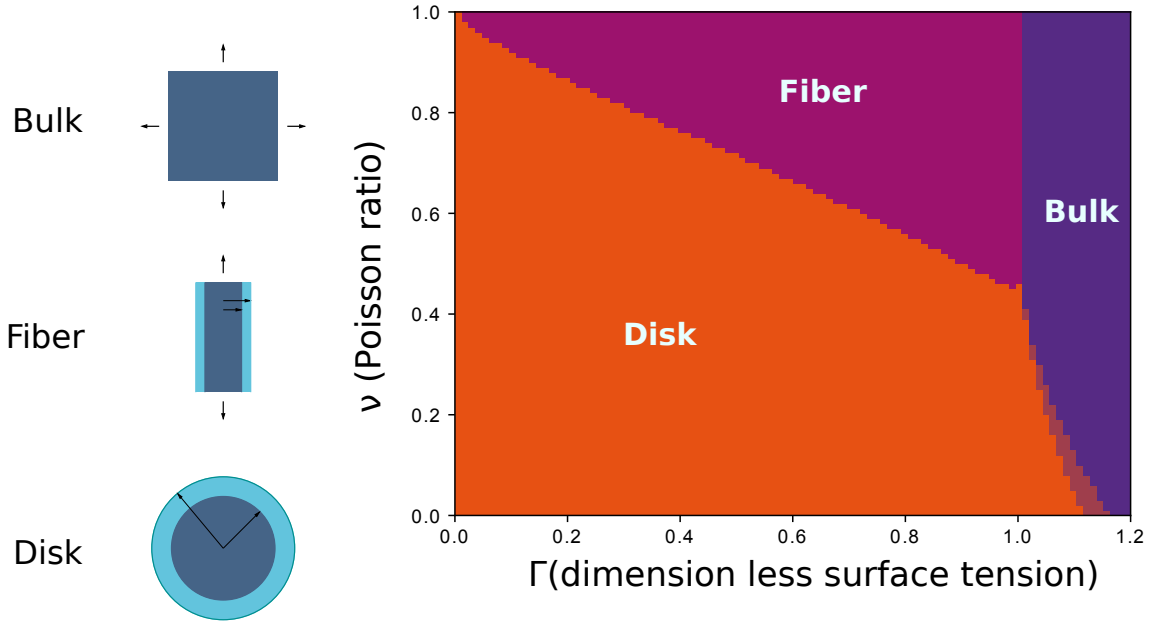


Figure 2.10: **Continuum Phase diagram** : for a given value of Γ and ν we plot what is the shape with the minimum energy among the three ansatz. In the shaded purple region, the absolute minimum energy is in $\mathcal{R} \rightarrow \infty$, but a local minimum of energy still exists at finite \mathcal{R} .

computation of the energy for the three different types of ansatz -disk/fiber/bulk- reveals that two parameters are sufficient to determine the equilibrium shape: Γ and ν . Fig 2.10 gives the stability domain of each shape considered. Similar to the square model, we observe the emergence of self-limiting aggregation through the same mechanism of a free boundary that allows for the relaxation of the stress over a lengthscale ℓ_0 . We observe the emergence of equilibrium fibers as the Poisson ratio of the sheets increases.

In this model, a mutual coupling between two elastic sheets induces residual stress in the structure. Similar to the square model, the stress is allowed to relax on the border of the aggregate over a characteristic lengthscale ℓ_0 that depends on the mechanical characteristics of the sheets. The emergence of this lengthscale corroborates with the emergence of an equilibrium size for the elastic sheets. Moreover, we observe that when the Poisson ratio increases, the sheets prefer limiting their size only in one dimension and fibrous structures emerge. The particles previously introduced exhibit a similar incompatibility, which takes the form of two spring networks with different lattice sizes. For these reasons, we expect the particle model to exhibit the same phenomenology.

Chapter 3

Shape Ansatz phase diagram

In the previous chapter, we introduced a coarse-grained model for frustrated self-assembling particles. The shape of these particles prevents tight packing without deformation. Deformation of the particles is enabled at the cost of an elastic energy modeled by harmonic springs. We noticed that a large aggregate of particles can be decomposed into two networks of incompatible lattice size, yet coupled by harmonic springs. A continuum version of this idea enabled us to compute a phase diagram based on three Ansätze of shape. The phase diagram reveals three important phenomena. Firstly, the emergence of a characteristic lengthscale, which depends on the mechanical characteristics of the elastic sheets. This lengthscale is responsible for the stabilization of the sheet over a fixed size. Secondly, this size limitation can happen in only one dimension, which leads to fibrous structures. Thirdly, the Poisson ratio is the parameter that triggers the transition from isotropic size limitation to fibrous structures. In this chapter, we use numerical methods to check the consistency between the continuum model and both triangle and hexagonal particle models. To do so, we first have to establish a mapping between the discrete and continuum parameters in section 3.1. Once this is done, we will introduce the algorithm we use to compute the elastic energy of any given structure of the aggregate in section 3.2. We will then have to build a discrete equivalent of the three Ansätze of shape used in the continuum model. The details of the shape used will be presented in section 3.3. Finally, we present and compare the different phase diagrams in section 3.4.

3.1 Mapping of the parameters

In the coupled elastic sheets model, we introduced 2 dimensionless parameters: the rescaled surface tension Γ and the Poisson ratio ν of the individual sheets. We also derived a unit energy and a unit length: f_B, ℓ_0 . The particle models only have

three parameters: k the main spring stiffness, κ the coupling spring stiffness and J the energy cost per free edge. In a large aggregate, the main springs of the particles form two coupled triangular spring networks. It turns out that a triangular spring network has a fixed Poisson ratio of $1/3$. This means that we can only explore a line of the phase diagram in Fig 2.10. Moreover, the continuum model predicts that no fiber should be stable for $\nu = 1/3$. To overcome these limitations and allow for a broader exploration of Poisson ratio, we add a quadratic energetic cost to the change in area of the red -small- and green -big- triangles represented in Fig 2.4 :

$$E_{\text{Area}}^{\pm}(A^{\pm}) = \frac{k_A}{A_0^{\pm}}(A^{\pm} - A_0^{\pm})^2 \quad (3.1)$$

Where \pm refers to the (+) big triangle -green- or (-) small triangle -red-, A^{\pm} is the area of the triangle, A_0^{\pm} is the rest area of the big or small triangle and k_A is the area stiffness. The Poisson ratio is associated to the compressibility of a material and in 2D, when $\nu = 1$ means incompressible material, we expect thus $\nu \xrightarrow[k_A \rightarrow \infty]{} 1$. With this definition of the area energy, we can compute the Poisson ratio and shear modulus of the triangular network as a function of k and k_A [45]:

$$\nu = \frac{\sqrt{3}k + 2k_A}{3\sqrt{3}k + 2k_A} \quad (3.2)$$

$$\mu = \frac{\sqrt{3}}{2}k \quad (3.3)$$

This allows us to write the bulk free energy using Eq (2.28):

$$f_B = \frac{1}{A_0^{\pm}}(3k + \sqrt{3}k_A)\epsilon^2 \quad (3.4)$$

We now want to establish a link between the coupling springs -blue springs in Fig 2.4- and the continuum coupling Eq (2.20). To do so, we need to compute the force density applied by the coupling springs. Equating the two energy densities on each spring network gives the mapping between κ , and k_c for each type of particles :

$$\kappa = \frac{\sqrt{3}}{1 - \epsilon^2}k_{c,\text{Hex}} \quad (3.5)$$

$$\kappa = \frac{4\sqrt{3}}{(1 + \epsilon)^2}k_{c,\text{Tri}} \quad (3.6)$$

where $k_{c,\text{Hex}}$ refers to the coupling constant in the hexagonal model, and $k_{c,\text{Tri}}$ is the coupling stiffness in the triangular model. The mapping between the triangular and hexagonal models are different because the number of coupling springs

as well as their respective orientations differ between the two models. Finally, the dimensionless surface tension can be found by using the relation between the constant cost per free edge J and the continuous surface tension γ :

$$J = \gamma l_{\text{edge}} \quad (3.7)$$

where the length of a free edge is: $l_{\text{edge}} = \sqrt{1/3 + \epsilon^2}$ for the hexagon and $l_{\text{edge}} = 1 + \epsilon$ for the triangle. Eq (3.3), Eq (3.4), Eq (3.6) give access to the parameters of Eq (2.26) and Eq (2.27) to compute Γ and ℓ_0 for each model.

3.2 The algorithm

The continuum phase diagram relies on the comparison of the energy of the shape Ansätze. The Poisson ratio and the surface tension are the two relevant parameters to determine the shape with the lowest energy. Now that we have a mapping between the parameters of the particle and continuum model, we can use the same procedure. The major difference in the particle model is that we do not have an analytical formula of the energy. We thus simulate the aggregates.

3.2.1 Topology relation

An aggregate is an ensemble of neighboring particles on a lattice. We create a mapping between a 2D array of Boolean numbers and a structure of the aggregate as represented in Fig 3.1. To define such a mapping between a square network – the 2D Boolean array – and a triangular or hexagonal one, we have to define a neighboring relation. Considering an entry (i, j) of the Boolean array, we define the neighbors of (i, j) in the hexagonal lattice as :

$$\mathcal{N}_{\text{Hex}}(i, j) = \{(i + 1, j), (i, j + 1), (i - 1, j + 1), \\ (i - 1, j), (i, j - 1), (i + 1, j - 1)\} \quad (3.8)$$

And for the triangular lattice :

$$\mathcal{N}_{\text{Tri}}(i, j) = \begin{cases} \{(i + 1, j), (i - 1, j), (i, j + 1)\} & \text{if } i+j \text{ is even} \\ \{(i + 1, j), (i - 1, j), (i, j - 1)\} & \text{if } i+j \text{ is odd} \end{cases} \quad (3.9)$$

Once we have defined the topology of the aggregate, we can compute its associated energy. Concerning the surface tension energy, the number of free edges is simply the number of non-occupied neighboring sites for each occupied site. Multiplying the number of free edges by J gives the surface energy. The computation of the elastic energy is detailed in the next section.

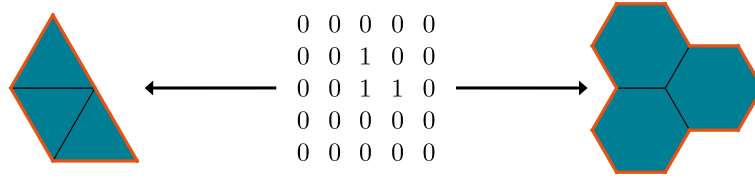


Figure 3.1: Mapping between Boolean array and aggregate structure

3.2.2 Equilibration of an aggregate

In this section, we give details about the way we compute the elastic energy of an aggregate given its topology. The details are given in the example of the hexagonal model but can easily be generalized to the triangular model. An aggregate is a collection of tightly packed particles. Each particle has a proper elasticity modeled by a spring network. Tight packing of particles requires to merge the nodes of two neighboring particles as seen in Fig 2.4 (g,h,i). To compute the elastic energy of an aggregate, we must first compute which nodes are merged. To do so, we use a smart labeling of the nodes. Nodes are labeled with a triplet of numbers: (i, j, k) . (i, j) refers to a given site, and k to a specific node of this given site, as represented in Fig 3.2 (a) for the hexagonal lattice. This way, a triplet of integers (i, j, k) defines a unique node. However, a node is not defined by a unique triplet. Fig 3.2 (b) and (c) shows the several triplets that represent the same node. We use these properties to build the nodes of an aggregate given its topology. All nodes are arranged into a map whose key is a triplet of integers and reciprocally each node is associated with 3 keys. By iterating over all occupied sites, we check if the nodes of the associated site exist. If not, we create them and arrange it according to its three keys. Once all nodes are created, we can similarly create the associated springs. At this point, the aggregate is a spring network. The strain in the aggregate corresponds to the displacements of the nodes. We can define the elastic energy of an aggregate as a function of the nodes' positions denoted $\{\mathbf{x}_i\}$ as:

$$\begin{aligned}
 E_{\text{el}}(\{\mathbf{x}_i\}) &= \frac{1}{2} \sum_{\langle i, j \rangle} k [|\mathbf{x}_i - \mathbf{x}_j| - (1 - \epsilon)]^2 \\
 &\quad \frac{1}{2} \sum_{\langle i, j \rangle} k [|\mathbf{x}_i - \mathbf{x}_j| - (1 + \epsilon)]^2 \\
 &\quad \frac{1}{2} \sum_{\langle i, j \rangle} \kappa [|\mathbf{x}_i - \mathbf{x}_j| - l_c]^2
 \end{aligned} \tag{3.10}$$

where $|\cdot|$ denote the norm of a vector, $\langle i, j \rangle$, $\langle i, j \rangle$, and $\langle i, j \rangle$ respectively denote the sum over nodes i and j that are bound by a small, big, and coupling spring. l_c is the rest length of the coupling springs, which is different for the trian-

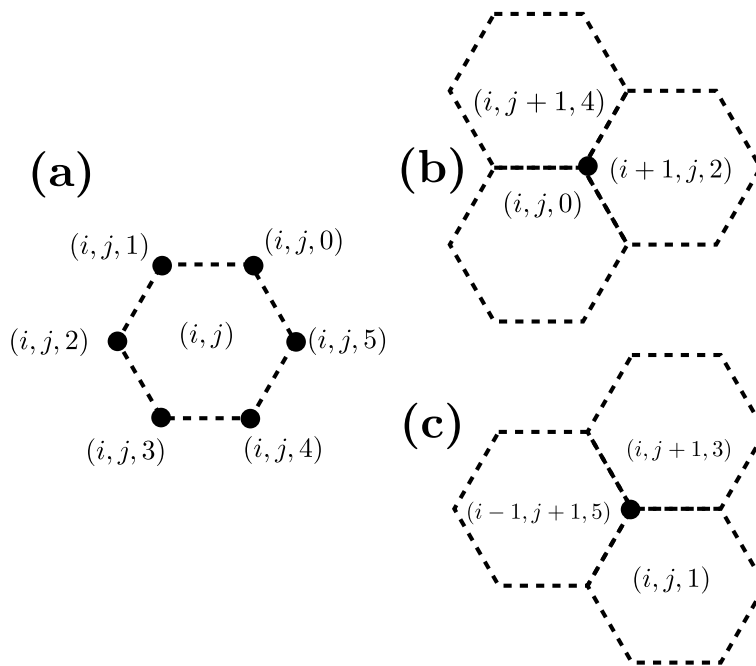


Figure 3.2: **Smart labeling of the nodes** : (a) The nodes' labels are given for the site (i, j) . (b) Notice that the node $(i, j, 0)$ is also associated to the label: $(i, j+1, 4)$ and $(i+1, j, 2)$. (c) Similarly, the node $(i, j, 1)$ is associated to $(i-1, j+1, 5)$, $(i, j+1, 3)$.

gular and for the hexagonal model. The elastic energy of an aggregate is defined as the minimum of E_{el} over the nodes' positions. To simulate an aggregate, we wrote a C++ program as a Python module using ctypes – a library for interfacing C and Python. The Python program manages the topology of the aggregate, i.e. which particle is neighbor to which other. The C++ program receives an array of Booleans as an input and creates the corresponding nodes and springs as C++ objects. Once all objects are built, it uses a nonlinear conjugate gradient algorithm to minimize the elastic energy over every nodes' position. With this program, we can compute the energy of any aggregate, let us now see how we can build a similar phase diagram to the one in section 2.3

3.3 Discrete Ansatz of shape

To build a similar phase diagram as in Fig 2.10, we have to design similar Ansätze of shapes than the ones used in the continuum model and represented in Fig 2.10 but using discrete particles for both triangle and hexagonal models. The discreteness of the model brings possibilities of new shapes that we present in this section.

3.3.1 Continuum disk to discrete hexagon

We identify two types of disk-like aggregate structures. On the one hand, an hexagonal structure that follows the lattice vector as represented in Fig 3.3 (a)-(c). On the other hand, a disk structure where particles beyond a fixed distance from a center point are depleted as shown in Fig 3.3 (b)-(c). For any value of the parameters, it turns out that the structure of minimum energy is always the hexagonal structure rather than the disk one. Their elastic energy per particle is almost the same while the surface tension per particle of the hexagonal disk is smaller than the one of the disk's structure. This is due to the anisotropy of the surface tension of the particles. The shape that minimizes the surface tension is thus not a disk but a compromise between surface minimization and alignment with the lattice vector that can be found using the Wulff construction [44].

3.3.2 Numerical infinite fiber

We define the fiber for the triangular model with the representation in Fig 3.4 (a). Concerning the hexagonal model, we found three types of fibers shown in Fig 3.4 (b)-(c)-(d). Similar to the disks, one fiber turns out to always have a smaller energy than all others: the one represented in Fig 3.4 (b). We will only use this one. Notice that unlike the ones in Fig 3.4 (c)-(d), the fiber in Fig 3.4 (b) is bent, which may appear as an additional mode of relaxation of the stress.

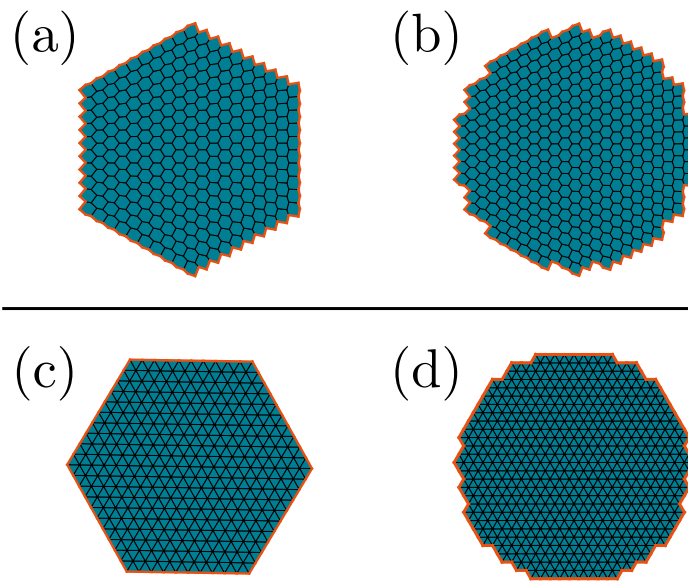


Figure 3.3: **Ansatz of disk structures** : (a) Hexagonal disk of the hexagonal particle model. (b) Disk shape of the hexagonal model. (c) Hexagonal disk of the triangle particle model. (d) Disk shape of the triangle model.

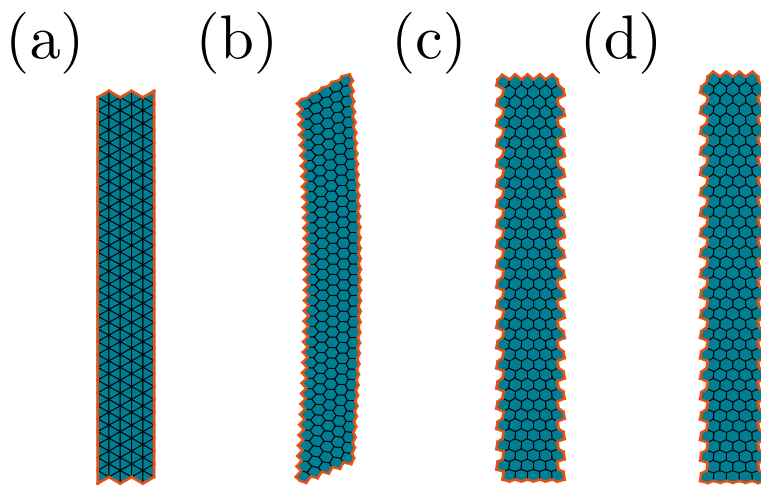


Figure 3.4: **Ansatz of fiber structures** : (a) Triangle type of fiber of width $W = 5$. (b) hexagonal bent fiber of width $W = 5$, which is the most stable one. (c)-(d) Two other type of hexagonal fiber of width $W = 5$.

Simulated fibers cannot be infinitely long, to overcome this limitation, we use an extrapolation of the energy of the fiber to an infinite length that we detail here. The difference between a fiber of finite length and a fiber with infinite length is

the tip of the fiber. The Energy of the tip of a fiber only depends on the width of the fiber. Therefore, the energy per particle of the tip of the fiber scales as $e_{\text{tip}}(L, W) \propto \frac{W}{L}$ where W is the width of the fiber and L its length -in number of particle units-. We simulate three fibers for three different aspect ratios $\mathcal{A} = \frac{W}{L}$: $1/3$, $1/5$, and $1/10$. We then plot the energy of the fibers as a function of the aspect ratio and fit it with a line as represented in Fig 3.5. The vertical intercept at the origin correspond to the energy of an infinite length fiber.

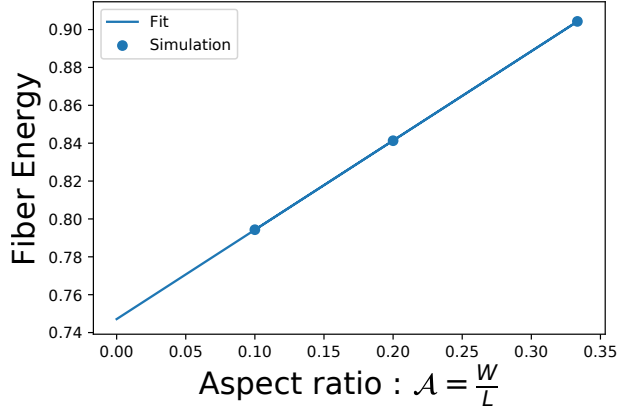


Figure 3.5: **Extrapolation to infinite fiber** : We plot the energy of finite length fibers as a function of their aspect ratio. The linear fit is also represented. Energies are in bulk energy unit.

3.3.3 Sparse bulks

Finally, we consider infinite bulks with holes in the structure, that we call sparse bulk. Sparse bulks also offer a compromise between surface tension and elastic frustration and are thus a good candidates for intermediate surface tension. We consider three types of sparse bulk for the hexagon and one for the triangles as represented in Fig 3.6, each with a different density of holes. Note that the first bulk in Fig 3.6 (a) is unfrustrated, and constitutes the best aggregate at very low surface tension.

3.4 Phase diagram

The phase diagram obtained by comparison of the energy of the various Ansätze that we presented in section 3.3, is given in Fig 3.7. To construct every point of the phase diagram -one value of Γ and ν per point-, we compute the energy of the fibers and disks with increasing size/width until a local minimum is found. If

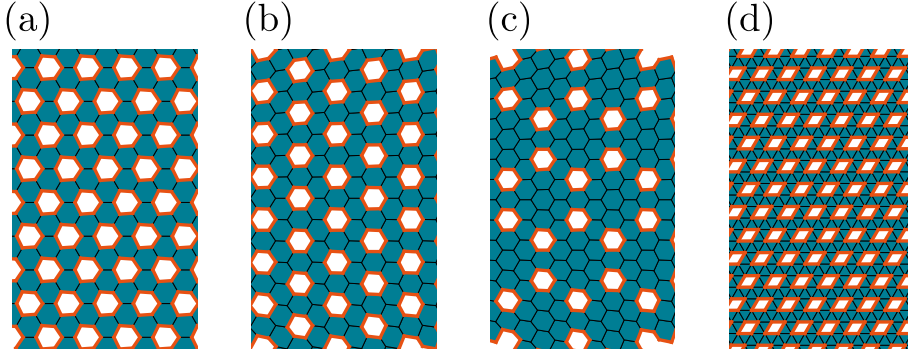


Figure 3.6: **Ansatz of sparse bulk structures** : (a,b,c) Hexagonal sparse bulk with decreasing density of hole. (a) is an unfrustrated structure. (d) sparse bulk for triangle lattice.

no local minimum exists, the energy is guaranteed to decrease with size up to the bulk energy. The color of the points give the aggregate with the lowest energy. Both phase diagrams are plotted with $\epsilon = 0.01$. To make sure that linear elasticity applies, we try to keep the deformation small. The deformation of a particle associated with the transition from an isolated particle to a bulk configuration requires a displacement of the nodes of the order of ϵ . However, the deformation accumulates at the border of the aggregate as the number of aggregated particles increases. Therefore, to keep the deformation small, we need to keep both ϵ and the size of the aggregates small. We used $\ell_0 = 5$ for both phase diagrams. ℓ_0 is the width of the stress relaxation boundary layer in number of particle units. As ℓ_0 increases, the discreteness of the unit less size of a particle: δ/ℓ_0 goes to 0, and the particle model approaches the continuum limit. Note, however, that as ℓ_0 increases, the size – in number of particles unit – of the equilibrium aggregates increases too. The simulation time increases rapidly with the number of aggregated particles which limits the possible value of ℓ_0 we can use.

Despite the similarities between both the discrete phase diagram and the continuum one, many differences deserve to be pointed out. First, the minimum value of Poisson ratio required to stabilize fibers over disks is $\nu = 1/2$ for the continuum model and turns out to be around $1/3$ for both discrete models. One reason for this enhanced stability of the fibers over the disks could be that the disks are not exactly circular, therefore the surface energy should be a little higher than perfect disks. Second, the fiber region of the hexagonal model is bigger than the triangle one at high Poisson ratio. This suggests that the bending of hexagonal fibers is a supplementary mode of relaxation of the stress that is only accessible to fibrous aggregates.

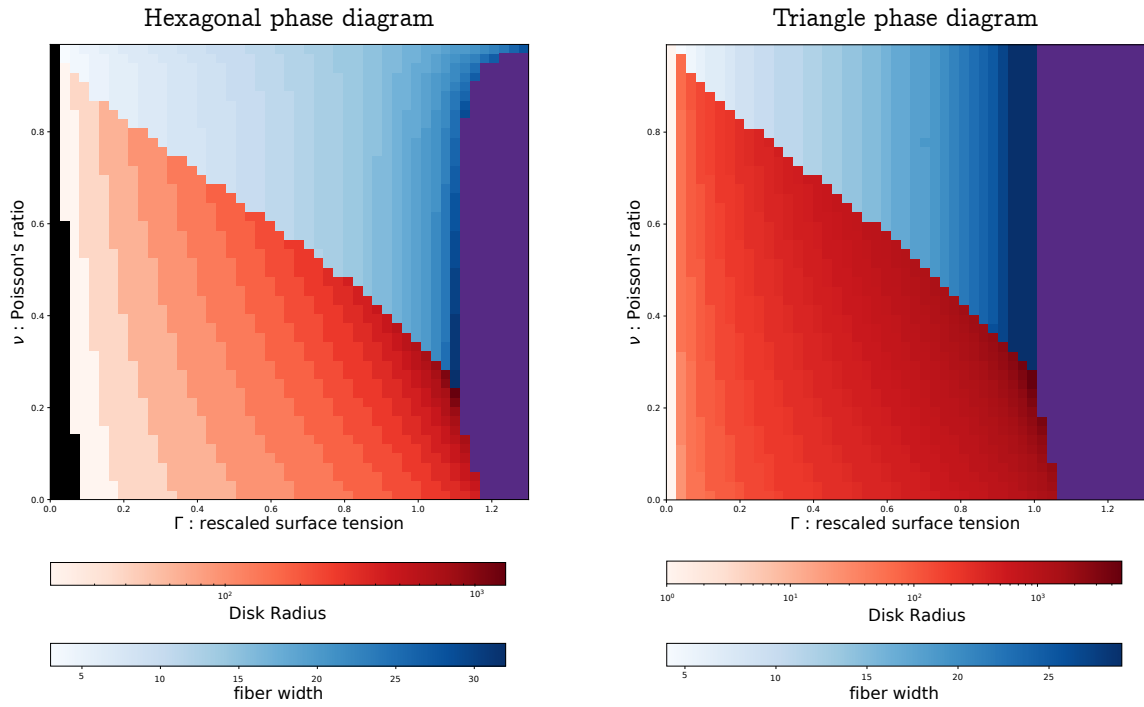


Figure 3.7: **Discrete phase diagrams** : The region where the disks structures have smaller energy than any other aggregate is colored in red, while blue is for fiber, purple for bulk, and black unfrustrated sparse bulk represented in Fig 3.6 (a). First we remark that except the unfrustrated sparse bulk, no other sparse bulk appears to be more stable than fiber, or disk. Second, as Γ increases, every color becomes darker, which means that the aggregates grow in size. This is expected as surface tension penalizes particles at the surface. The relative contribution of surface particles to the energy of the whole aggregate decreases with the aggregate size. The size increases of the disk is so steep close to the bulk transition that we use a logarithmic scale for red color coding.

Chapter 4

Monte-Carlo simulated annealing

The phase diagrams built in the previous section stand on preconceived Ansätze of shape. The validity of the diagrams depends on the diversity of shapes considered. Maybe other better structures, that we have not thought of, have a lower energy. One strategy would be to push the exploration to a broader variety of structures by enumeration of Ansatz. In the case of square particles, a current enumeration of structures made of n particle gives an approximate scaling of N_n . [46] :

$$N_n \propto \frac{\lambda^n}{n} \tag{4.1}$$

where $\lambda \sim 4$ a numerical estimate gives $\lambda \approx 3$, and is N_n the number of possible polyominoes made of n square particles. This number diverges exponentially as the number of particles increases. Considering that some points of the phase diagram in Fig 3.7 involve a thousand particles means that an enumeration of the possible shapes is unrealistic. Instead, we are going to use an unbiased optimization procedure called simulated annealing Monte Carlo. Physicists are familiar with Monte Carlo simulation that is an efficient way to simulate equilibrium thermodynamic ensembles. Monte Carlo simulated annealing, however, is an optimization procedure that can display remarkable convergence performance, especially in systems with proliferating local minimum. In the following section 4.1, we are going to recall the basic assumptions required to guarantee the convergence of simulated annealing toward a energy minimum. We then present how we implemented the algorithm in section 4.2, and explain how we can restrain the phase space to improve the convergence of the algorithm in section 4.3. Finally, we present and criticize the results of the simulations in section 4.4.

4.1 About simulated annealing in general

We start by introducing simulated annealing Monte Carlo from a mathematical perspective. We recall the assumptions required to guarantee the convergence toward the ground state. Although, no statement is provided related to the convergence speed of the algorithm.

Let us consider n particles -triangles or hexagons- on a lattice in a box of volume $V \in \mathbb{N}$, in number of available sites. Let Ω be the phase space of such a system, i.e., the ensemble of all possible positions for the particles. A state is given by a set of positions of particles on a lattice. $\pi_i(T)$ is the equilibrium probability that the system is in the state i at temperature T . In a Monte Carlo simulation, we propose moves from a state $i \rightarrow j$ with a probability p_{ij} , and accept this proposition with a probability $\alpha_{ij}(T)$. We assume the symmetry of the proposal of the moves :

$$p_{ij} = p_{ji} \quad (4.2)$$

To ensure that Ω is a connected space, the matrix P , whose entries are the p_{ij} s has to be irreducible. This means that every state i is accessible through any state j via a sequence of intermediate states. Concerning the acceptance probability, we use the Metropolis criterion :

$$\alpha_{ij} = \min \left(1, \exp \left[\frac{E_i - E_j}{T} \right] \right) \quad (4.3)$$

With these assumptions, we can show [47] that the equilibrium distribution probability satisfies :

$$\pi_i = \pi_j \alpha_{j,i} \quad (4.4)$$

If the states i are sorted by increasing energy values - E_0 is the lowest energy-. We can use Eq (4.4) for $i = 0$ with $\alpha_{j,0} = 1$ and thus :

$$\forall j \neq 0 \quad \pi_j = \pi_0 \alpha_{0,j}(T) \quad (4.5)$$

From Eq (4.3), we have $\alpha_{0,j} \xrightarrow{T \rightarrow 0} 0$, which means $\pi_0 \xrightarrow{T \rightarrow 0} 1$. Which guarantee the convergence of the annealing procedure to the ground state. However, we must notice that this reasoning does not say anything about the speed of convergence or the condition on the evolution of the temperature T . In fact, being able to predict the convergence speed of the simulation requires deeper knowledge of the system, the energy landscape, and the topology of the phase space. Because such a knowledge is inaccessible, we will optimize the convergence using empiric rules.

4.2 Implementation of the simulated annealing

As explained in section 3.2, the energy of a set of particles depends on two types of variables. A first discrete set that corresponds to the structure of an aggregate, and a second continuum set of variables that correspond to the position of each node. The first is represented as a Boolean array treated by a Python program, while the second is an array of real numbers treated by a C++ program. Once the structure of an aggregate is given, the corresponding elastic energy is computed by minimizing the spring energy over the position of the nodes using a conjugated gradient algorithm as explained in section 3.2.2. The Monte Carlo simulation optimizes the structure of an aggregate to minimize its energy. The Monte Carlo simulation only deals with the Boolean array that is used as an input for the computation of the elastic energy, irrespective of the particle type used – hexagonal or triangular –. Therefore, in the following, the reader should keep in mind that the temperature only affects the position of the particles on the lattice, and not the position of the nodes.

We start by defining a canonical simulated annealing. We consider a large array of Booleans, of size $L \times L = V$. It corresponds to the box in which N particles are living. If two or more particles are neighbors, they form an aggregate. Each aggregate is a distinct C++ object. A Monte Carlo move consists in :

1. Select a random particle uniformly and remove it.
2. Select a random free site uniformly and add a particle in it.
3. Actualize the energy of each affected aggregates.
4. Accept or refuse the move according to the Metropolis criterion.
5. actualize the temperature.

We verify that the assumptions of section 4.1 are verified by illustrating such a move in Fig 4.1. The probability to delete a specific particle is the same for all particles: $P_{\text{delete}}(i) = 1/N$. The probability to add a particle in a specific site is the same for all sites: $P_{\text{add}} = 1/(V - N)$ Therefore the probability to propose the move $i \rightarrow j$ and $j \rightarrow i$ or both equal to :

$$p_{i,j} = p_{j,i} = \frac{1}{N(V - N)} \quad (4.6)$$

The acceptance probability is given by Eq (4.3) which is symmetric too. As explained in section 4.1 this properties are enough to guarantee the convergence.

The convergence criterion we just derived relies on the assumption that enough Monte Carlo steps are performed at a given temperature to reach the equilibrium

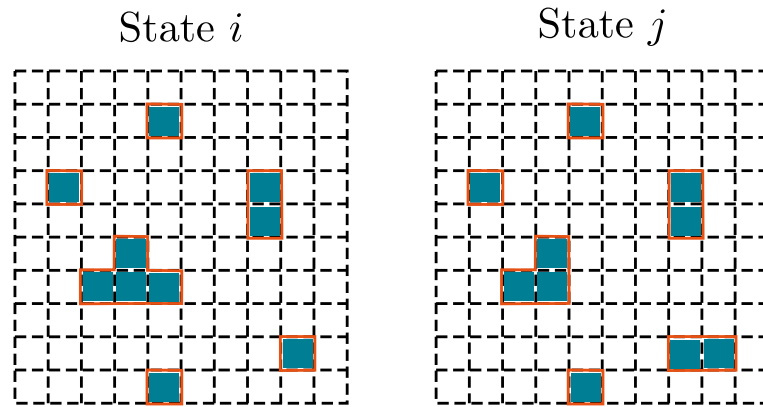


Figure 4.1: **Canonical Monte Carlo move** : A move from state i to j takes place by removing a random particle chosen uniformly, and adding one particle on a random free site chosen uniformly. The moves are performed on a 2D lattice of Booleans in a similar way for the triangular and for hexagonal model.

distribution. Moreover, the convergence of the equilibrium distribution – as the temperature decreases – to the ground state is ensured, but no statement is made on how slowly the temperature must be decreased. In reality, as it is often the case for frustrated systems, we expect the energetic landscape of our system to be made of many local minimums. As the number and depth of these local minimums increase, the speed of convergence of the simulated annealing decreases. For these reasons, we do not expect the Monte Carlo simulated annealing to provide an unambiguous answer regarding the ground state of our system. Instead, we will be interested in the common features of the different outputs. Nonetheless, in the next section, we design another algorithm that may help us to approach the ground state faster.

4.3 Restricting the phase space to improve efficiency

In this section, we use our physical intuition to improve the efficiency of the algorithm. In addition to the usual canonical Monte Carlo simulated annealing –fixed number of particles, fixed volume, we designed a Monte Carlo algorithm that focuses on studying the structure of the aggregate rather than the aggregation process. In this algorithm, we simulate N particles while forcing them to stay connected into a single aggregate. We call this algorithm Yielded Monte Carlo Algorithm -YMCA. Similarly than before, a Monte Carlo move consists in removing one random particle chosen uniformly, and the addition of a new particle

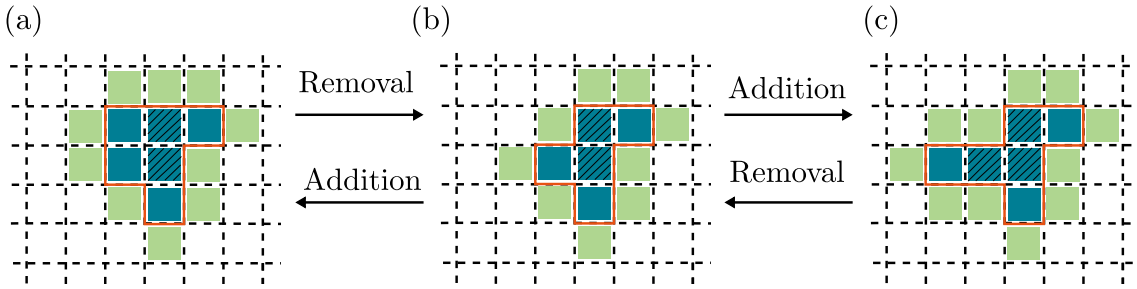


Figure 4.2: **YMCA moves** : We represent particles as blue squares on a lattice. The dash blue particles are frozen since their removal would lead to the breaking of the aggregate. The surface of the aggregate is underlined by an orange line. The free sites, in the vicinity of the aggregate, where a particle can be added are colored in green.

in a position chosen uniformly. However, to ensure the contiguity of the aggregate throughout the simulation, we impose a constraint on each of the subsequent moves. First, concerning the removal of a particle: if the aggregate is broken after removing a particle, the move is systematically rejected. Second, concerning the addition of a particle: it has to happen in the direct vicinity of the aggregate to make sure that no new aggregate is formed. We now show that this process respects the detailed balance by showing that the proposal of the move and the proposal of the reversed move are equal. As shown in Fig 4.2, the symmetry of the moves means comparing the probability to execute a move from (a) to (c) and the probability to execute the reverse move from (c) to (a). Concerning the removal move, every particle is picked with the same probability: $P = 1/N$ where N is the total number of particles. Because the number of particles is the same in state (a) and state (c), the probabilities are equal. Concerning the following addition of a particle, it always occurs in the intermediate situation in Fig 4.2 (b). The number of available sites -green sites- is thus the same, and so is the probability of adding a particle in one of the random green squares. We thus have the Eq (4.2) satisfied.

This algorithm is going to be specially interesting to investigate the region of the phase diagram where we expect fibrous structures to emerge. Indeed, a fiber made of N particles has a length of order N . To be able to assemble such a fiber in a regular canonical simulation, we need a box of size N^2 . The density of particles thus decreases as $\rho \propto 1/N$, $N \sim 100$, which already gives an extremely low density. Low density makes the process of aggregation extremely slow and computationally costly, which limits our ability to simulate fibers.

4.4 Comparing Monte-Carlo results and shape Ansätze

The resulting shapes of the Monte Carlo are not as well defined as the shape ansatz. To make an understandable comparison, we will be testing three tendencies. Starting with the increase of radius size of disk-like shape with the value of Γ at low ν , we will then study the increase of fiber width with Γ at high ν . We will finally test how increasing ν leads to increasingly fibrous aggregates.

Unlike the usual Monte Carlo simulations, thermal averages are impossible in simulated annealing. The main goal of simulated annealing is to find the configuration of minimum energy. Repeating a simulation would give several configurations with different energies. The winner is the one with the smallest energy. However, we want to ensure that all configurations with an energy comparable to “the winner” also share common features. In the following, we present one instance of the final configuration, while keeping in mind that the main features (size of the finite aggregate, width of the fibers) are reproducible.

4.4.1 Increase in radius with Γ

We start by looking at the evolution of the size of the disks at a low Poisson ratio ($\nu = 0.4$) as a function of Γ . It corresponds to a line in the phase diagram obtained in Fig 3.7. The expected behavior is to see a finite disk with increasing size as Γ increases. Here we want to simulate the aggregation process, which is why we use the usual canonical Monte Carlo simulated annealing with a fixed number of particles in a box with fixed boundary conditions. The evolution of the cluster size is given in Fig 4.3 with the shape Ansatz prediction as a comparison. The expected tendency is well reproduced; however, our ability to aggregate particles in a Monte-Carlo simulation remains limited. In any case, the energies of the simulated Ansätze are almost always smaller than the Monte-Carlo aggregates, which means better. The pictures corresponding to the graph’s points are shown in Fig 4.4 for hexagons and in Fig 4.5 for triangles. Each aggregate is treated as an independent object, living in a different world, as long as they do not interact. The plotting procedure consists in plotting each of them in their own space and then combining all these plots in a single figure. This can lead to stacked aggregates on top of each other. In any case, the orange line provide a guide for the boundary of an aggregate to avoid confusion. We notice in Fig 4.4 that the aggregates are sometimes connected. The assembly of two hexagonal particles is unfrustrated, therefore, it is always possible to connect two aggregates without introducing any frustration. These bridges do not appear in the triangular model in Fig 4.5.

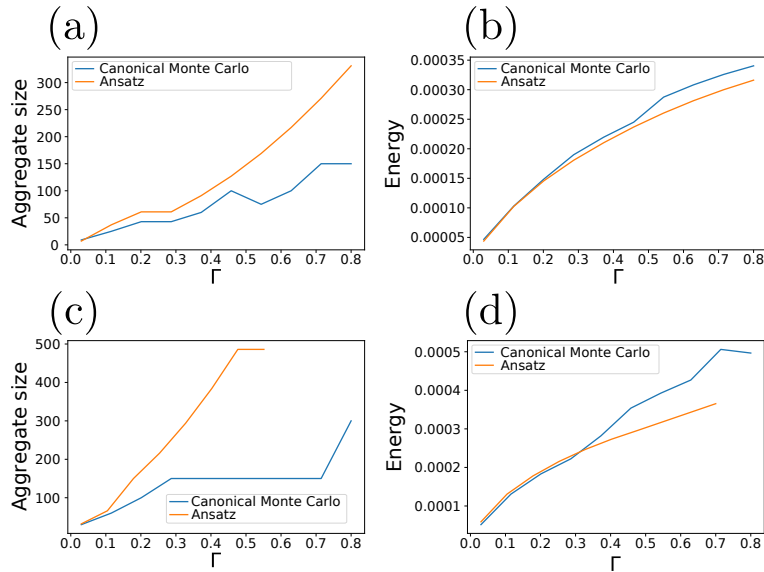


Figure 4.3: **Small Poisson ratio comparison** : (a-b) Hexagonal particles. (c-d) Triangle particles. (a,c) give the size of the best aggregate for the Monte Carlo and ansatz simulation. (b,d) gives the corresponding energy. Notice that the ansatz simulation is always better than the simulation. As the number of particles increases, the phase space increases exponentially. These effects makes the aggregation of the particles more costly in terms of Monte Carlo moves. (c) We notice a stagnation of the aggregate size as Γ increases. This is due to the finite number of particles simulated, in this case 300 particles. If the best aggregate is made of 200 particles, then the system can only achieve at best one aggregate of 200 particles and another one of 100 particles, which gives 150 particles in average.

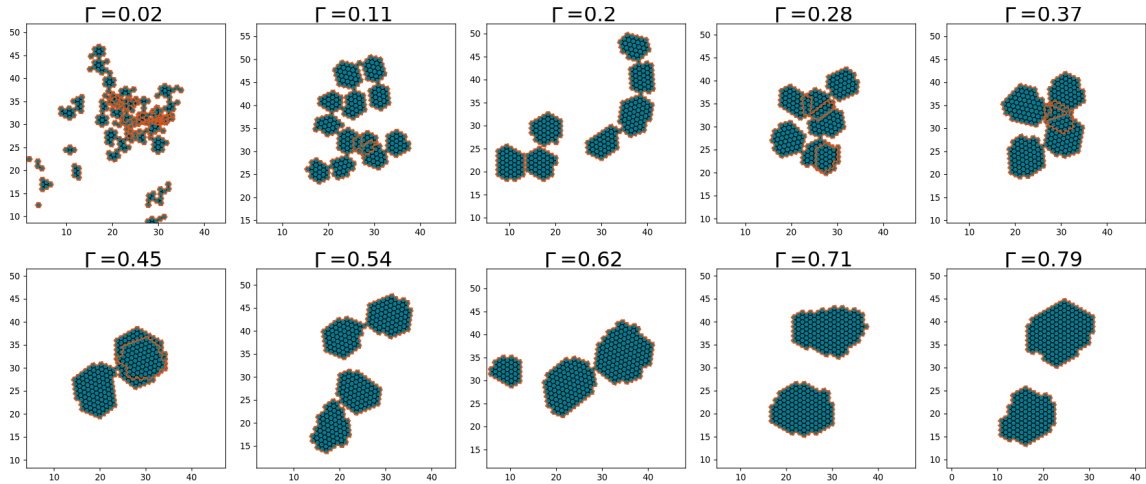


Figure 4.4: **Size of finite disks made of hexagons** : Each plot is the final result of a simulated annealing. There is $N = 300$ particles, $\nu = 0.4$, $\ell_0 = 5$, and the value of Γ is given as a title. The picture is the result of a total of 10^6 time steps, which takes approximately 3 days to compute. The computation time limits our ability to slowly cool down the system, or to increase the number of simulated particles.

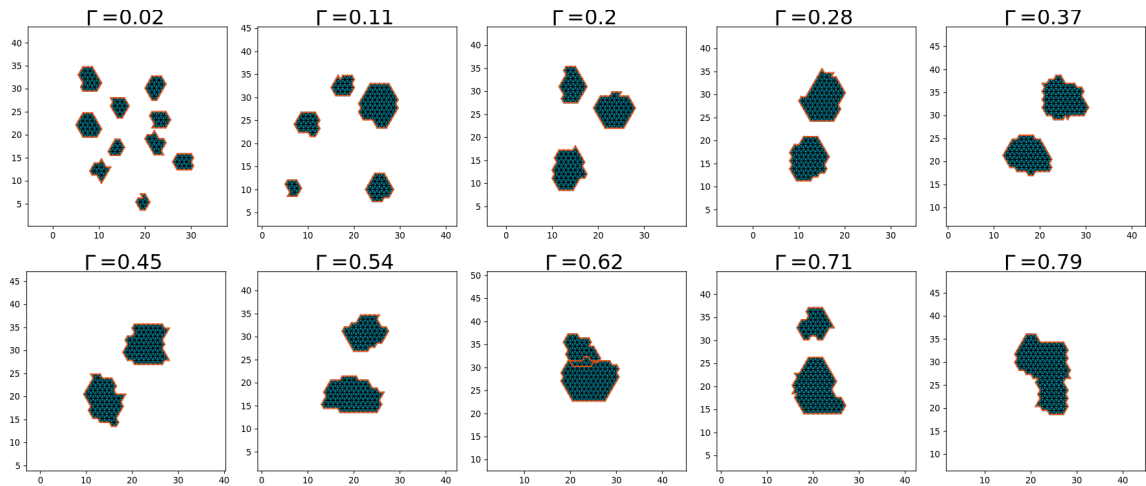


Figure 4.5: **Size of finite disks made of triangles**: Each plot is the final result of a simulated annealing. There is $N = 300$ particles, $\nu = 0.4$, $\ell_0 = 5$, and the value of gamma is given as a title. There is a total of 10^6 time steps

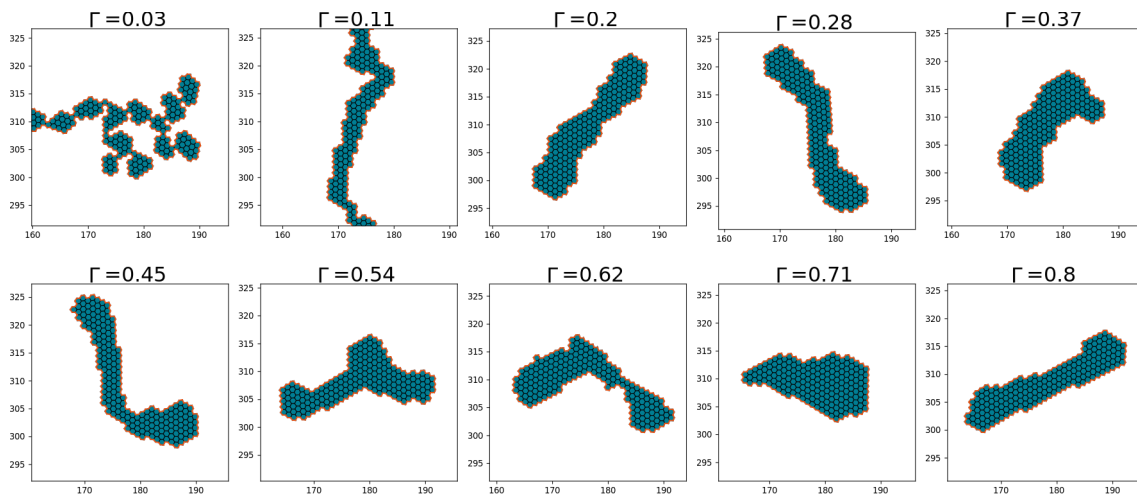


Figure 4.6: **Evolution of fiber width with Γ for hexagons:** Snapshot of final states of YMCA annealing. $\nu = 0.9$, $l_0 = 5$. The simulations are the result of $2 \cdot 10^4$ time steps with 200 particles. We notice that at very small surface tension, the aggregate is not a fiber. The YMCA algorithm gives a grape of small disks, connected together.

4.4.2 Increase in width with Γ

We now have a look at the formation of fibers at high Poisson ratio, which is predicted by our previous models. In this case, we are more interested in the shape of the aggregates rather than their size. As explained before, the canonical Monte Carlo algorithm has to be used in a very large box to provide enough space for a fiber to form. Doing so, leads to partially aggregated systems. Using the YMCA algorithm gives much better convergence performance, which means smaller final energy and displays fibrous structures as shown in Fig 4.6 for the hexagons and in Fig 4.7 for the triangles. If we can see a slight increase in fiber width at low Γ , until $\Gamma = 0.2$, then the fixed number of particles limits the width growth. Indeed, the fibers predicted by the ansatz phase diagram are supposed to be infinite. Here, the system has to find the best aspect ratio, which appears as a trade-off between length and width.

Notice that the number of time steps in the YMCA algorithm is way smaller than in the canonical algorithm. It is because Most of the computation time is used to compute the elastic energy. In the case of the canonical Monte Carlo algorithm, many of the moves involve small aggregates and are thus very fast to compute. On the contrary, every move of the YMCA algorithm involves a single aggregate made of all particles and are much longer to compute. However, because we massively restrained the phase space, the annealing converges much faster.

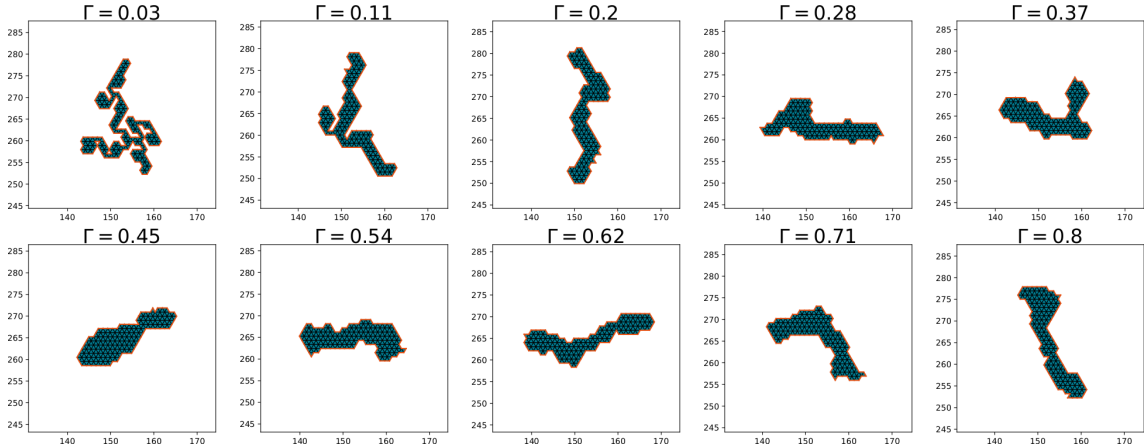


Figure 4.7: **Evolution of fiber width with Γ for triangles:** Snapshot of final states of YMCA annealing. $\nu = 0.9$, $l_0 = 2.5$. The simulations are the result of 10^5 time steps, with 250 particles. Notice that the number of time steps, as well as the number of particles, in the triangle model, is higher than in the hexagonal model. The computation time to compute the elastic energy is actually shorter in the case of triangles.

4.4.3 Increase in anisotropy with ν

We define the anisotropy as

$$\mathcal{A} = \frac{L - W}{L + W} \quad (4.7)$$

where L is the length of a fiber and W its width. The anisotropy is a number between 0 and 1. A circular aggregate will have an anisotropy of 0 and an infinite fiber of 1. For any aggregate, the tricky part is to define the length and the width and especially for curved fibers. For these reasons, we will stick to a qualitative approach of the anisotropy of an aggregate. We simulate the evolution of the anisotropy of ground state aggregates as a function of the Poisson ratio in Fig 4.8, and in Fig 4.9. To do so, we use the YMCA algorithm.

The shape Ansatz phase diagram in Fig 3.7 predicts a transition from finite disks to fibers with increasing the Poisson ratio. The tendency is well reproduced, as we observe anisotropic disk-like aggregates at small Poisson ratios and fibrous structures as ν increases. Similar to the previous canonical Monte-Carlo, the system has to optimize its shape with a fixed number of particles. In this chapter, we have used a more rigorous approach to simulate the formation of aggregates and investigate their structure. Monte Carlo simulations allow for any type of shape to emerge. Despite this extra freedom, the systems seem to form aggregates whose structures are consistent with the Ansätze previously used. On top of this,

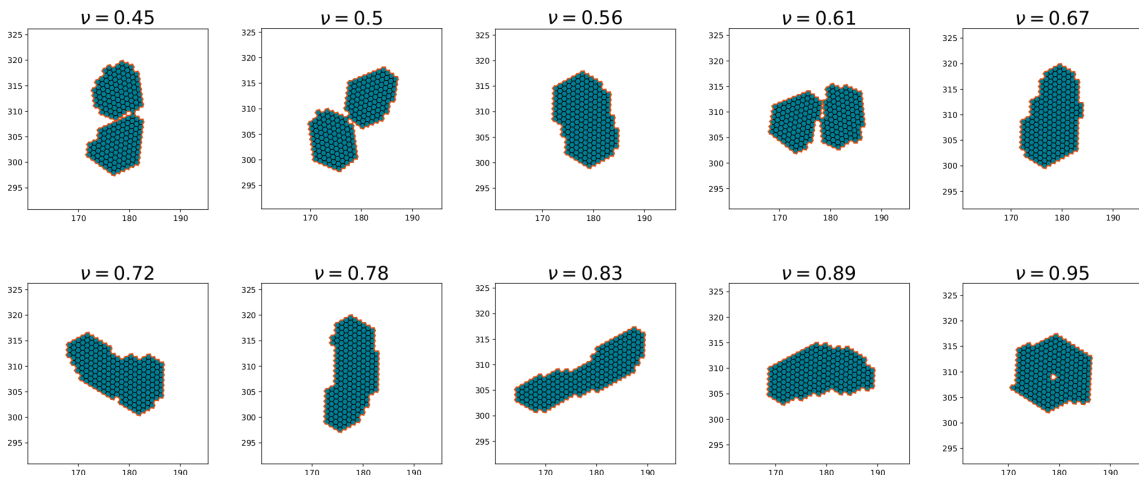


Figure 4.8: **Evolution of the anisotropy with the Poisson ratio for hexagons:** Snapshot of the final states of YMCA annealing. $\Gamma = 0.5$, $\ell_0 = 5$ and ν is given as a title. The simulation is the result of $2 \cdot 10^4$ time steps with 200 particles. Notice the structure with the highest Poisson ratio: $\nu = 0.9$, can either be interpreted as a disk with a hole, or as a curved fiber closed on itself. The latter is a way for the aggregate to suppress the tip of the fibers.

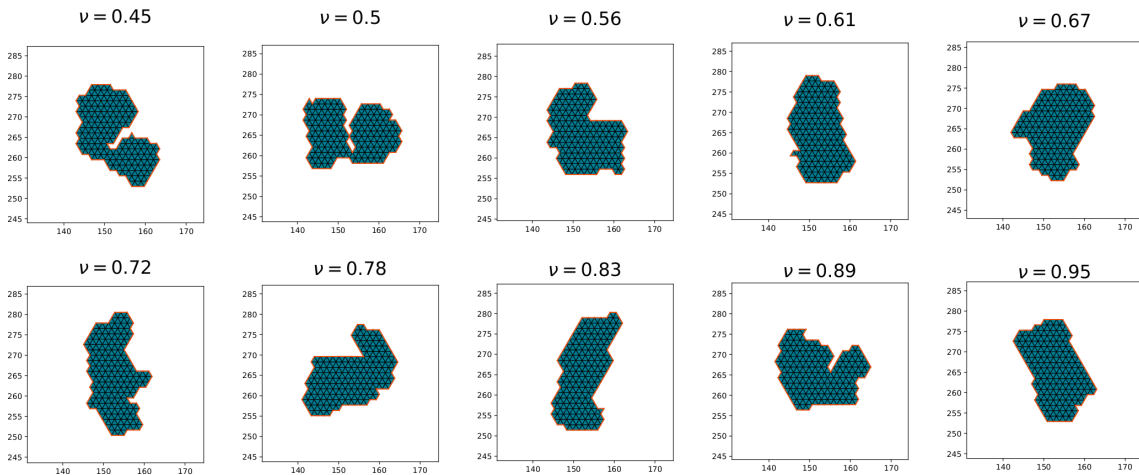


Figure 4.9: **Evolution of the anisotropy with the Poisson ratio for triangle :** Snapshot of the final states of YMCA annealing. $\Gamma = 0.5$, $\ell_0 = 2.5$ and ν is given as title. The simulation is the result of 10^5 time steps with 300 particles.

we have never been able to find a shape with a smaller energy than the predicted shape Ansatz, which further validate the Ansatz approach. In the next chapter, we design a more general model for frustrated self-assembling systems. If it is in

theory possible to perform Monte Carlo simulations on such a system, we will see that it is in practice too costly in terms of computation time. We thus use the shape Ansatz approach that is now strengthened.

Chapter 5

Mechanisms that stabilize assembly

In the previous chapters, we designed two specific models of geometrically frustrated self-assembling particles, now referred to as spring models. For each of these models, emergent properties appear when particles interact together, such as limited-size assembly or formation of fibrous structures. We have derived a continuum model that helped us to understand the origin of these phenomena. Moreover, the continuum model provides a link between the bulk properties of the particles and the preferred assembling structure. This is why, despite relying on a different lattice, both particle models –triangular and hexagonal– behave essentially the same. We now try to go one step further and check if the results brought by the continuum model can apply to a more general model of particles.

The key feature of our previous model of particle is the possibility to decompose a large aggregate into two spring networks with different lattice sizes, yet coupled by coupling springs. In section 5.1, we introduce a way to generate geometrically frustrated particles that cannot be decomposed into two spring networks. There are many ways to generate such particles. To do so in the most unbiased way we will generate particles with random mechanical properties. At this point we will be able to generate thousands of different models of particles, all different. To study their assembly Monte Carlo simulation will be way too computationally expensive. Instead, we are going to use the approach previously validated that consist in comparing the energy of Ansatz of shapes. We will investigate the two main results previously derived. First, in section 5.2 we study the correlation of a boundary layer of stress relaxation with limited-size self-assembly. Then in section 5.3, we will investigate the mechanisms that stabilize the formation of fibers over disks by looking at the correlation between fibrous assembly and high Poisson ratio.

5.1 A more general model: the random hexagons

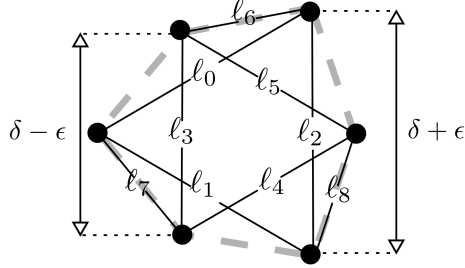


Figure 5.1: **Degrees of freedom of a random particle** : An irregular hexagon is represented as a dashed line. We use the 9 l_i 's distances to determine the energy of a particle. The rest length of all the l_i 's is set so that the rest configuration is similar to the spring model: $l_0, l_1, l_2 = \delta + \epsilon$, $l_3, l_4, l_5 = \delta - \epsilon$, $l_6, l_7, l_8 = \sqrt{1/3 + \epsilon^2}$. ϵ quantifies how frustrated the particle are.

In this section, we design a model for hexagonal random particles. We build a model for three-fold symmetric, yet geometrically frustrated, self-assembling particles. Similar to the previous spring model the nodes of the particles are arranged on a hexagonal lattice and are thus hexagons themselves with the same rest state than the hexagonal spring model. We model the elasticity of the particles as a quadratic expansion of a potential around the rest state. We first have to choose the degrees of freedom on which the potentials are going to act. An hexagon has 6 nodes which means 12 degrees of freedom. To be consistent with the elasticity, the energy has to be invariant over translation -along X and Y- and along a continuous rotation of the particle. This gives a total of 9 independent degrees of freedom for that can be constrained by the expansion of the energy. We require isolated particles to be rigid which means having at least as many constraints than degrees of freedom and is called isostaticity. For a particle to be an isostatic we have to constrain all of its 9 degrees of freedom. We ensure these invariances by construction by choosing the random potential to act on the distance between nodes rather than the node's position. We use the 9 distances between nodes, represented in Fig 5.1 as a set of degrees of freedom to write the energy. We denote ρ the vector that contains all the $\{l_i\}$ s, and ρ_0 the value of the l_i s in the rest configuration. The Taylor expansion of the energy to 2nd order of a particle reads :

$$F(\rho) = (\rho - \rho_0)A + (\rho - \rho_0)M_c(\rho - \rho_0)^T \quad (5.1)$$

where M_c is a random matrix referred to as the coupling matrix in the following. M_c has to be positive definite for the free energy to be convex which ensure that ρ_0 is a steady minimum of the free energy. Moreover, we require M_c to be symmetric.

Finally, we impose M_c to be three-fold symmetric, which guarantee the isotropicity of the mechanical properties of a large aggregate. ρ_0 is the rest state of the single particle, which means no internal force is being applied to an individual particle in the configuration ρ_0 by definition of the rest state:

$$\frac{\partial E}{\partial \rho} \Big|_{\rho_0} = 0 \quad (5.2)$$

which imposes $A = 0$. To draw a random coupling matrix, we draw random entries from a normal distribution of mean 0 and variance 1. We then apply the two following operations to make sure the matrix has the correct symmetry:

$$M_1 = \frac{1}{3} (M_0 + \Omega_3 M_0 \Omega_3^{-1} + \Omega_3^2 M_0 (\Omega_3^{-1})^2) \quad (5.3)$$

$$M_c = M_1 M_1^T \quad (5.4)$$

$$(5.5)$$

where M_0 is the initial random Gaussian matrix and Ω_3 is a permutation matrix :

$$\Omega_3 = \begin{bmatrix} 0. & 0. & 0. & 0. & 1. & 0. & 0. & 0. & 0. \\ 0. & 0. & 0. & 0. & 0. & 1. & 0. & 0. & 0. \\ 1. & 0. & 0. & 0. & 0. & 0. & 0. & 0. & 0. \\ 0. & 1. & 0. & 0. & 0. & 0. & 0. & 0. & 0. \\ 0. & 0. & 1. & 0. & 0. & 0. & 0. & 0. & 0. \\ 0. & 0. & 0. & 1. & 0. & 0. & 0. & 0. & 0. \\ 0. & 0. & 0. & 0. & 0. & 0. & 0. & 0. & 1. \\ 0. & 0. & 0. & 0. & 0. & 0. & 1. & 0. & 0. \\ 0. & 0. & 0. & 0. & 0. & 0. & 0. & 1. & 0. \end{bmatrix} \quad (5.6)$$

and Ω_3^{-1} its inverse. The operation: $\Omega_3 M_0 \Omega_3^{-1}$ to M_0 applies the following permutation over rows and column to M_0 :

- $\ell_0 \rightarrow \ell_3$ • $\ell_3 \rightarrow \ell_1$ • $\ell_6 \rightarrow \ell_7$
- $\ell_1 \rightarrow \ell_4$ • $\ell_4 \rightarrow \ell_2$ • $\ell_7 \rightarrow \ell_8$
- $\ell_2 \rightarrow \ell_5$ • $\ell_5 \rightarrow \ell_0$ • $\ell_8 \rightarrow \ell_6$

The operation $\Omega_3^2 M_0 (\Omega_3^{-1})^2$ applies the same permutation twice. For a matrix to be three-fold symmetric, it has to be invariant over such operation. If we apply these permutations to M_1 we get :

$$\Omega_3 M_1 \Omega_3^{-1} = \frac{1}{3} (\Omega_3 M_0 \Omega_3^{-1} + \Omega_3^2 M_0 (\Omega_3^{-1})^2 + \Omega_3^3 M_0 (\Omega_3^{-1})^3) \quad (5.7)$$

Using the property: $\Omega_3^3 = I$, gives:

$$\Omega_3 M_1 \Omega_3^{-1} = M_1 \quad (5.8)$$

therefore, M_1 is three-fold symmetric. Finally, Eq (5.4) ensures the final coupling matrix to be positive definite.

We define ρ_0 so that the rest configuration is the same as in the spring model, which guarantees these particles to be geometrically incompatible. Similar to the spring model, the aggregation process is driven by a constant energy cost per free edge and the aggregation rule applies as if particles was not allowed to rotate.

5.2 On the boundary layer of stress relaxation

We derive the characteristic length in Eq (2.26) from the analytical theory of section 2.3 This length sets the typical size of the self-limited aggregate. We have also seen in the 1D model in section 2.2, that this characteristic length is associated with a decrease of the stress in an aggregate close to its boundary. Here we explain how we generalized the meaning of the characteristic length to the random particles in section 5.2.1. We then show the relevance of this new definition by correlating the newly defined characteristic length with the equilibrium size of ansatz of shape in section 5.2.2.

5.2.1 Measuring the boundary layer

Previously, in section 2.2 we derived the local elastic energy of a particle in an aggregate as a function of its distance from the border of the aggregate, as written in Eq (2.14). As mentioned, this phenomenon is not specific to this simple 1D squared model. Fig 5.2 shows how the characteristic length ℓ_0 derived from the spring model is related to the local elastic energy, and thus the stress. We are going to use this phenomenon as a basis to define the characteristic length ℓ_0 of the random particle model. To do so, we consider the situation described in section 2.2 in the case of a very thick fiber i.e. $\mathcal{W} \rightarrow \infty$. We neglect the contribution of the coupling springs to the energy and expand Eq (2.14) close to the border of the

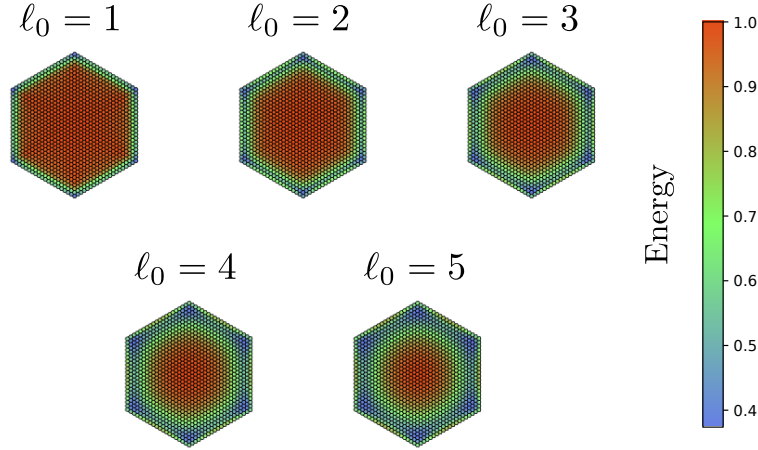


Figure 5.2: **Link between the characteristic length and stress relaxation layer in the spring model:** Each particle is color-coded depending on its elastic energy by summing over the energy of all of their individual springs. We see that the energy is smaller close to the boundary and increases until it reaches the bulk elastic energy in the center of the aggregate. The distance over which this relaxation occurs increases as the characteristic length ℓ_0 increases. Every energy is in bulk energy units.

aggregate: $\xi \rightarrow \mathcal{W}/2 - x$, where x is the distance from the border :

$$\begin{aligned}
 e_{el}(x) &= E\delta\eta^2 \left(1 - \frac{\cosh\left(\frac{\mathcal{W}}{2\ell_0} - \frac{x}{\ell_0}\right)}{\cosh\left(\frac{\mathcal{W}}{2\ell_0}\right)} \right) \\
 &= E\delta\eta^2 \left(1 - \frac{\cosh\left(\frac{\mathcal{W}}{2\ell_0}\right) \cosh\left(\frac{x}{\ell_0}\right) - \sinh\left(\frac{\mathcal{W}}{2\ell_0}\right) \sinh\left(\frac{x}{\ell_0}\right)}{\cosh\left(\frac{\mathcal{W}}{2\ell_0}\right)} \right) \quad (5.9) \\
 &\xrightarrow{\mathcal{W} \rightarrow \infty} E\delta\eta^2 (1 - e^{-x/\ell_0})
 \end{aligned}$$

where $E\delta\eta^2 = f_B$ is the bulk energy. The analytical theory predicts that the elastic energy should relax exponentially as we approach the border of the aggregate. More generally, we can approximate the elastic energy of an individual particle in an aggregate as a function of its distance from the border by:

$$f(\xi) = f_B - (f_B - f_{\text{edge}})e^{-\xi/\ell_0} \quad (5.10)$$

where ℓ_0 is the generalized characteristic length, f_B the bulk free energy of an individual particle, and f_{edge} the energy of a particle on the edge. ξ is the topological distance from the border, it is a discrete variable. Distances are computed

by calculating the number of nearest neighbors that separate two particles. The distance of a particle from the border is computed by taking the minimum of the distances between the given particle and the particles at the border. We show the validity of the approximation Eq (5.10) on a random particle in Fig 5.3. We can then compute ℓ_0 using :

$$\ell_0 = \sum_{\xi=0}^{\xi_{\max}} \frac{f_B - f(\xi)}{f_B - f_{\text{edge}}} \quad (5.11)$$

ξ_{\max} is the value of ξ at the center of the aggregate. The equation Eq (5.11) remains approximately valid as long as $\ell_0 < \xi_{\max}$.

Fig 5.4 shows the correlation between this definition and the analytic ℓ_0 on the spring model. In the context of random particles, we can simulate such an aggregate to measure f_B , f_{edge} , and $f(\xi)$, which gives us a measure of the characteristic length.

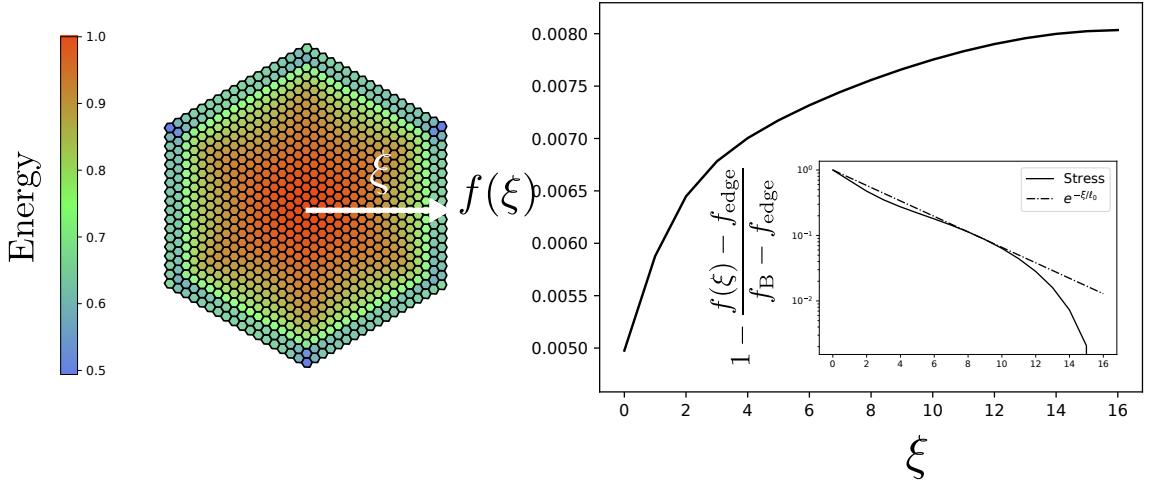


Figure 5.3: **Elastic energy of random particles in an aggregate:** The graph is obtained by averaging the energy of all the particles that are at the same distance from the edge. Here we used a randomly generated particle. Every randomly generated particle display a similar exponential decrease of the energy from center to border. Inset, semi-logarithmic plot of the energy function. The Y axis has been adapted to emphasize the exponential aspect of the stress decay at the boundaries. In this drawing, we measure $\ell_0 \sim 5$.

5.2.2 Correlation with the equilibrium size

In this section, we look at the size of the equilibrium aggregates. Equilibrium aggregates are determined using a shape Ansatz, either disk or fiber. Computing

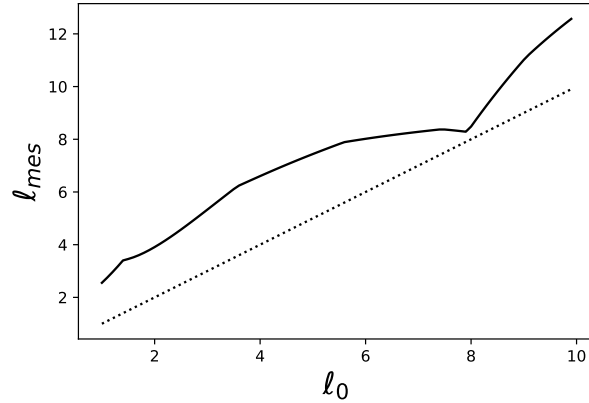


Figure 5.4: **Consistency between analytic and measured ℓ_0 :** We are using the spring model to compare the analytic definition of ℓ_0 given Eq (2.26) and the measured one. ℓ_{mes} is the characteristic length obtained by measurement of the relaxation layer of the stress using Eq (5.11). The correlation is not perfect, but sufficient to be able to select random particles that will create limited size self-assembly.

the energy of an increasing size disk, for instance, reveals local minima in the energy. The size corresponding to this minimum of energy is called the size of the equilibrium aggregate. We have already observed such aggregates in the spring model, and similarly, we expect the analytical continuum limit theory to apply when the characteristic length becomes large: $\ell_0 \rightarrow \infty$. Previously, this was achieved by reducing the stiffness κ of the coupling springs. Here, instead, we are looking for different modes of deformation that could be responsible for the emergence of a decrease of the energy at the border. We thus generate 4000 random matrices and measure their characteristic length with Eq (5.11). Fig 5.5 shows the probability distribution of drawing a random matrix that gives rise to a certain ℓ_0 . Most of them have a fairly low ℓ_0 , around 2. Indeed, looking at Eq (2.26), the characteristic length is the ratio of the shear modulus with the stiffness of the coupling spring. For this length to be large, a particle must exhibit two modes of deformation with very different stiffnesses. In the context of random entries drawn from a Gaussian distribution, drawing several entries with very different stiffness is rather unlikely. Based on this measurement, we can look at the influence of ℓ_0 on the size of the lowest energy aggregate. To do so, we first define a scale of surface tension for each random particle. Eq (2.27) gives the rescaling between γ the surface tension and Γ in the continuum model. We want to design an equivalent rescaling of the surface tension for the random particles. Here, as in the spring model, we use a constant cost per free edge, denoted J as a surface tension. We

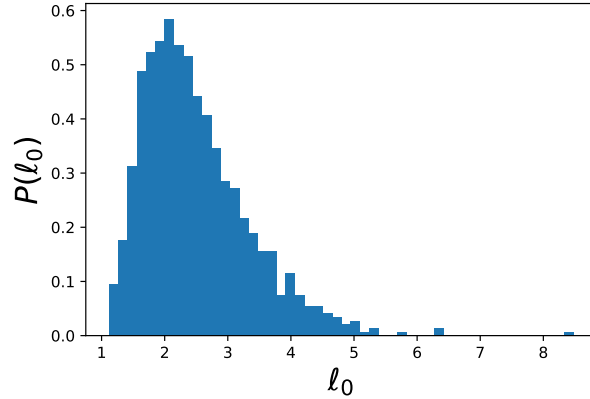


Figure 5.5: **Probability of drawing a matrix with a given ℓ_0 .**

can associate to any random particle a value J_{\max} which is the value of J above which the equilibrium aggregate is always a bulk. We then define the bulk free energy F_B for the random particles. We know from section 2.1 that the only way for these particles to tightly pack into a macroscopic aggregate is to become a regular hexagon. Given a random particle, we deform it into a regular hexagon and minimize the energy of the particle as a function of the regular hexagon's edge size. Which corresponds to the best compatible shape of a given random particle. Finally, we define Γ as :

$$\Gamma = \frac{J}{F_B} \quad (5.12)$$

And Γ_{\max} as :

$$\Gamma_{\max} = \frac{J_{\max}}{F_B} \quad (5.13)$$

We now look at the evolution of the size of the equilibrium aggregate for random particles as a function of Γ/Γ_{\max} . Finite-size equilibrium aggregates only exist when the characteristic length ℓ_0 is not too small. Small $\ell_0 < \delta$ does not give equilibrium aggregates above size 1, which is not very meaningful. Among the 4000 random matrices drawn, we selected the 500 random particles with the largest ℓ_0 , which gives $\ell_0 > 2.34$. We expect the random particle model to display a similar behavior to the continuum limit one when the size of the equilibrium aggregate is large compared to the particle size. We thus plot Fig 5.6 respectively the evolution of the number of particles in the equilibrium disk rescaled with the characteristic length, and similarly the rescaled width in the equilibrium fiber as a function of $1 - \Gamma/\Gamma_{\max}$ for random particles. Notice that the rescaling of the size of the particles with the characteristic length is crucial for the consistency between the random particle model and the analytical model. This consistency suggests that

the phenomena observed are more general than the spring model on which the computation has been made.

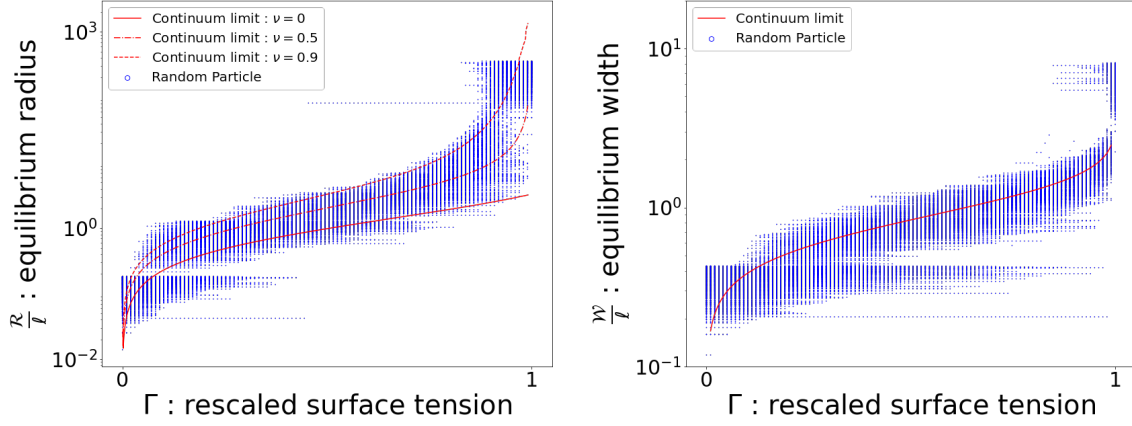


Figure 5.6: **Evolution of the equilibrium size / width as Γ/Γ_{\max} goes to 1:** Left: we plot the number of particles in an equilibrium aggregate, rescaled by the measured characteristic length. If R is the radius of the ground state disks, the rescaled radius is $\rho = R/\ell_0$ with the number of particles $N_p \propto \rho^2 \propto R^2/\ell_0^2$. On top of the random particles dot, we added the analytic prediction for different ν . Right: similarly, we plot the ground state width of fibers, rescaled by the characteristic length. The analytic continuum limit is also given, notice that the Poisson ratio ν does not change the equilibrium width.

5.3 Mechanisms that stabilize the fibers

We are now able to generate random particles with fairly large characteristic lengths. From the two phase diagrams computed in section 2.3 for the continuum model and in section 3.4 for the spring model, we see that larger ν favors fiber formation. We now investigate this phenomenon in the context of random particles. We first design a procedure to measure the Poisson ratio of a random particle in its bulk configuration. In a continuum material, the elastic free energy can be written [27]:

$$f = \frac{1}{2}(2\mu u_{ij}^2 + \lambda u_{kk}^2) \quad (5.14)$$

where λ and μ are the two Lamé coefficients [27]. We consider a random particle in its bulk configuration: a regular hexagon. We apply two types of deformations to the particle in its bulk configuration by moving its nodes according to a strain tensor. We then measure the change in energy to obtain an estimate of λ , and μ .

First, a volumetric deformation, which 2D strain tensor can be written:

$$\begin{pmatrix} u_{xx} & 0 \\ 0 & u_{xx} \end{pmatrix} \quad (5.15)$$

which gives for the free energy :

$$f = 2(\lambda + \mu)u_{xx}^2 \quad (5.16)$$

Second, we apply a pure shear deformation :

$$\begin{pmatrix} u_{xx} & 0 \\ 0 & -u_{xx} \end{pmatrix} \quad (5.17)$$

Which gives for the free energy :

$$f = 2\mu u_{xx}^2 \quad (5.18)$$

Measuring the energy change after each deformation, and plotting the energy as a function of u_{xx}^2 gives a line of slope respectively $2(\lambda + \mu)$ for the volumetric deformation, and 2μ for the pure shear. Finally, the Poisson ratio can always be written as a function of the previously measured Lamé coefficients:

$$\nu = \frac{\lambda}{\lambda + 2\mu} \quad (5.19)$$

Fig 5.7 shows the probability of generating a particle with a given Poisson ratio. We can now generate random matrices as explained in section 5.1, select the matrices that yield high ℓ_0 as explained in section 5.2 and sort them according to their Poisson ratio in their bulk configuration. Finally, we study what is the aggregate shape formed by such particles as a function of the Poisson ratio. The results over 100 particles are represented in Fig 5.8. On top of this phase diagram, we performed more accurate statistics over four thousand particles. Fig 5.9 shows the fraction of a line of the phase diagram, that is a disk -fraction of red- as a function of ν . The first phenomenon that is qualitatively displayed in Fig 5.8 and then confirmed in Fig 5.9 is that fibers form more often than disks. Secondly, the correlation between fiber stability and Poisson ratio is not reproduced in this model. Our first model focuses on a specific mode of deformation that displays a decrease of the elastic energy at the border of an aggregate. It seems that this mode is not the only deformation that is responsible for the stability of finite-size aggregates.

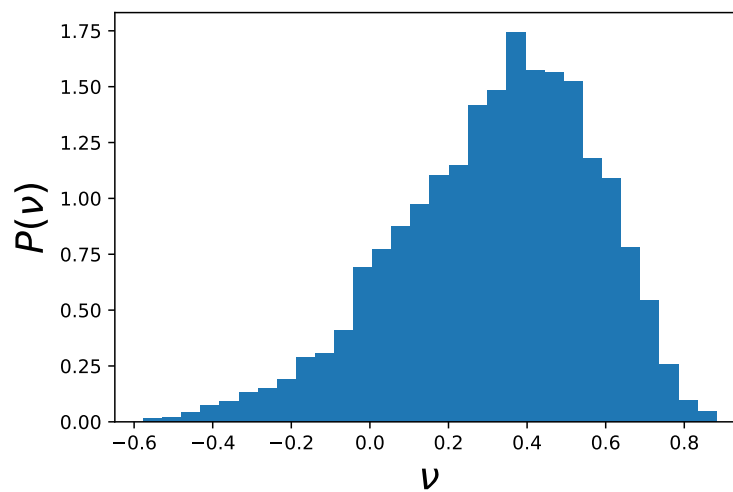


Figure 5.7: **Probability distribution of Poisson ratio** : The probability is centered around $\nu = 1/3$, which is the value of the Poisson ratio obtained if the coupling matrix is the identity matrix. Coupling matrix being the identity matrix means that the energy is a set of 9 linear springs corresponding to the distances represented in Fig 5.1

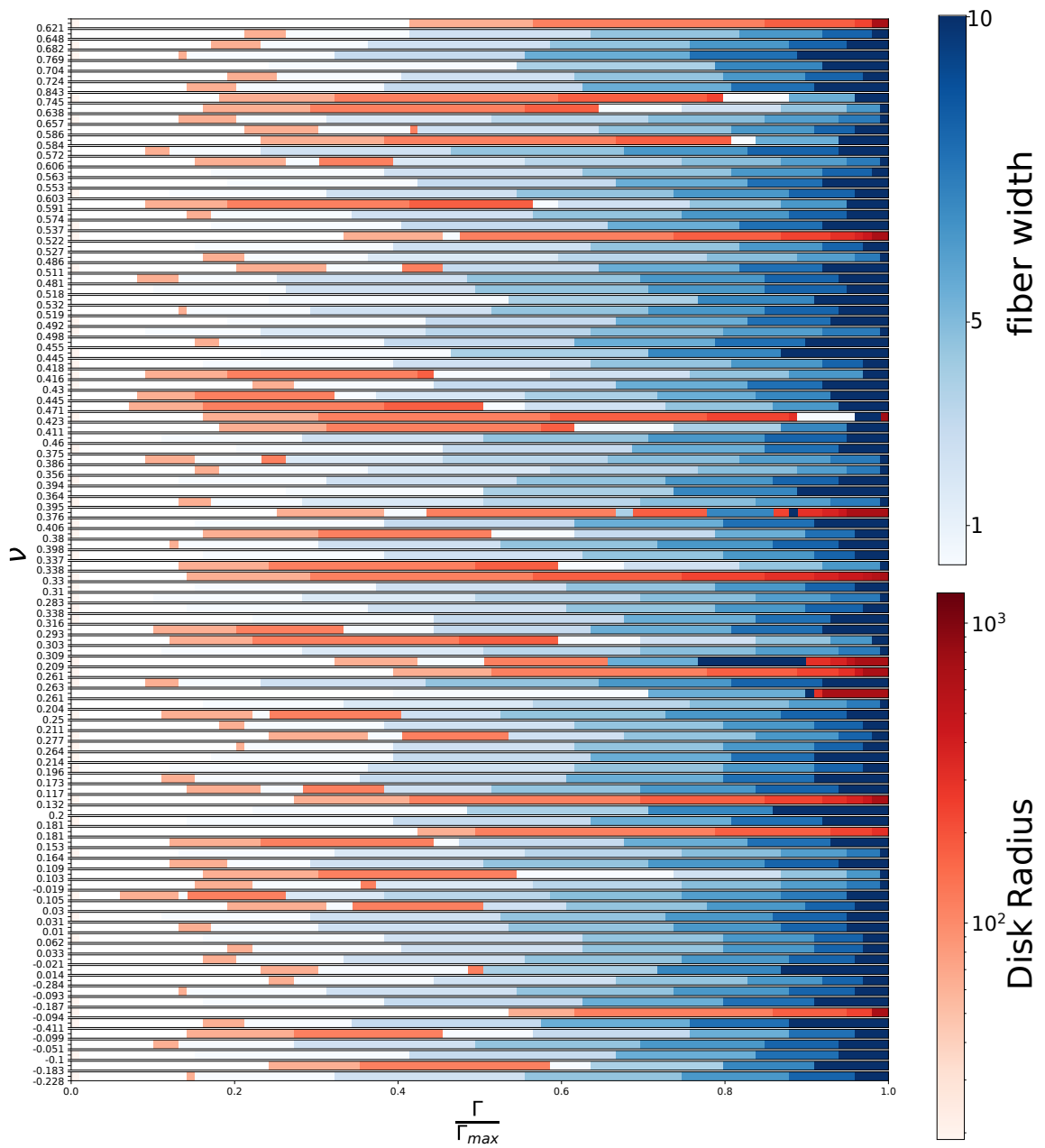


Figure 5.8: **Phase diagram of random particles:** Each line represents a random particle. For each value of $\frac{\Gamma}{\Gamma_{max}}$, the shape and width of the most stable aggregate are represented by a color patch.

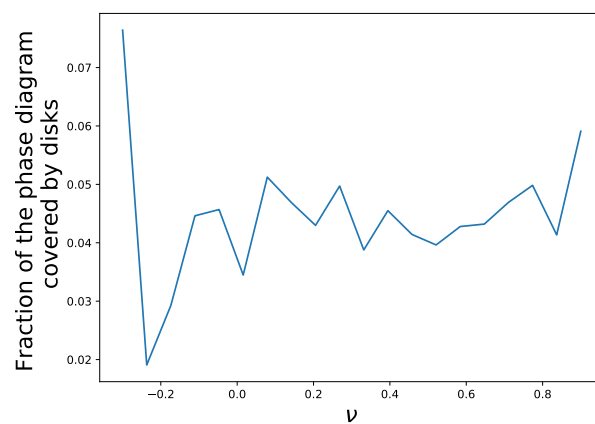


Figure 5.9: **Fraction of ground state disks** : We performed a similar analysis to the one in Fig 5.8 with 4000 random particles. We then sum the fraction of red regions to obtain a fraction of disk's stability. The no-tendency that is qualitatively displayed in Fig 5.8 is confirmed here with better statistics.

Conclusion

In this first part of the thesis, we studied the effect of geometrical frustration on self-assembling systems through the lens of two main phenomena. Firstly, the emergence of a characteristic lengthscale that sets the size of equilibrium aggregates. Secondly, an overall tendency to form fibrous structures over isotropic ones. To do so, we designed a specific model of ill-fitting particles, supposed to represent a coarse-grained version of assembling particles such as proteins. We derived a continuum version of this model that helped us to understand the origins of the two main questions we addressed initially. Based on this, we designed a third, more general, model where the particles are still simple geometrical shapes, but their mechanical properties are drawn randomly. The goal of this random particle model was to verify whether the results brought by the continuum limit could be more general than the specific particle model it was designed for. It turns out that we can observe the emergence of a characteristic lengthscale that we associated with a decrease of the elastic energy close to the border of an aggregate. However, we have not been able to identify the modes of deformation responsible for this boundary layer of stress relaxation. Quite surprisingly, the random particle model reveals that the fibers are stable in a broad range of surface tension. This is not exactly in accordance with the conclusion of the continuum model which predicts fibrous aggregate stability only at a large Poisson ratio. It seems that fibers provide more freedom to modes of deformation that would relax stress in the structure, such as bending, or maybe twisting in 3d. This study only focuses on comparing the energy of aggregates and does not tackle any questions related to thermal fluctuation, which should enrich the phenomenology of this type of model.

Part II

Control of non-exponential stress relaxation of hydrogels through tuning of crosslinker valency.

Chapter 6

The wide variety of hydrogels' mechanical behavior

In this chapter, we introduce the class of hydrogels we will study. We start by introducing hydrogels, their applications, and the recent advances in the field in section 6.1. We then present an experimental system that has been developed by our collaborators at MIT in section 6.2. They are able to synthesize a broad variety of hydrogels whose mechanical response to an external strain is extremely slow, around a day. However, the exact microscopic relaxation mechanism that leads to such a slow dissipation of the stress is unclear. Finally, in section 6.3, we will review some existing models for hydrogel mechanical relaxation. Starting with the simplest model will enable us to identify the main challenges that we will be facing.

6.1 The hydrogel family

A hydrogel is a network of hydrophilic polymers that swell once in contact with water. They are mainly made of water ($\sim 90\%$), making them cheap and easy to synthesize. Hydrogels are often a viscoelastic material. Their elasticity comes from the rubber elasticity of the polymer matrix, while the viscous behavior originates from the friction of water, reptation of the polymer chains, or dynamical crosslinks [52, 53]. Soft hydrogels are ubiquitous in biology and dictate the mechanics of cells and tissues [54], due to their biocompatibility, synthetic hydrogels are prime candidates to serve as robust soft tissue implants, although a fine control of their mechanical properties is crucial for their success in this role [55, 56]. In addition to standard approaches based on polymer rigidity and concentration [57, 58], a new design paradigm consisting of using nanocomposite hydrogels has recently emerged [48, 59]. These hydrogels contain the usual polymer matrix in which large

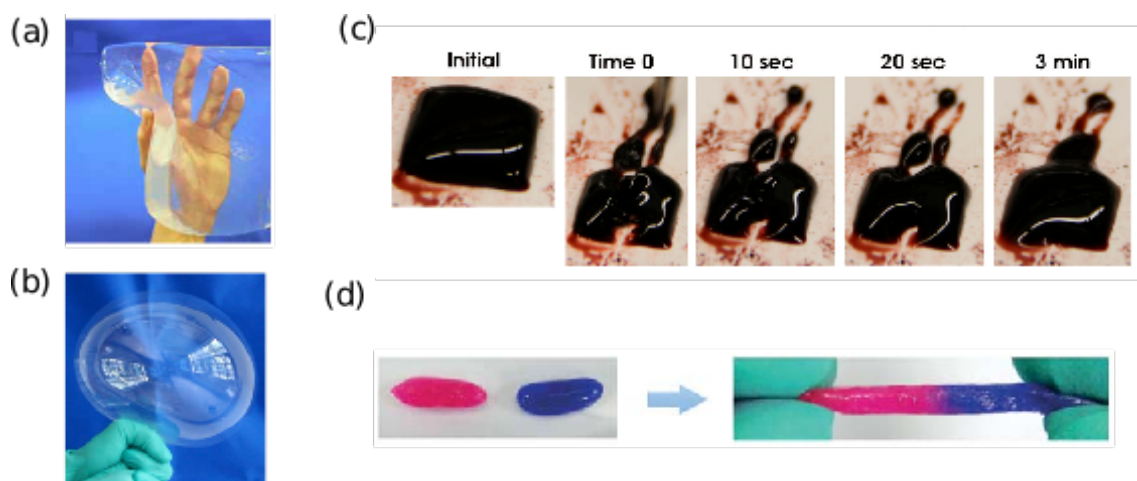


Figure 6.1: **Properties of nanocomposite hydrogels**(a) Illustration of the rigidity of a thick sheet of nanocomposite hydrogel from [48]. (b) Air inflation experiment into a nanocomposite hydrogel, showing the deformability of hydrogel from [49]. (c) Self healing of metal ion-ligand composite hydrogel, after an initial shear failure, the sample is able to recover its initial shape from [50]. (d) Self adhesion of two nanocomposite hydrogels from [51].

crosslinkers are added to create tougher materials than the usual hydrogels, with remarkable abilities such as self-healing [51, 60, 61] as shown in Fig 6.1. In particular, a promising platform consists in hydrogels of polymers carrying crosslinks that form reversible metal-coordinate bonds with metal ions or nanoparticles [50, 62]. These ions or particles crosslink the gel, and viscoelastic stress relaxation and flow proceed as they unbind, relax, and rebind to the polymer. This relaxation mechanism enables tight control over the gels' dynamic properties by controlling the rate of unbinding, and enables new design strategies. In particular, large crosslinkers can create bonds composed of multiple polymer strands. Multivalent binding appears today as a tractable method to enhance selective binding [63], or to tightly control self-assembling structures [64, 65]. In the following, we will study the influence of crosslinker coordination on the mechanical properties of the gel.

6.2 Experimental setup

To study the influence of the valency of the ligands on the mechanical response of transient hydrogels, a group of experimental collaborators: Jake Song, Niels Holten-Andersen, and Gareth Mckinley synthesized three different metal coordinate hydrogels. Each of these gels are made using star polymers -4arms polyethy-

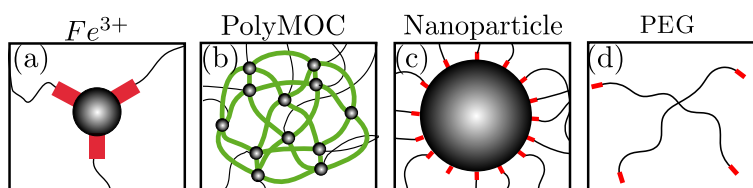


Figure 6.2: **Constitutive element of the gels** : (a) Fe^{3+} ligands has a fixed valency of three. (b) metal organic cages (MOC) is made of Fe^{3+} ions and polymers that bind at a very specific angle. This creates a cage. The coordination is estimated to 14 [66]. (c) nanoparticles of Fe_3O_4 , it is a macroscopic ligand, many polymers can bind to it. We computed the coordination by assuming that the binding of new polymers on a nanoparticle stops whenever the steric interactions are stronger than the binding energy. This gives us an estimation of 80 polymers per nanoparticle. (d) 4arms polyethylen glycol functionalized with anitrocatechol group at their ends to create a binding with the crosslinkers.

lene glycol: PEG- to the ends of which a nitrocatechol group has been added which can bind to the metal crosslinkers Fig 6.2 (d). Each system uses a different crosslinker with different valencies as represented in Fig 6.2 (a,b,c) Fe^{3+} .

The dynamic mechanical properties of the gels are tested by applying a step strain to the sample and measuring how the stress relaxes throughout time. The experiment is carried on using an Anton Paar rheometer with parallel plate geometry (10 mm diameter flat probe for NP gels and polyMOC gels, and 25 mm diameter cone probe for Fe^{3+} gels). The same experiment is performed at five different temperatures for each system. This experiment results in the measurement of $G(t)=\sigma(t)/\gamma_0$ called the relaxation modulus, where $\sigma(t)$ denotes the stress in the sample as a function of the time and γ_0 , the initial strain. The resulting relaxation moduli are given in Fig 6.3. The strain remains small to make sure that we only probe the linear response of the gel and avoid effects such as strain stiffening of the polymer's stretching rigidity, or avalanches of unbinding [67].

The Fe^{3+} system displays a fast, almost exponential relaxation, as we can see in Fig 6.3 with a characteristic time $\tau \approx 1s$, which is of the same order of magnitude as the microscopic event of unbinding of a polymer from a ligand. In the poly-MOCs and nanoparticle systems instead, we observe that the average relaxation time is higher by orders of magnitude, on the one hand, and that the relaxation is less and less exponential on the other hand. To elucidate the viscoelastic relaxation of these soft materials with high-valency crosslinks and enable the rational design of metal-coordinated hydrogels with long relaxation times, we develop in the following chapters a physical model of this relaxation.

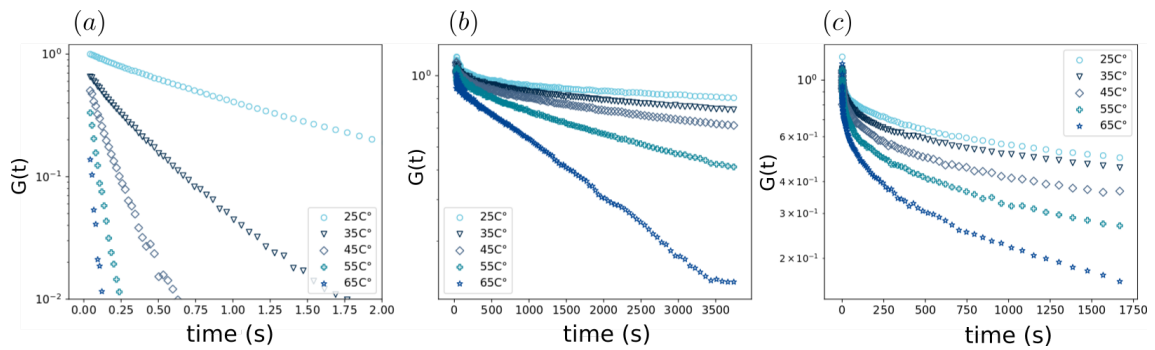


Figure 6.3: **Stress relaxation experimental curves** : (a) stress relaxation of Fe^{3+} (b) poly-MOC system (c) nanoparticles system. The lin-log scale emphasizes how exponential is the relaxation -the straighter the curve is, the closer to an exponential it is.

6.3 Model for viscoelastic relaxation of transient hydrogels

To understand the specificity of the hydrogels used by our experimentalist collaborators, we first introduce viscoelasticity in its simplest version in section 6.3.1: the Maxwell spring-damp model. We first derive the mechanical response of the spring-damp to a step strain and second, we present a theory for reversibly crosslinked networks in section 6.3.2. We show that under some assumptions, such a network can display the same mechanical response as a spring-damp system [68]. Nevertheless, the reality is usually more complex, especially for composite materials. We thus introduce in section 6.3.3, the stretched exponential law and present its usual interpretation.

6.3.1 Maxwellian relaxation

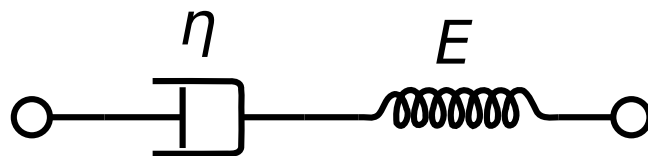


Figure 6.4: Maxwell model.

Viscoelastic materials exhibit both elastic (solid-like) and viscous (liquid-like) behavior. The Maxwell model for viscoelastic materials is a straightforward translation of this by associating a solid-like model: a spring of stiffness k and a liquid-

like model: a damper of viscosity η in series as shown in Fig 6.4. We can compute the mechanical response of such a system by writing first that the stress in the damper and in the spring are equal :

$$\sigma(t) = \eta \frac{d\epsilon_1}{dt} = E\epsilon_2 \quad (6.1)$$

with ϵ_1 the relative deformation of the damper, and ϵ_2 the relative deformation of the spring. We then write the total deformation of the system as the sum of both deformations, and differentiate it with respect to time to obtain :

$$\frac{d\epsilon}{dt} = \frac{d\epsilon_1}{dt} + \frac{d\epsilon_2}{dt} \quad (6.2)$$

And finally by using Eq (6.1) we obtain :

$$\frac{d\epsilon}{dt} = \frac{1}{E} \frac{d\sigma}{dt} + \frac{\sigma}{\eta} \quad (6.3)$$

This equation defines a single relaxation time $\tau = \eta/E$. In the context of a step strain, we consider a sample stress-free for $t < 0$ and apply a constant deformation to the sample: ϵ_0 at time $t = 0$. The stress relaxes throughout time. Using this initial condition, we can compute the solution of the differential equation Eq (6.3) called the relaxation modulus: $G(t) = \sigma(t)/\sigma_0 = e^{-t/\tau}$, where $\sigma_0 = E\epsilon_0$ is the stress at the beginning of the relaxation. The relaxation is thus a single exponential. It is a common behavior for hydrogels that occurs when the system relaxes according to a single microscopic time.

6.3.2 Ideal network theory

To understand why the spring-damp model is interesting, we now consider an reversibly crosslinked polymer network and derive its response to a step strain. The polymer network is made of small chains, so that we can neglect the entanglement of the polymer chains and consider the Rouse relaxation time to be much shorter than the lifetime of the crosslinks. We consider a small shearing step strain applied to a hydrogel made of such a network to probe its linear response see Fig 6.5. Let $N(t)$ be the number of polymer strands that carry stress at time t and $\sigma(t)$ the stress at time t in the gel. We assume the deformation to be affine in the ideal network, so that initially, the part of the stress carried by each individual bond is $\sigma(0)/N(0)$. Whenever a bond detaches, the stress that the polymer chain carries is assumed to immediately relax. Therefore, we write:

$$\sigma(t) = \frac{\sigma(0)}{N(0)} N(t) \quad (6.4)$$

The crosslinkers have a characteristic lifetime τ , because linear response theory ignores the effect of strain on the unbinding event, the unbinding process is a Poisson process. We introduce the survival probability of a crosslink $S(t)$, which is the probability for a crosslinker to still be bound, we have: $N(t) = N(0)S(t)$. Using Eq (6.4), we get :

$$\sigma(t)/\sigma(0) = S(t) \quad (6.5)$$

The survival probability of a Poisson process of rate $\nu = 1/\tau$ is exponential, which finally gives us :

$$\sigma(t) = S(t) = e^{-t/\tau} \quad (6.6)$$

which gives a relaxation modulus defined by a single relaxation time similar to the Maxwell spring-damp model.

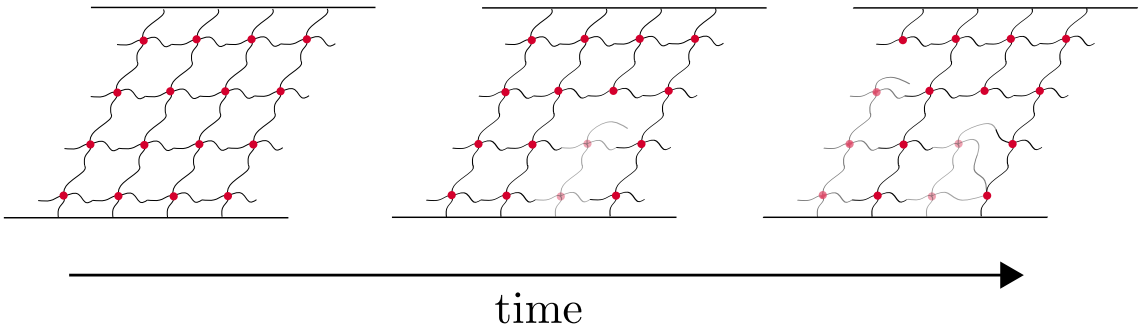


Figure 6.5: **Relaxation in a transient ideal network** : We represent a network of crosslinkers represented as red dots that bind polymer chains together, represented in black. Polymer chains initially contribute to the mechanical response of the network. The network is sheared at the beginning of the experiment, and the relaxation occurs as the polymers unbind from the crosslinkers -shaded regions correspond to mechanically inactive chains-. Subsequent re-binding happens without re-stretching the strand, and thus does not re-introduce any stress.

6.3.3 Stretched exponential relaxation

The model previously introduced captures the mechanical response of simple hydrogels [69, 70, 71], but is not necessarily working well for composite hydrogels . The introduction of larger crosslinkers, in which dozens of polymers can simultaneously bind, slows down the relaxation, but also comes at the cost of the simple Maxwellian relaxation. Typically, this results in a broadening of the distribution of time scales, and the stress response $\sigma(t)$ to a step strain is commonly approximated by a stretched exponential :

$$\sigma(t) \propto \exp [-(t/\tau)^\alpha] \quad (6.7)$$

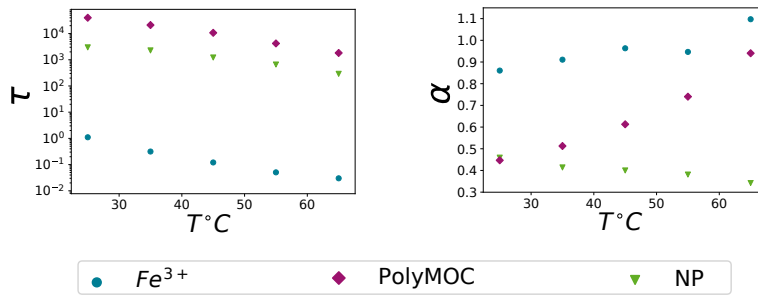


Figure 6.6: **Fitting parameters obtained for stretched exponential**

Using this formula with the time constant τ and a stretching exponent $\alpha \in]0, 1]$ treated as fitting parameters is a convenient way that rheologists use to compare complex non-exponential relaxation. A stretched exponential function is usually associated with the existence of multiple relaxational time scales [72] :

$$G(t) = \exp(-(t/\tau)^\alpha) = \int_0^\infty \rho(\tau, \alpha) e^{-t/\tau} d\tau \quad (6.8)$$

In this description, each relaxation process relaxes according to a single exponential with relaxation time τ , and $\rho(\tau, \alpha)$ is a distribution of relaxation timescale. the smaller α is, the broader is the distribution. More precisely, a stretched exponential means a relaxation faster than any exponential at small timescales, and slower than any exponential at long timescales.

We fit the experimental relaxation curves presented in the previous chapter with a stretched exponential to compare them. The value of the fitting parameters is given in Fig 6.6. We remark that the relaxation timescales are increasing by orders of magnitude between the low valency crosslinker: Fe^{3+} and the high valency crosslinkers: PolyMOC, nanoparticles. Moreover, the stretched exponent becomes smaller than 1 as the valency increases. Surprisingly, the value of the stretched exponent for the PolyMOC system depends on the temperature. α is usually associated with disorder in the material rather than fluctuations. While stretched exponentials are a popular fitting form for stress responses to a step strain [73, 74], existing microscopic models do not apply to the situation discussed here. Indeed, rationalizing the emergence of a whole distribution of timescales is often based on collective rearrangements in glass-like, dense assemblies of hard particles [75] or nonlinear elastic response regimes [76], neither of which is straightforwardly applicable to the system we are going to study. In the next chapter, we present our model based on the escape process of two large multivalent crosslinkers. Our model accounts for both the drastic increase in relaxation time and the proliferation of microscopic relaxation times.

Chapter 7

Modeling of the microscopic relaxation process

As we have just seen, hydrogels are versatile and can display various mechanical responses. To be able to design appropriate gels with the desired properties, we would like to be able to identify the mechanisms responsible for the emergence of a broad distribution of timescales as larger crosslinkers are introduced. To do so, we start by building a model for the microscopic process of relaxation. We propose that the elementary relaxation events in viscoelastic gels with high-valency crosslinks are essentially similar to those in the presence of low-valency ions. Elementary stress release events consist in the severing of the physical connection between two crosslinks. We first provide in section 7.1 a model for the breaking of a single polymer strand – called single bonds. We next describe the case of high-valency crosslinks in section 7.2. Such connections – hereafter termed “superbonds” – are comprised of several polymer strands. We then show in section 7.3 that survival probability of such a bond is a single exponential. Finally, we compute in section 7.4 the mean breaking time, which turns out to depend very strongly on the number of strands involved in it.

7.1 Dynamic of a single bond

Single bonds are made of polymers whose ends have been engineered by adding a nitrocatechol group that can bind to metal ions. Polymer ends are trapped into a potential. The unbinding of a single strand requires them to diffuse out of the trap. To do so, the polymer’s end must overcome an energetic barrier of height ΔE . It is possible to estimate the value of ΔE using stopped flow technique [77], which gives $\Delta E = 36k_B T$ at $398K$. Such a high value for the binding energy as compared to the thermal energy – $k_B T$ – makes the breaking of a single bond much slower than

the re-binding. We will consider the limit of very high energy by neglecting the unbound state of a polymer's end as illustrated in Fig 7.1. It means that the stress release in a single bond consists of the unbinding of one polymer's end, followed by its rebinding somewhere else. Except that the rebinding takes place without introducing any stress. In the case of large crosslinks, a given polymer strand can have both of its ends bound to the same crosslink. In the absence of entanglement, such a polymer strand becomes mechanically inactive. If the bound and unbound state have the same energy, it is not necessarily the same for their entropy. We now consider the entropic change ΔS between the two states. The entropy of a polymer strand depends on the distance between its two ends. Binding both ends to a single crosslink or to two different crosslinks does not bring about the same configurational entropy for the polymer. Finally, we respectively denote the binding and unbinding rates by :

$$\omega^+ = \frac{1}{\tau_0} e^{-\beta\Delta E} \quad \omega^- = \frac{1}{\tau_0} e^{-\beta\Delta E + \Delta S} \quad (7.1)$$

where τ_0 is a microscopic timescale. It corresponds to the time required for the end group of the polymer to move out of the binding potential.

7.2 A collection of single bonds: the superbond

We are interested in the relaxation of gels made of high valency crosslinks. It is thus possible that two crosslinks are held together via several polymer strands Fig 7.2. We now consider the dynamics of a superbond involving N polymer strands, and we assume that each strand attaches and detaches independently of the others. As a result, the probability $P_n(t)$ for n strands to span between the two crosslinks at time t satisfies the master equation as illustrated Fig 7.3 :

$$\begin{aligned} \partial_t P_n(t) = & - [r^+(n) + r^-(n)] P_n(t) \\ & + r^-(n+1) P_{n+1}(t) \\ & + r^+(n-1) P_{n-1}(t) \end{aligned} \quad (7.2)$$

where

$$\begin{cases} r^+(n) = \omega^+(N-n) \\ r^-(n) = \omega^- n \end{cases} \quad (7.3)$$

Which automatically implements a reflecting boundary condition that ensures that the number of bound polymers can never be greater than N . We discuss the physical origin of this boundary in the next section. In the following we rescale the time by the mean unbinding time, define as :

$$\tilde{t} = t/\tau_0 e^{-\beta\Delta E} \quad (7.4)$$

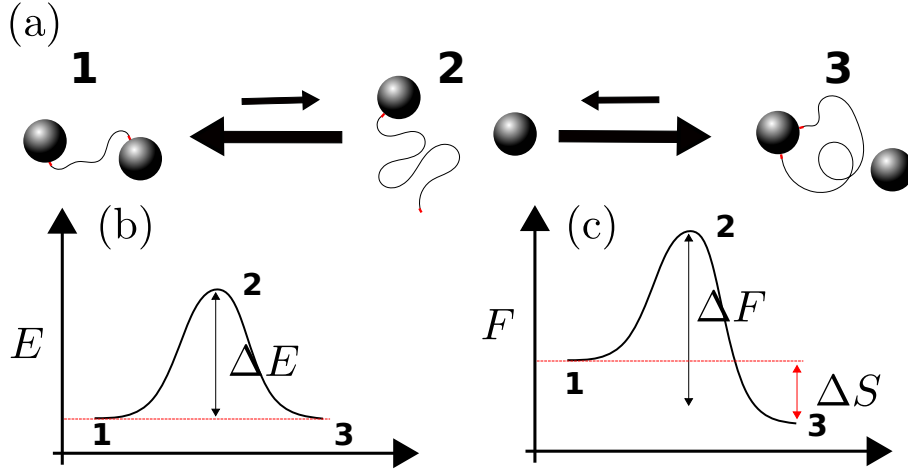


Figure 7.1: **Single-bond dynamics** : (a) Schematic of the unbinding process of a single bond between two crosslinks, represented as black spheres. (a) The unbinding ($1 \rightarrow 3$) or binding ($3 \rightarrow 1$) events pass through a state of high energy: (2) which makes it unstable, and that we neglect. (b) schematic of the energy along the coordinate of reaction. States (1) and (3) have the same energy, while (2) is very unstable. (c) schematic of the free energy ($F = E - TS$) along the coordinate of reaction. Although the energies of (2) and (3) are the same, their free energies should differ, since the entropy of a polymer with two bound ends depends on the distance of its two ends [78].

The parameters ΔE and τ_0 do not affect the dynamic. τ_0 sets the time unit, and ΔE encapsulates the temperature dependence of the time unit. An equivalent formulation that we will need later is to define a transition matrix Ω . Defining a probability vector $\mathbf{P} = (P_0(t), \dots, P_N(t))$, the master equation Eq (7.2) can be re-written :

$$\frac{d\mathbf{P}}{dt} = \Omega\mathbf{P}(t) \quad (7.5)$$

with :

$$\Omega_{i,j} = -\delta_{i,j}(r^-(i) + r^+(i)) + \delta_{i+1,j}r^-(i+1) + \delta_{i-1,j}r^+(i-1) \quad (7.6)$$

To determine the rate at which a superbond breaks, we define its survival probability $S(t) = \sum_{n=1}^N P_n(t)$ and set an absorbing boundary condition $r^+(0) = 0$. $S(t)$ is the probability that at time t the random walker has not yet reached 0. Indeed, once the random walker reaches 0 the two ligands can freely diffuse, the stress is relieved, future rebinding becomes irrelevant for the relaxation modulus in Fig 7.3.

To compute $S(t)$, we first determine the equilibrium distribution of bound polymers in the superbonds of the systems without the absorbing boundary condition.

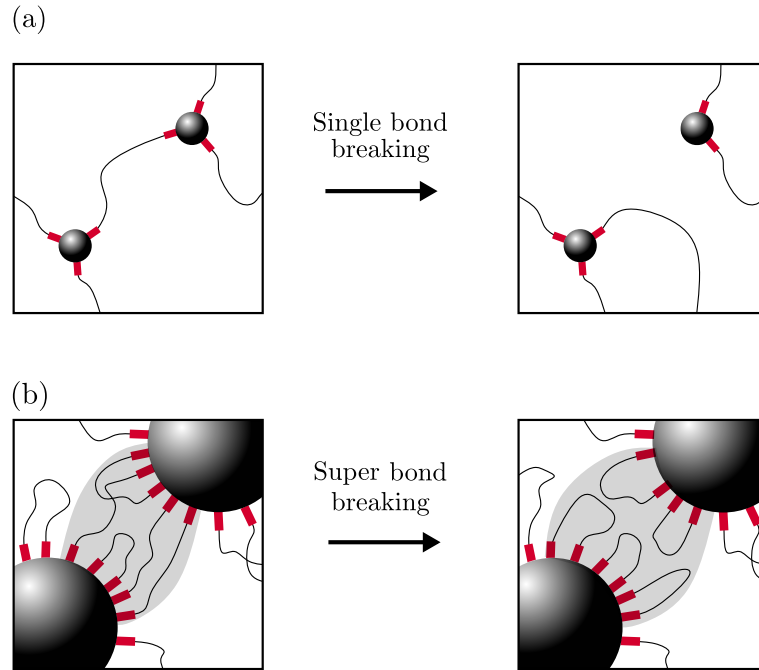


Figure 7.2: **Single vs Super bond** : (a) Tensile stresses between low-valency crosslinks are relaxed by the moving of a single polymer strand. This results in an exponential stress relaxation whose time constant is associated with the unbinding of a single strand from a crosslink. (b) In contrast, the relaxation of stress in a network formed from high valency crosslinks typically requires the simultaneous unbinding of all the strands in the shaded region, which represents a “superbond”.

The equilibrium distribution corresponds to the stress-free situation, before the strain is applied. Solving Eq. (7.2) with $\partial_t P_n(t) = 0$ gives a binomial distribution :

$$P_{\text{eq},n}(N, P_{\text{off}}) = P_{\text{off}}^{N-n} (1 - P_{\text{off}})^n \binom{N}{n} \quad (7.7)$$

It is our initial condition: $P_n(0) = P_{\text{eq},n}$ with $P_{\text{off}} = 1/(1 + e^{-\Delta S})$, the probability for and individual polymer strand to not be involved in a superbond. Computing the survival probability then reduce to solving the master equation with the initial condition P_{eq} to find $\forall t > 0$ and $\forall n \in \mathbb{N}$: $P_n(t)$.

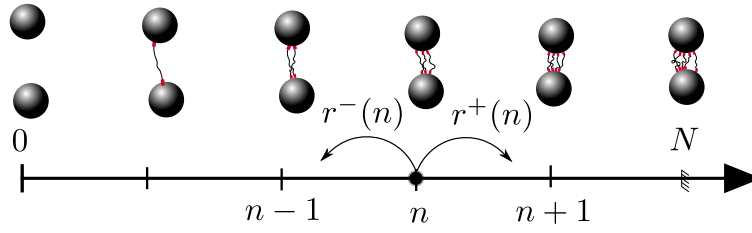


Figure 7.3: **Analogy between the breaking process of a superbond, and a 1D random walk.** The metal ion ligands are represented as two spheres, which are linked by polymers strands. Only polymers that are actually involved in the superbond are represented. The random walk has two boundary conditions. Absorbing in 0: the stress is finally relieved whenever all polymer strands are unbound from the superbond. Reflective in N , N defines the maximum number of bond that either the ligand can carry or that the polymer concentration can provide.

7.3 Computation of the survival probability of a superbond

Solving the full master equation is not an easy problem. To do so, we use a Kramer-like approximation that we also call small leak assumption. In this context, it means considering that adding the absorbing boundary condition in 0 – the leak – almost does not perturb the distribution of bonds. We first give a quick understanding of why this approximation leads the survival probability to be a single exponential. In section 7.3.1, we give a semi-quantitative argument for the survival probability to be almost a single exponential. We then provide a numerical argument in section 7.3.2 to settle the validity of this approximation. Finally, in section 7.4 we will derive more rigorously the mean escape time of this process and show the consistency with our previous arguments.

7.3.1 Quick argument

Considering that the leak is small, means that the time requires to break the last bond is large as compared to the inner dynamic time of binding/unbinding of bonds. It reads: $P_{\text{eq},1}(t)r^-(1) \ll \omega^+$, replacing P_{eq} and r^- by their expression from Eq (7.7) and Eq (7.3) gives $NP_{\text{off}}^{N-2}(1 - P_{\text{off}})^2 \ll 1$. This separation of timescale means that the shape of the probability distribution of bonds is similar to the equilibrium one. However, the leak reduces the total probability. We are looking for a probability distribution that has the same shape as P_{eq} and that

ensure the normalization: $\sum_{n=1}^N P_n(t) = 1 - P_0(t)$, which gives :

$$P_n(t) = P_{\text{eq},n}(1 - P_0(t)) \quad (7.8)$$

We can then write the differential equation for $S(t) = 1 - P_0(t)$ using Eq (7.2) for $n = 0$, to obtain :

$$\begin{aligned} \partial_t P_0(t) &= r^-(1)P(1, t) \\ &= \omega^- P_{\text{eq},1} [1 - P_0(t)] \end{aligned} \quad (7.9)$$

which finally gives

$$\partial_t S(t) = \omega^- P_{\text{eq},1} S(t) = N\omega^- P_{\text{off}}^{N-1} (1 - P_{\text{off}}) S(t) \quad (7.10)$$

The full form of the survival probability is a single exponential

$$S_N(t) = \exp(-t/\tau_N) \quad (7.11)$$

with a relaxation time given by :

$$\bar{\tau}_N = \frac{\tau_0 e^{\beta\Delta E}}{N P_{\text{off}}^N} \quad (7.12)$$

In this approximation, the time required to break a superbond is exponential with a characteristic time that itself displays an exponential dependency with N . N is a boundary condition and appears as a crucial parameter. The next chapter is dedicated to its computation.

7.3.2 Numerical argument

We gave a quick argument supporting that the survival probability is a single exponential. We are now going to use numerical tools to reinforce the assumptions used in the previous section. Looking at the transition matrix in Eq (7.5), saying that the distribution is not perturbed by the leak in $n = 0$, means that the equilibrium distribution vector \mathbf{P}_{eq} is almost an eigenvector: $\Omega \mathbf{P}_{\text{eq}} \approx \lambda \mathbf{P}_{\text{eq}}$. To check this, we numerically compute and diagonalize Ω , noting $\{\lambda_i\}$ the ordered $-\lambda_0$ the smallest- eigenvalues, and $\{\mathbf{Q}_i\}$ the associated eigenvectors. We then plot the scalar product of \mathbf{P}_{eq} with the eigenvector associated to the smallest eigenvalue: \mathbf{Q}_0 in Fig 7.4. For a broad range of values of the two parameters P_{off} and N , the scalar product is around 1, which means that \mathbf{P}_{eq} is almost parallel to this eigenvector. \mathbf{P}_{eq} almost parallel to \mathbf{Q}_0 has two effects. On the one hand, it means $\forall t > 0 \mathbf{P}(t) \sim \mathbf{P}_{\text{eq}}$. On the other hand because \mathbf{P}_{eq} is also the initial condition, it means that the relaxation mostly occurs over this precise mode.

Once Ω diagonalized, the exact solution is :

$$\mathbf{P}(t) = \sum_i \mathbf{Q}_i e^{\lambda_i t} \quad (7.13)$$

A couple eigenvalue/eigenvector $(\lambda_i, \mathbf{Q}_i)$ is called a mode of relaxation. To understand what is happening with the other modes of relaxation, we plot the ratio of the smallest to the second smallest eigenvalue: λ_0/λ_1 in Fig 7.4. Small eigenvalue means a long relaxation time, therefore, the relaxation time associated to \mathbf{P}_{eq} is the largest one by orders of magnitude. To summarize, the survival probability is the sum of all eigenmodes, each relaxing exponentially. The starting point is the equilibrium distribution. Because P_{eq} is almost an eigenvector, most of the relaxation happens over this mode. Moreover, this mode has a relaxation time larger by orders of magnitude than every other. Which means even with a different initial condition, all other modes would relax quasi instantly, and only remains the slowest one. Eq (7.13) becomes a single exponential.

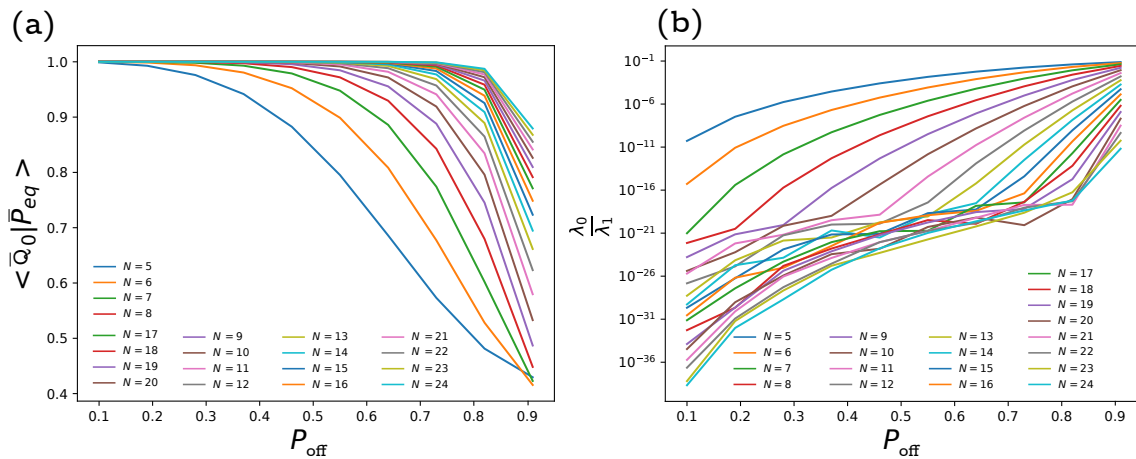


Figure 7.4: **Comparison between \mathbf{P}_{eq} and \mathbf{Q}_0 :** (a) scalar product between the equilibrium probability distribution and the eigenvector associated to the smallest eigenvalue. (b) The ratio λ_1/λ_0 is plotted as a function of P_{off} .

7.4 Calculation of $\bar{\tau}(N)$

We have given a quick physical argument, then a numerical one for a survival probability being a single exponential. We now use a more mathematical one. We compute the mean escape time of a random walker that starts in m with a reflective boundary condition in N : $\bar{\tau}_{m,N}$. To do so, we start by using the general

exact formula for the mean escape time of a one-step process from [79]. It is the mean escape time for the symmetrical problem with an absorbing boundary condition in N , reflective in 0 knowing that the random walker started in m , which gives :

$$\bar{\tau}_{m,N} = \sum_{\nu=m}^{N-1} \sum_{\mu=0}^{\nu} \frac{\prod_{i=\mu+1}^{\nu} i \omega^+}{\prod_{i=\mu}^{\nu} (N-i) \omega^-} \quad (7.14)$$

In the following, we are going to use this formula to simplify it. Starting with a few mathematical manipulations, we remark that $\frac{\omega^+}{\omega^-} = e^{-\Delta S}$, we re-write $\bar{\tau}_{m,N}$:

$$\bar{\tau}_{m,N} = \sum_{\nu=m}^{N-1} \sum_{\mu=0}^{\nu} \frac{e^{-(\nu-\mu)\Delta S}}{\omega^-} \frac{\prod_{i=\mu+1}^{\nu} i}{\prod_{i=\mu}^{\nu} (N-i)} \quad (7.15)$$

We can write the two products of the fraction using the identities :

$$\begin{aligned} \prod_{i=\mu+1}^{\nu} i &= \frac{\nu!}{\mu!} \\ \prod_{i=\mu}^{\nu} (N-i) &= \prod_{k=N-\nu}^{N-\mu-1} k = \frac{(N-\mu-1)!}{(N-\nu-1)!} \end{aligned} \quad (7.16)$$

which leads to :

$$\bar{\tau}_{m,N} = \sum_{\nu=m}^{N-1} \sum_{\mu=0}^{\nu} \frac{e^{-(\nu-\mu)\Delta S}}{\omega^-} \frac{\nu! (N-\nu-1)!}{\mu! (N-\mu)!} \quad (7.17)$$

We can separate the sum over ν and the one over μ which gives Eq (7.18).

$$\frac{1}{\omega^-} \sum_{\nu=m}^{N-1} e^{-\nu\Delta S} \nu! (N-\nu-1)! \sum_{\mu=0}^{\nu} \frac{e^{\mu\Delta S}}{\mu! (N-\mu)!} \quad (7.18)$$

Here, we recognize a binomial coefficient :

$$\frac{1}{\mu! (N-\mu)!} = \frac{1}{N!} \binom{N}{\mu} \quad (7.19)$$

and then use the formula of Newton Binomial,

$$(x+y)^N = \sum_{k=0}^N \binom{N}{k} x^k y^{N-k} \quad (7.20)$$

which leads to :

$$\sum_{\mu=0}^{\nu} \frac{e^{\mu\Delta S}}{\mu! (N-\mu)!} = \frac{1}{N!} \left[(1 + e^{\Delta S})^N - \sum_{\mu=\nu+1}^N e^{\mu\Delta S} \binom{N}{\mu} \right] \quad (7.21)$$

Using this in the Eq (7.18) leads to:

$$\begin{aligned} \bar{\tau}_{m,N} = & \underbrace{\frac{(1 + e^{\Delta S})^N}{\omega^- N!} \sum_{\nu=m}^{N-1} e^{-\nu \Delta S} \nu! (N - \nu - 1)!}_{\text{Saddle point approximation}} \\ & - \underbrace{\frac{1}{\omega^- N!} \sum_{\nu=m}^{N-1} e^{-\nu \Delta S} \nu! (N - \nu - 1)! \sum_{\mu=\nu+1}^N e^{\mu \Delta S} \binom{N}{\mu}}_{\text{negligible term}} \end{aligned} \quad (7.22)$$

We then use a saddle point approximation on the first term, which means that the last term ($\nu = N - 1$) dominate the sum of all others provided that :

$$\frac{P_{\text{off}}}{1 - P_{\text{off}}} \frac{1}{N - 1} \ll 1. \quad (7.23)$$

For this to be valid, we need $\Delta S < 0$ which is true in practice, otherwise this approximation is not valid anymore -other approximations leading to the same result are, however, still possible.

The computation of the validity of the saddle point approximation as well as the negligibility of the second term is not reported here. Ultimately, these two approximations give a simple formula for $\tau_{m,N}$:

$$\bar{\tau}_{N,m} = \bar{\tau}_N = \frac{\tau_0 e^{\beta \Delta E}}{N P_{\text{off}}^N} + \mathcal{O} \left(\frac{P_{\text{off}}}{1 - P_{\text{off}}} \frac{1}{N - 1} \right) \quad (7.24)$$

Here we recognize $\bar{\tau}_N = 1/(P_{\text{eq}}(1)\omega^-)$ as in Eq (7.10), which is the time required to break the last bond of the superbond. This result confirms that a single relaxation time dominates the breaking of a superbond. Notice that we started computing $\bar{\tau}_{m,N}$ but finally obtained $\bar{\tau}_N$, which does not depend on the starting point anymore. This is an important result. It means that the relaxation of the gel does not depend on the initial state before the strain was being applied, instead it does depend on N the maximum number of bonds a superbond can carry. Physically, it means that no matter how many polymer strands are involved in a given superbond at the beginning of the process, the additional binding of more strands is so much more likely than the unbinding, that a superbond is almost guaranteed to reach a state where it has N strands. Reaching this state is so certain that the information of the starting point becomes irrelevant. The next chapter is dedicated to the computation of N .

Chapter 8

Two mechanisms can limit a super-bond lifetime

In the previous section, we derived the mean breaking time for a superbond that turned out to be determined by the maximum number of bonds a superbond can carry N . This limit can either be due to the amount of polymer available or imposed by the valency of the ligands. Here we consider both limits, starting in section 8.1 by modeling the distribution of polymers available in the system. We then look in section 8.2 at how the valency modifies this distribution. Now we can compute N , we present how we compute the relaxation modulus in section 8.3, and show that the properties of the relaxation modulus found reproduce the behavior associated with the stretched exponential. However, the experimental system introduced in section 6.2 also displays an interesting behavior, such as a stretched exponential that sometimes depends on the temperature – polyMOC system –, and sometimes does not – nanoparticle system–. We show in section 8.4 that our model provides an interpretation for this phenomenon.

8.1 Polymer availability limitation

To determine N in a superbond, we start by taking into account the polymer concentration limitation. The polymer strands used are 4-arm PEG star polymers. It is well known that star polymers diffuse extremely slowly [80], moreover, these polymer strands are bound to crosslinkers with an escape time – $\tau_0 e^{\beta \Delta E}$ – of the order of 1s. This very slow diffusion means that the time required for the polymer strands to homogenize in solution is much larger than the experimental time. We, therefore, consider the polymer strands in the solution to not be diffusive at all. If the polymers are not diffusing, their local concentration is determined at the beginning of the experiment and then fixed.

To compute the distribution of polymer in the system, we discretized the system into a small box of volume v (v would be the volume over which the polymer can diffuse during the overall time of the experiment). We add the polymers one by one in a random box chosen according to a uniform probability. The probability that a given box contains n polymers of PEG is given by a Poisson distribution :

$$P(n, v) = \rho_{\text{PEG}}^n \frac{\exp(-\rho_{\text{PEG}}v)}{n!} \quad (8.1)$$

where ρ_{PEG} is the average concentration of PEG in the system. Assuming then that inside the box of volume v the PEGs are free to diffuse means that the concentration inside each box is homogeneous. We write the number of single bonds between two nanoparticles N . For a box that contains n polymer strands, it gives :

$$N = \frac{n}{\rho_{\text{NP}}v} \quad (8.2)$$

with ρ_{NP} the average concentration of nanoparticles in the system (assumed to be homogeneous). From this, we can write the probability of having N bonds in a superbond :

$$P(N, v) = (\rho_{\text{PEG}}v)^{\rho_{\text{NP}}Nv} \frac{\exp(-\rho_{\text{PEG}}v)}{(\rho_{\text{NP}}vN)!} \rho_{\text{NP}}v \quad (8.3)$$

In this equation, the volume of the box v is the only parameter that is not fixed by the experimental conditions. As said previously, the polymers are assumed to not diffuse at all, v is thus the volume of one single superbond, which reads: $\rho_{\text{NP}}v \rightarrow 1$. Denoting $\bar{N} = \rho_{\text{PEG}}v$: the average number of polymer strands in a superbond throughout the whole system, we get :

$$P(N) = \frac{\bar{N}^N e^{-\bar{N}}}{N!} \quad (8.4)$$

8.2 Valency limitation

Secondly, we consider the intrinsic limit of binding sites on a ligand imposed by the valency. We call this limit N_{cut} . It is proportional to the valency of the ligands that is constant throughout the system. To summarize, the polymer concentration initially constrains N , then once the concentration of polymer is sufficiently large to allow for a maximum number of bonds N higher than N_{cut} , then the crosslink's valency turns out to be the limiting factor. To include both effects in the probability distribution of Eq(8.4), we set all the $N > N_{\text{cut}}$ to be equal to N_{cut} and

finally obtain :

$$P(N) = \begin{cases} \frac{\bar{N}^N e^{-\bar{N}}}{N!} & \forall N \in [1, N_{\text{cut}}[\\ \sum_{N_{\text{cut}}}^{\infty} \frac{\bar{N}^N e^{-\bar{N}}}{N!} & \text{if } N = N_{\text{cut}} \\ 0 & \text{if } N > N_{\text{cut}} \end{cases} \quad (8.5)$$

This distribution of bond number is essentially the distribution fixed by the polymer concentration. However, when a local excess of polymer concentration overcomes the number of available binding sites, it does not create a new single bond in a superbond. The case $N = N_{\text{cut}}$ in Eq (8.5): $\sum_{N_{\text{cut}}}^{\infty} \frac{\bar{N}^N e^{-\bar{N}}}{N!}$ is nothing else than the probability of having an excess of polymer.

8.3 Derivation of the relaxation modulus

Having now computed the survival probability of an individual superbond Eq (7.3), as well as the distribution of polymer strands involved in a superbond Eq (8.5), we now derive the relaxation modulus $G(t) = \sigma(t)/\sigma(0)$. We use the framework introduced in section 6.3.2 for ideal networks. In the case of a homogeneous network made of single bonds, Eq (6.5) gives the relation between the relaxation modulus and the survival probability of a single bond. Here, instead, the polymer strands that compose a superbond are assumed not to be diffusive at all, making the hydrogel a quenched material. We write the total stress in the material as a sum over the contribution of all superbonds that contain N polymer strands :

$$\sigma(t) = \sum_N^{\infty} \sigma_N(t) \quad (8.6)$$

where $\sigma_N(t)$ is the part of the stress carried by all superbonds made of N polymer strands. Assuming an affine deformation means that each superbond carries the same stress :

$$\sigma(t) = \sigma(0) \sum_N^{\infty} \frac{\mathcal{N}_N(t)}{\mathcal{N}_{\text{tot}}(0)} \quad (8.7)$$

where $\mathcal{N}_N(t)$ is the number of superbonds made of N polymer strands that carry stress at time t , and $\mathcal{N}_{\text{tot}}(0)$ is the initial total number of superbonds in the system. Eq (8.7) means that the fraction of the stress carried by superbonds made of N polymer strands at time t , is equal to the fraction of bond number that carry stress at time t . In the thermodynamic limit of large number of bonds, we can write the survival probability as :

$$S_N(t) = \frac{\mathcal{N}_N(t)}{\mathcal{N}_N(0)} \quad (8.8)$$

where $\mathcal{N}_N(0)$ is the number of superbonds made of N polymer strands at the beginning of the experiment. It is determined by the quenched process described section 8.1 and section 8.2, which gives :

$$P(N) = \frac{\mathcal{N}_N(0)}{\mathcal{N}_{\text{tot}}} \quad (8.9)$$

Using Eq (8.8) and Eq (8.9) into Eq (8.7) finally gives :

$$G(t) = \sum_{N=0}^{\infty} P(N) S_N(t) \quad (8.10)$$

We finally write the relaxation modulus by substituting the expressions of the survival probability Eq (7.11) and the superbond N distribution Eq (8.5) to obtain :

$$G(t) = \sum_{N=1}^{N_{\text{cut}}-1} P(N) e^{-t/\tau_N} + e^{-t/\tau_{N_{\text{cut}}}} P(N_{\text{cut}}) \quad (8.11)$$

Eq (8.11) splits the relaxation modulus into two terms, depending on the mecha-

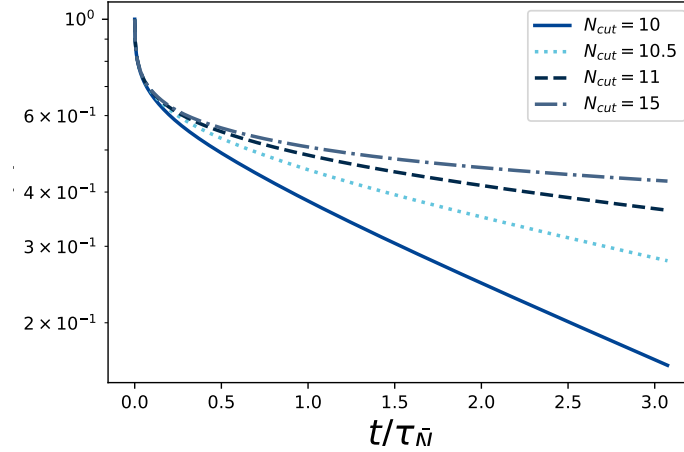


Figure 8.1: **Influence of N_{cut} on $G(t)$** : We plot the expression for $G(t)$ given in Eq(8.11) with the parameters: $\beta\Delta E = 0$, $\tau_0 = 10^{-3}$, $P_{\text{off}} = 0.2$, $\bar{N} = 10$, for several values of N_{cut} . We notice that as N_{cut} becomes closer to \bar{N} , not only the relaxation becomes faster, but also more exponential.

nism that limits the number of polymer strands. The first mechanism dominates the short-time relaxation $- t < \tau_{N_{\text{cut}}}$ - displays a superposition of several exponential relaxation modes. Its characteristics depend on the average polymer concentration and variance in the system through $P(N)$ as explained in section 8.1. The

second mechanism dominate at long time – $t > \tau_{N_{\text{cut}}}$ – gives a single exponential relaxation, whose characteristic time is fixed by the valency of the ligand as explained in section 8.2. Fig 8.1 shows the two different regimes. The semi-logarithmic scale emphasizes the transition between the first and the second regime, the latter appearing as a straight line. A convenient way to show the influence of the valency of the crosslinkers on the relaxation modulus is to fit the curve obtained for our model with a stretch exponential as defined in Eq (6.7) for a range of value of N_{cut} . An example of such a series of fits is given in Fig 8.2 showing the very good agreement between these two models, with a coefficient of determination r^2 always higher than 0.98. The model we used has five adjustable parameters – ΔE , ΔS , τ_0 , \bar{N} and N_{cut} – while the stretched exponential has only two – α and τ –. However, the model we designed provides a physical interpretation of the influence of the different parameters, such as of the valency of the crosslinkers. It is illustrated by the comparison with the stretched exponential, as it reveals a strong dependence of the characteristic timescale on the valency of the crosslinkers -as expected from the experiments- as shown in Fig 8.3. Moreover, we observe that it is possible to effectively tune the stretching exponent, α over the whole possible range $[0; 1]$ by varying the valency of the crosslinkers as shown in Fig 8.3.

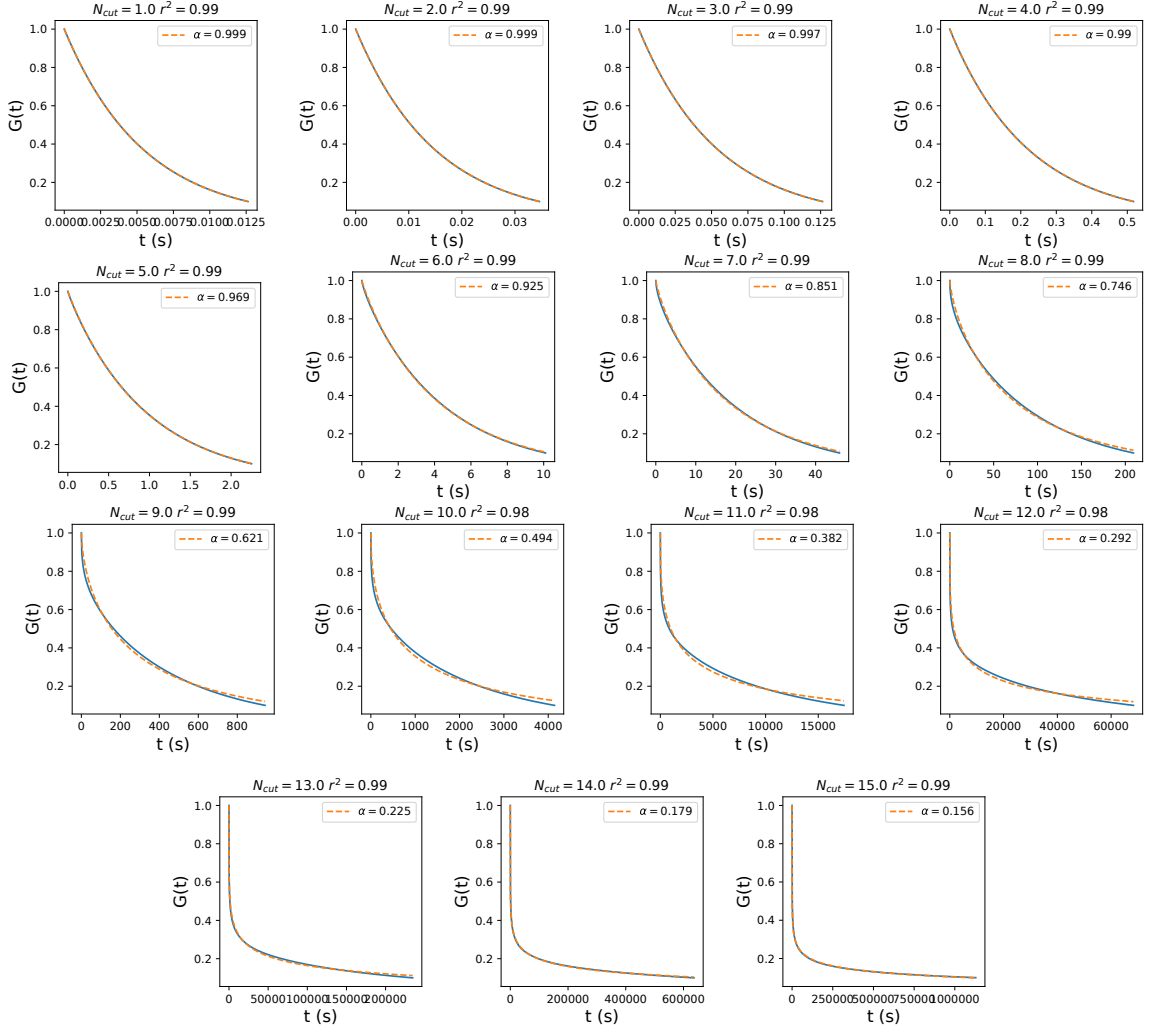


Figure 8.2: **Series of fits of the relaxation modulus modeled:** We plot the relaxation modulus modeled for $N_{\text{cut}} \in [1; 15]$, with $\beta\Delta E = 0$, $\tau_0 = 10^{-3}$, $P_{\text{off}} = 0.2$, $\bar{N} = 10$, on top of which a stretch exponential fit is given, with the stretching exponent given as a legend. The correlation coefficient of the fit: r^2 is also given as a title. The relaxation time varies very strongly with N_{cut} , we thus have to adapt the interval over which the curves are fitted. In a real experiment, we are interested in the timescale where most of the stress relaxes. We determine the time interval $[0; t_{\text{max}}]$ by imposing that the relaxation modulus has relaxed by 90% at t_{max} . We demonstrate here, that the model derived can be associated to a stretched exponential. Moreover, on a practical level, we show the influence of the parameter N_{cut} – which itself depends on the valency – on the stretched exponent.

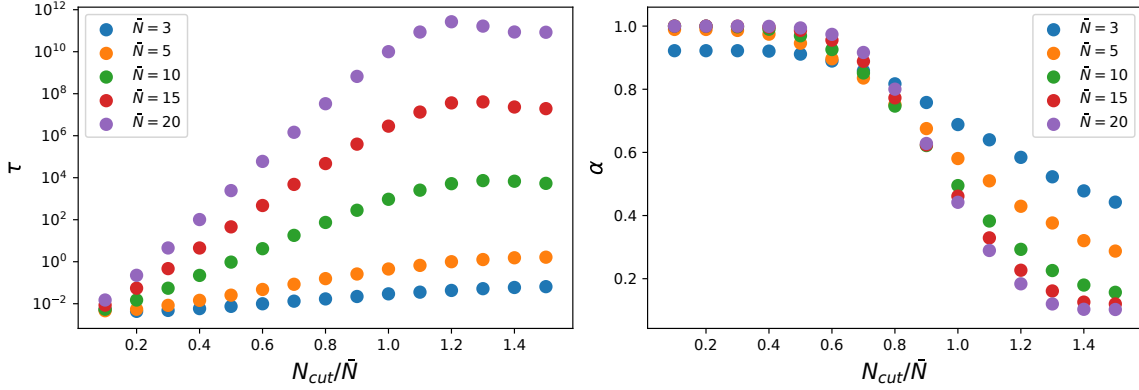


Figure 8.3: **Summary of the stretched exponential fits** : We did a series of fits as presented Fig 8.2. Here, we plot the variation of the two fitting parameters for the stretched exponential: τ and α as a function of N_{cut}/\bar{N} . τ increases over orders of magnitude with growing valency. α seems to converge toward a finite value. However, it is an artifact due to the finite-time interval of the fit. Indeed, we showed that for $N_{\text{cut}} \rightarrow +\infty$ $G(t) \underset{t \rightarrow \infty}{\sim} e^{-\log(t)^2}$. This long-time scaling cannot be reproduced by a stretched exponential.

8.4 The $\alpha(T)$ paradox

Finally, we give more details about our interpretation of the fact that the stretch exponent α of the polyMOC system depends on the temperature, while it is not the case of the nanoparticle's system. Indeed, Fig 8.4 represent the relaxation modulus $G(t)$ and the stretched exponential fit, for different temperatures, in two different case: high valency $N_{\text{cut}} \gg \bar{N}$ and intermediate/low valency $N_{\text{cut}} \approx \bar{N}$. We can observe that in the case where the relaxation is dominated by the mix of relaxation time (high valency), the temperature dependence of the stretched exponent α is small compared to the regime with a smaller valency. In the next chapter, we will show that the latter corresponds to the case of the polyMOC.

The relaxation modulus that we derived uses more parameters than the stretched exponential one. One of the reasons for this is that we included a temperature dependency. This temperature dependency turns out to be rewarded, as we can give a physical interpretation of what appeared at first as a paradox.

8.5 About power-law stress relaxation

We have previously discussed the implications of our microscopic mechanism for the relaxation of the stress – superbond breaking – on the relaxation modulus. This

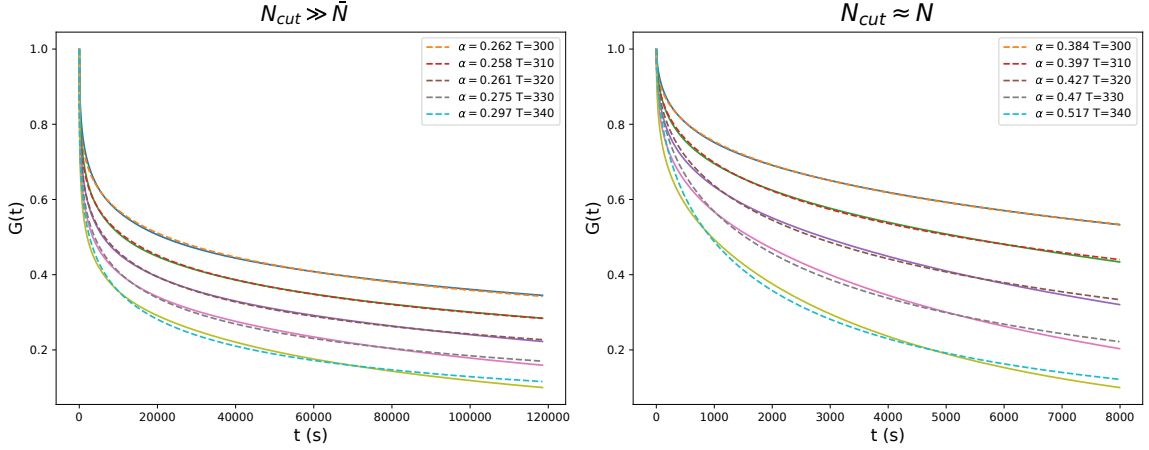


Figure 8.4: α - \mathbf{T} dependency: Left, when the relaxation is dominated by the superposition of timescales $\bar{N} \gg N_{\text{cut}}$, the α dependence is weak with the temperature. Right on the contrary, when the relaxation has an exponential tail, or dominated by the limit imposed by the valency, the α dependency with the temperature is stronger. The parameters used here are: $\Delta E = 20(k_B \times 300K)$, $P_{\text{off}} = 0.2$, $\tau_0 = 10^{-9}$, $\bar{N} = 8$, $N_{\text{cut}} = 10$ left, and $N_{\text{cut}} = 8$ right.

analysis will allow us in the next chapter to make a quantitative comparison with experimental measurements. However, it is worth to mention that the previous calculation can easily be extended to account for other non-exponential relaxations. Indeed, many systems such as protein gels [81, 82], living cells [83], ring polymers [84] all exhibit a power law decay of the stress when submitted to a constant strain. In this section, we use an exponential distribution of single bonds in the superbonds and show that this choice leads to a power law relaxation of the stress.

Let us consider the following distribution of single bonds in a superbond :

$$P(N) = \frac{1}{\bar{N}} \exp\left(-\frac{N}{\bar{N}}\right) \quad (8.12)$$

where \bar{N} is the average number of single bonds involved in a superbond. We can straightforwardly apply Eq 8.10 to obtain a new relaxation modulus that is plotted in Fig 8.5 (b,c) in plain line. Fig 8.5 (b,c) reveals the emergence of a power law in the relaxation modulus, which appears as a straight line in the log-log plot.

To further confirm this observation, we now derive an expression for the exponent of the power law. To do so, we use an approximation of Eq 7.24 for the mean escape time :

$$\bar{\tau}(N) = \frac{\tau_0 e^{\beta \Delta E}}{N P_{\text{off}}^N} \approx \frac{\tau_0 e^{\beta \Delta E}}{\bar{N} P_{\text{off}}^N} \propto P_{\text{off}}^{-N} \quad (8.13)$$

This approximation enables us to compute the full distribution of relaxation time by using :

$$P(N)dN = P(\bar{\tau})d\bar{\tau} \quad (8.14)$$

Which gives :

$$\begin{aligned} P(\bar{\tau}) &= \frac{1}{\log(P_{\text{off}})} (\bar{N} e^{\beta \Delta E} \bar{\tau})^{\frac{1}{N \log(P_{\text{off}})} - 1} \\ &\propto \bar{\tau}^{\frac{1}{N \log(P_{\text{off}})} - 1} \end{aligned} \quad (8.15)$$

Similar to Eq 8.10 we write the relaxation modulus as a sum over all the microscopic timescales, except that the distribution of microscopic timescales is now continuous:

$$\begin{aligned} G(t) &= \int_0^\infty P(\bar{\tau}) e^{-t/\bar{\tau}} d\bar{\tau} \\ &= \frac{(\bar{N} e^{\beta \Delta E})^{\frac{1}{N P_{\text{off}}}}}{\log(P_{\text{off}})} \Gamma\left(-\frac{1}{N \log(P_{\text{off}})}\right) t^{\frac{1}{N \log(P_{\text{off}})}} \\ &\propto t^{\frac{1}{N \log(P_{\text{off}})}} \end{aligned} \quad (8.16)$$

We compare this approximation with the exact computation in Fig 8.5 (b,c). In this example we have not considered the intrinsic limit of binding sites of the crosslinkers. Doing so would give the following distribution of bonds:

$$P(N) = \begin{cases} \frac{1}{N} \exp\left(-\frac{N}{N_{\text{cut}}}\right) & \text{for } N < N_{\text{cut}} \\ \sum_{N=N_{\text{cut}}}^{\infty} \frac{1}{N} \exp\left(-\frac{N}{N_{\text{cut}}}\right) & \text{for } N = N_{\text{cut}} \end{cases} \quad (8.17)$$

which results in a transition from a power law relaxation at short-times to an exponential relaxation at larger times, as illustrated in Fig 8.5 (c).

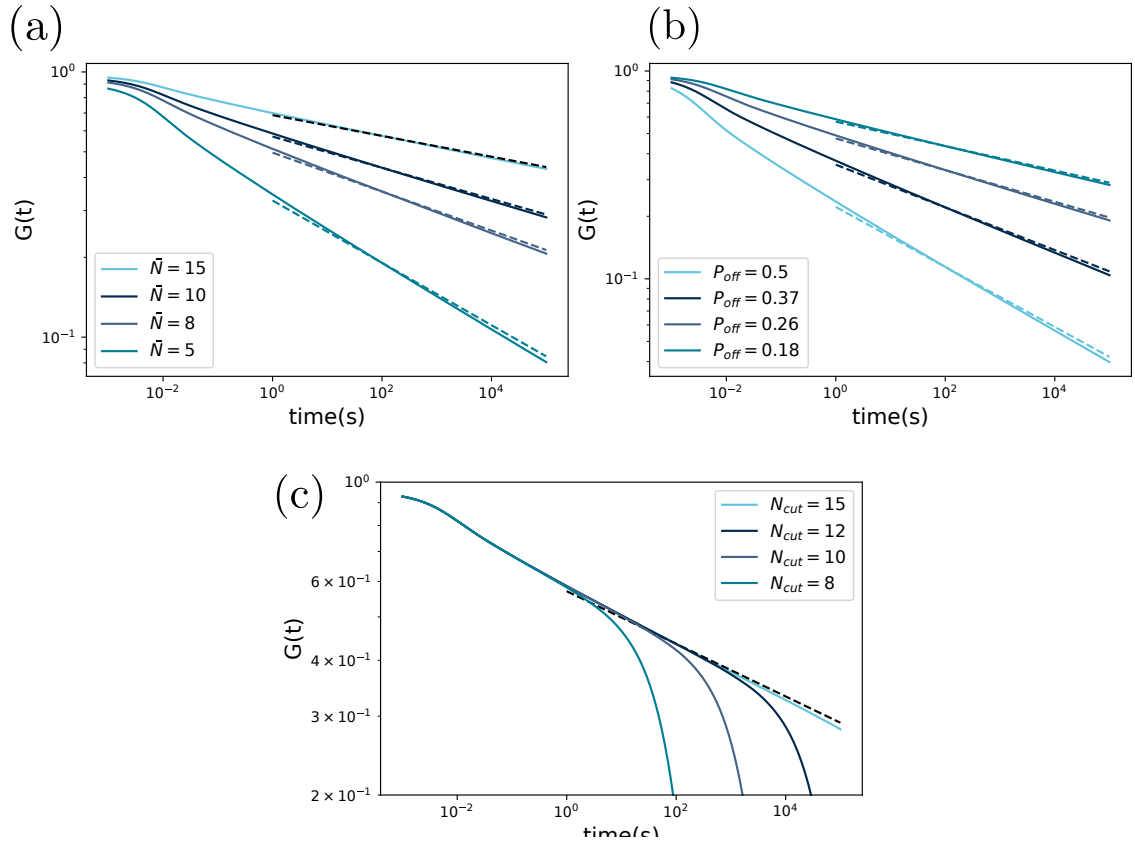


Figure 8.5: **Power law relaxation modulus** : (a,b) We plot the exact relaxation modulus derived by summing over the discrete relaxation time as plain line and the power law approximation derived in Eq 8.16 as dotted line. The parameters used here are: $\beta\Delta E = 0$, $\tau_0 = 10^{-3}$, $N_{cut} \rightarrow \infty$ and (a): $P_{off} = 0.18$, (b): $\bar{N} = 10$. (c) relaxation modulus with finite N_{cut} the parameters used are $\beta\Delta E = 0$, $\tau_0 = 10^{-3}$, $P_{off} = 0.18$ and $\bar{N} = 10$. We observe a power law relaxation at short-time. The rest of the relaxation is exponential. The power law approximation derived in Eq 8.16 is also displayed showing its extended validity.

Chapter 9

Comparison with the experiment

In the previous chapter, we derived an analytic formula for the relaxation modulus $G(t)$ of hydrogels crosslinked with high valency crosslinkers. This theoretical approach establishes a link between the valency of the crosslinkers and the stretched exponent. To validate this approach, we will now compare it with the experiment introduced in section 6.2 by fitting the relaxation modulus measured. This fitting process requires adjusting 4 parameters for 5 – at 5 different temperatures – curves per type of crosslinker: τ_0 a microscopic diffusion time, ΔE the binding energy of the polymer on the ligands, P_{off} the probability of a given polymer strand to be bound between two ligands, \bar{N} the average maximum number of bonds between ligands. The intrinsic limit of single bond in a super bond : N_{cut} , however, is not used as a fitting parameter. Instead, we start by computing it for each ligand in section 9.1 by introducing a simple model to link the valency and the parameter N_{cut} . ΔE is then measured in section 9.2 using the time-temperature collapse of the relaxation curves at different temperatures. The remaining parameters are then determined in section 9.3 by minimizing the squared distance between the experimental points and the relaxation modulus of Eq (8.11).

9.1 Valency and N_{cut}

N_{cut} is the upper limit of the number of polymer strands a superbond can carry. To establish a link between N_{cut} , the valency and the topology of the hydrogel, we consider a crosslinker saturated by polymer strands. If the polymer strands are homogeneously shared between all nearest neighbors of the considered crosslinker, we write the following relation :

$$N_{cut} = \frac{N_{valency}}{z} \quad (9.1)$$

where N_{valency} is the valency of the crosslinker and z is the number of nearest neighbors a crosslinker has. To model the number of nearest neighbors of a crosslinker, we model the crosslinker organization in the system using a regular lattice. Hydrogels are not dense systems such as crystals, we will thus not consider a compact packing of crosslinkers. However, hydrogels are mechanically rigid. For a spring network to be mechanically rigid without pre-strain, each degree of freedom – here the crosslinkers – have to be connected by at least $2 \times d$ other crosslinkers, where d is the dimension of the space [85]. We choose for the crosslinker organization the lowest coordinated regular lattice that guarantees a mechanical response: a cubic lattice, which confers them 6 nearest neighbors. We then design distinct models to deduce the valency of each crosslinker. Starting with the simplest, the Fe^{3+} ions have a fixed valency that has been measured by our experimental collaborator of 3, which gives $N_{\text{cut}} = 3/6 = 0.5$. Having half of a single bond involved in a superbond does not make sense. The Fe^{3+} ions can only form a network with a connectivity of 3. We thus round up to $N_{\text{cut}} = 1$. Concerning the Poly MOC system, the cage are made of 14 ions, each of them binds to one polymer [66], which set the valency, and gives $N_{\text{cut}} = 14/6 = 2.33$. Finally, we assumed that the valency of the nanoparticles crosslinkers is limited by the entropic cost of squeezing polymers together around a nanoparticle. Given the ratio of concentration of polymer per nanoparticle in the system -80 polymers/nanoparticles-, it turns out that the entropic cost required to bind each of the 80 polymers is very small compared to the binding energy at room temperature. Therefore, we consider the ratio of concentration to be limiting and obtain $N_{\text{cut}} = 80/6 = 13.3$.

9.2 Collapsing of the relaxation curves

Here we determine the value of the binding energy ΔE . Looking at the formula section 8.3, Eq (8.11), one can notice that the temperature dependence of the relaxation modulus can be eliminated by a rescaling of the time $\tilde{t} \rightarrow te^{\beta\Delta E}$. We are testing this prediction by collapsing all relaxation curves of a given system using an optimized procedure that we detail here.

For each type of ligand, we have a data set of 5 relaxation moduli $-G(t)-$ each at a different temperature: $\{T_i\}_{i \in [0,4]} = \{25^\circ C, 35^\circ C, 45^\circ C, 55^\circ C, 65^\circ C\}$. To find the optimal coefficients, we minimize a cost function that takes as an argument a set of rescaling coefficients $\{a_i\}$ and perform a rescaling of the time as following: $t' \rightarrow te^{a_i}$. Then compute the distance of each curve to the $25^\circ C$ one. We use the semidistance function defined as:

$$D(P, Q) = \int_{I_Q \cap I_P} [P(x) - Q(x)]^2 dx \quad (9.2)$$

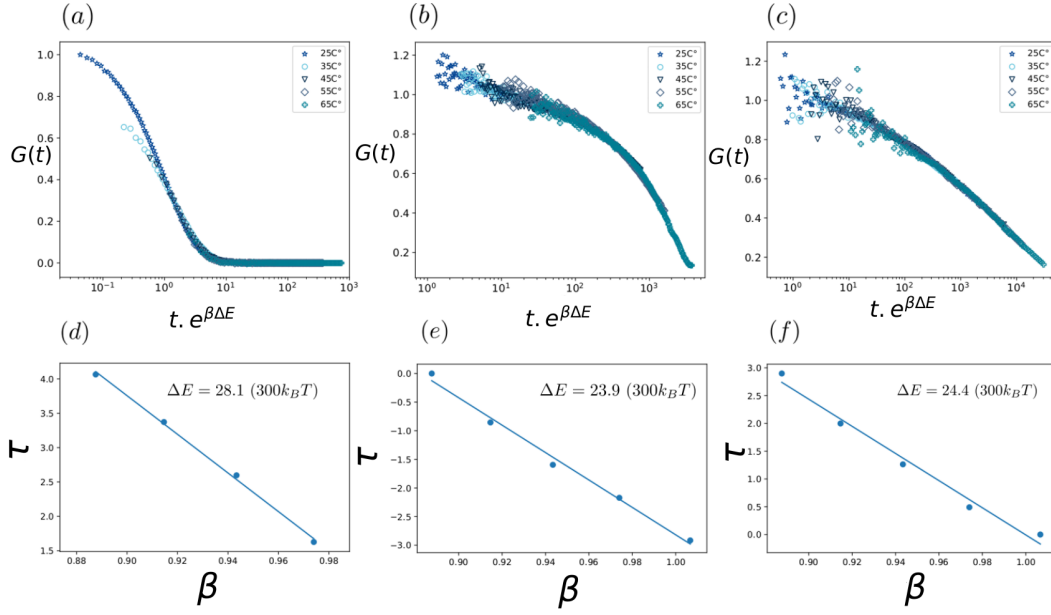


Figure 9.1: **Collapse of the relaxation modulus:** (a-c) respectively the collapsed relaxation modulus of Fe^{3+} , PolyMOC, nanoparticles after the rescaling of the time for an optimized collapse. (d-f) corresponding rescaling parameters as a function of $1/(k_B T)$ the inverse temperature. The slope of the line is $-\Delta E$, the result is given as a legend.

where I_Q and I_P are respectively the interval of definition of each function P and Q . However, the data sets are discrete measurements, and the rescaling of the time induces a mismatch of the time interval between different curves, which means that the evaluation of the two functions P and Q in Eq (9.2) at the same point is impossible. Therefore, the discrete computation of the integral is impossible. To overcome this issue, we start by fitting each experimental curve using a very high degree polynomial and compute the distance between the two fitting polynomials. Minimizing each distance with the 25°C curve gives the collapsed data (see data in Fig 9.1) as well as the set of parameters $\{a_i\}$. The optimized rescaling coefficients are then plotted as a function of the inverse temperature $1/k_B T$. The series of points is fitted with a line to verify the predicted emergence of an energy scale: $a(T_i) = \Delta E/k_B T_i$ consistent with our prediction. The binding energy ΔE is the slope of the fitted line. We observe a very good agreement with the expectation of a time-temperature rescaling through a binding energy. This further validates the assumption that the stress relaxation in the gel is a local process, involving a single energy scale.

9.3 Fit the master curve

The three remaining parameters τ_0 , P_{off} , \bar{N} are obtained by minimizing the squared distance between the experimental points and the fitting function. We start by fitting the collapsed curve for a temperature $T = 25^\circ C$. We then reverse the scaling from $t \rightarrow \tilde{t}e^{-\beta\Delta E}$ to obtain the fits given Fig 9.2. The corresponding values of the fitting parameters are given Table 9.1. The fits are in

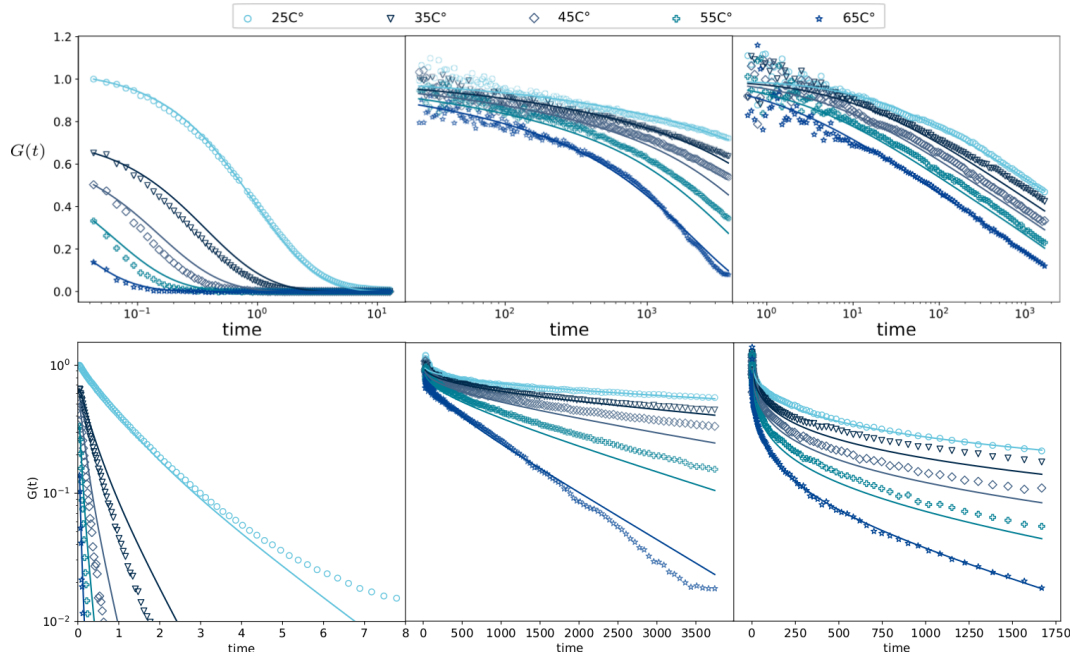


Figure 9.2: **Fits of the relaxation modulus** : We plot twice the same experimental data, with the associated fits, on different axis scales. From left to right, Fe^{3+} , PolyMOC, nanoparticle systems. The dots are experimental data, and the lines are the associated fitting curves. The top part, the lin-log scale, emphasizes the large interval of timescales involved. It is a characteristic of stretched exponential function. Such a coexistence of short, and long relaxation times, is a direct consequence of the exponential dependency of N on the relaxation time. Bottom part, the log-lin scale emphasizes the single exponential regime that appears as a straight line for long times. The nanoparticle and polyMOC system display two examples with the two regimes described: polymer concentration limited vs valency limited relaxation, in other words: collection of relaxation timescale vs single exponential regime.

good agreement with the experiments, with 4 adjustable parameters for 5 curves. More importantly, the model accurately captures what could be thought of as

two very different types of relaxation between the polyMOC and the nanoparticle systems. Most of the relaxation of the polyMOC system is exponential due to its low/intermediate valency, while most of the relaxation of the nanoparticles is happening through a collection of relaxation timescales. This difference translates into $N_{\text{cut}} < \bar{N}$ for polyMOC and $N_{\text{cut}} > \bar{N}$ for the nanoparticles.

Ion type	Fe^{3+}	PolyMOC	Nano particles
ΔE ($300k_B$)	28.11	23.94	24.42
P_{off}	0.05	0.02	0.31
τ_0 (s)	10^{-13}	4.10^{-10}	10^{-11}
\bar{N}	1.0	3.34	10
N_{cut}	1.	2.33	13.3
Valency	3	14	80

Table 9.1: **Value of the fitting parameters** : ΔE is close to the value obtained using stopped-flow techniques ($\Delta E_{\text{stopped flow}} = 36k_B T$). P_{off} is very small for both the ion and the PolyMOC system; as a reminder it corresponds to the probability for a polymer strands to be bound twice to the same crosslinker, which appears to be way more likely for a nanoparticle. The value of τ_0 is very small, as expected for a diffusion time over a nano-scale. We notice that \bar{N} is close to N_{cut} , which certainly results from the experimental adjustment to match the polymer concentration with ligand valency. N_{cut} and the valency are reminded for the comparison.

Conclusion

Our model focuses on the escape process of two crosslinks bound together by several polymers, while ignoring the physical entanglement of the polymer chains. The main assumptions made are a high energy barrier ($\beta\Delta E \gg 1$) for the binding of the polymer. With these assumptions, the maximum number of polymer chains that a crosslink can carry turns out to be the dominant parameter for the relaxation ($\tau_N \propto e^N$). The microscopic relaxation time scale can be limited by two phenomena that are both influenced by the valency of the crosslinkers. These two limiting factors -crosslink valency (N_{cut}) and polymer concentration (\bar{N})- translate into two distinct regimes in the relaxation modulus, both of which can be observed experimentally. On a more phenomenological level, we showed that it is possible to compare our model with the stretched exponential function by establishing a link between the parameter N_{cut} and the stretching exponent α . In theory, it is possible to cover the whole range of value of $\alpha \in [0, 1]$ by varying N_{cut}/\bar{N} . In practice, the concentration of polymer i.e. \bar{N} has to be adjusted to obtain a gel with a non-zero modulus. We are still able to identify two types of relaxation for $N_{cut} \gg \bar{N}$ and $N_{cut} \sim \bar{N}$. In the first case, most of the relaxation occurs through a superposition of many timescales. In the second one, a clear single exponential relaxation is observed for long-time. We show that these two regimes can be easily identified in an experiment by looking at the temperature dependence of the stretched exponent. As a proof of concept, we are able to visualize these two regimes in two different systems: the first scenario for nanoparticles and the second one for polyMOC.

Stretched exponential relaxation is observed in many physical systems [54, 76, 86], however, the origins of the stretched nature of the relaxation are as diverse as the systems. Despite the lack of microscopic models of the stretched exponential, it is usually associated with proliferating microscopic relaxation timescales.

In foam, for instance, the emergence of multiple time scales relies on non-local rearrangement of the system over regions of different lengthscales, called glassy dynamics [87]. It is possible to associate a distribution of timescales with this distribution of lengthscales. Instead, in our system, the origin of the wide spectrum of timescales comes from a local mechanism that we have modelled as a 1d random walk.

This mechanism should, in theory, apply to any gel with transient, multivalent crosslinkers, as is the case for most nanocomposite hydrogels that we have introduced section 6.1. For instance, we can imagine to extend these ideas to bio materials, such as actin gels. In the cell cytoskeleton, actin is also a crosslinked network that is known for exhibiting glassy rheology, suggesting a similar broad spectrum of relaxation timescales [76]. In some situations, actin can even be crosslinked with multivalent crosslinkers [88], although no experiment comparable to ours has been carried out in this case. More generally, we chose to use a Pois-

son distribution of bonds to model the heterogeneity in the system, but one can imagine using a different distribution. For instance, we showed section 8.5 that an exponential distribution leads to a relaxation of the stress according to a power law that corresponds to the observed behavior of cells' cytoskeleton [89].

Finally, the model we derived reveals two regimes of relaxation that we could have missed if we stuck with the stretched exponential model. In our situation, the second regime of relaxation originates from an upper bound of the distribution of relaxation timescale set by the size of the crosslinkers. This type of relaxation with two regimes has also been observed in other systems [90, 91]. Despite the origin of the relaxation being very different, the emergence of the two distinct regimes relies on an upper bound of the microscopic relaxation timescale. We expect that in some cases, the development of more refined models for explaining non-exponential relaxation can shed light on new phenomenologies, overshadowed by the stretched exponential model.

General conclusion

This thesis has been organized along a usual dichotomy in biophysics : practical problems that open the way for theoretical questions. Despite being two decoupled projects, each of the two parts aim to improve our understanding of how biological matter is organized. The first does so by focusing on the mechanisms of self-assembly itself and the second by understanding the macroscopic effect of a specific microscopic organization.

In the first part, we established a link between the mesoscopic properties of assembling particles and the resulting aggregate structure. More precisely, we exposed two phenomena : the influence of a relaxation layer of the stress at the boundary of an aggregate on its equilibrium size, and the influence of the incompressibility of the particles on the aggregate's structure. The first one is well understood within the framework of our model, but its generalization to random particles remains limited. Indeed, we have not been able yet to establish a clear link between the mechanical properties of the random particle and the emergence of the relaxation layer. Preliminary work presented section 5.2, suggests that many modes of deformation are candidates for relaxing stress at the boundary of the aggregate. Among those, the softest should dominate, as it gives rise to the largest relaxation layer. In future work, we expect to be able to identify such a mode and to predict the emergence of the boundary relaxation layer from the mechanical characteristics of the random particle. Concerning the influence of the incompressibility of the particles, the correlation between fiber formation and high ν completely drops when considering random particles. However, we must point out that the Poisson ratio considered in the continuum limit is associated with the two elastic sheets. If incompressible sheets imply incompressible particles, the reciprocal relation is not true. Finally, using model-independent mechanical characteristics – such as bulk modulus and Poisson ratio – to predict the emergence of self-limited aggregation or fiber formation would allow for an application to experimental systems.

The second part of the thesis aimed at understanding the influence of the valency of large crosslinkers on the relaxation of hydrogels. The initial motivation for this project originates from an engineering query, as the valency of the crosslinkers is an experimentally well-defined parameter. Beyond its influence on the relaxation of the gel, the valency of the crosslinkers also affects the gelation process of the gel. When preparing the gel, the ratio of the concentration of crosslinkers over the polymers' one must be precisely adjusted to match a fixed ratio of binding sites per polymer. On the one hand, a deficit in polymers reduces the connectivity of the network and ultimately leads the resulting gel's shear modulus to vanish. On the other hand, a deficit in nanoparticles leads to a phase separation into a phase rich in polymer and a gel one. The concentration of the polymer at which

this phase separation occurs depends on the valency of the crosslinkers, suggesting that the phase separation is driven by the binding of polymers to the crosslinkers. A quantitative theory of equilibrium phase separation driven by transient binding would be valuable from an experimental point of view.

Bibliography

- [1] Tuomas P. J. Knowles, Michele Vendruscolo, and Christopher M. Dobson. The amyloid state and its association with protein misfolding diseases. *Nature reviews Molecular cell biology*, 2014.
- [2] Joseph A. Marsh and Sarah A. Teichmann. Structure, dynamics, assembly, and evolution of protein complexes. *Annual Review of Biochemistry*, 2015.
- [3] Shanshan Cheng and Charles L Brooks III. Viral capsid proteins are segregated in structural fold space. *PLoS computational biology*, 9(2):e1002905, 2013.
- [4] Robijn F Bruinsma and William S Klug. Physics of viral shells. *Annu. Rev. Condens. Matter Phys.*, 6(1):245–268, 2015.
- [5] Donald LD Caspar and Aaron Klug. Physical principles in the construction of regular viruses. In *Cold Spring Harbor symposia on quantitative biology*, volume 27, pages 1–24. Cold Spring Harbor Laboratory Press, 1962.
- [6] Kenneth W. Adolph and Butler P Jonathan G. Assembly of a spherical plant virus. *Philosophical Transactions of the Royal Society of London. B, Biological Sciences*, 276(943):113–122, 1976.
- [7] Adam Zlotnick. To build a virus capsid: an equilibrium model of the self assembly of polyhedral protein complexes. *Journal of molecular biology*, 241(1):59–67, 1994.
- [8] Luigi E Perotti, Ankush Aggarwal, Joseph Rudnick, Robijn Bruinsma, and William S Klug. Elasticity theory of the maturation of viral capsids. *Journal of the Mechanics and Physics of Solids*, 77:86–108, 2015.
- [9] Nidhi Pashine. Local rules for fabricating allosteric networks. *arXiv preprint arXiv:2101.06793*, 2021.

- [10] Jordan M Fletcher, Robert L Harniman, Frederick RH Barnes, Aimee L Boyle, Andrew Collins, Judith Mantell, Thomas H Sharp, Massimo Antognozzi, Paula J Booth, Noah Linden, et al. Self-assembling cages from coiled-coil peptide modules. *Science*, 340(6132):595–599, 2013.
- [11] Jeanette Nangreave, Dongran Han, Yan Liu, and Hao Yan. Dna origami: a history and current perspective. *Current opinion in chemical biology*, 14(5):608–615, 2010.
- [12] Christian Sigl, Elena M. Willner, and Wouter Engelen et al. Programmable icosahedral shell system for virus trapping. *Nature materials*, 2021.
- [13] Yin Zhang, Angus McMullen, Lea-Laetitia Pontani, Xiaojin He, Ruojie Sha, Nadrian C Seeman, Jasna Brujic, and Paul M Chaikin. Sequential self-assembly of dna functionalized droplets. *Nature communications*, 8(1):1–7, 2017.
- [14] Stef AJ van der Meulen and Mirjam E Leunissen. Solid colloids with surface-mobile dna linkers. *Journal of the American Chemical Society*, 135(40):15129–15134, 2013.
- [15] Zorana Zeravcic, Vinothan N Manoharan, and Michael P Brenner. Size limits of self-assembled colloidal structures made using specific interactions. *Proceedings of the National Academy of Sciences*, 111(45):15918–15923, 2014.
- [16] Avinoam Ben-Shaul and William M Gelbart. *Statistical thermodynamics of amphiphile self-assembly: structure and phase transitions in micellar solutions*. Springer, 1994.
- [17] Michael F. Hagan and Gregory M. Grason. Equilibrium mechanisms of self-limiting assembly. *Rev. Mod. Phys.*, 93:025008, Jun 2021.
- [18] Emanuela Bianchi, Julio Largo, Piero Tartaglia, Emanuela Zaccarelli, and Francesco Sciortino. Phase diagram of patchy colloids: Towards empty liquids. *Physical Review Letters*, 97(16):168301, 2006.
- [19] Francesco Sciortino and Emanuela Zaccarelli. Reversible gels of patchy particles. *Current Opinion in Solid State and Materials Science*, 15(6):246–253, 2011. Functional Gels and Membranes.
- [20] Zhenli Zhang and Sharon C. Glotzer. Self-assembly of patchy particles. *NANO LETTERS*, 2004.

- [21] Francesco Sciortino, Stefano Mossa, Emanuela Zaccarelli, and Piero Tartaglia. Equilibrium cluster phases and low-density arrested disordered states: The role of short-range attraction and long-range repulsion. *Phys. Rev. Lett.*, 93:055701, Jul 2004.
- [22] Francesco Sciortino, Piero Tartaglia, and Emanuela Zaccarelli. One-dimensional cluster growth and branching gels in colloidal systems with short-range depletion attraction and screened electrostatic repulsion. *The Journal of Physical Chemistry B*, 109(46):21942–21953, 2005. PMID: 16853852.
- [23] Jan Groenewold and Willem K. Kegel. Anomalously large equilibrium clusters of colloids. *The Journal of Physical Chemistry B*, 105(47):11702–11709, 2001.
- [24] Yangkun Du, Chaofeng Lü, Michel Destrade, and Weiqiu Chen. Influence of initial residual stress on growth and pattern creation for a layered aorta. *Scientific reports*, 9(1):1–9, 2019.
- [25] Gabriel Helmlinger, Paolo A Netti, Hera C Lichtenbeld, Robert J Melder, and Rakesh K Jain. Solid stress inhibits the growth of multicellular tumor spheroids. *Nature biotechnology*, 15(8):778–783, 1997.
- [26] David C Wright and N David Mermin. Crystalline liquids: the blue phases. *Reviews of Modern physics*, 61(2):385, 1989.
- [27] L. D. LANDAU and E. M. LIFSHITZ. *Theory of elasticity*. 1986.
- [28] Guangnan Meng, Jayson Paulose, David R Nelson, and Vinothan N Manoharan. Elastic instability of a crystal growing on a curved surface. *Science*, 343(6171):634–637, 2014.
- [29] Snir Meiri and Efi Efrati. Cumulative geometric frustration in physical assemblies. *arXiv*, 2021.
- [30] Pierre Ronceray and Bruno Le Floch. The range of geometrical frustration in lattice spin models. *Phys Rev E*, 2019.
- [31] Gregory M Grason. Misfits unite. *Nature Physics*, 13(12):1149–1150, 2017.
- [32] Gregory M. Grason. Chiral and achiral mechanisms of self-limiting, twisted bundle assembly. *Soft Matter*, 2019.
- [33] Gregory M. Grason. Perspective: Geometrically frustrated assemblies. *The Journal of Chemical Physics*, 2016.

- [34] Efi Efrati, Eran Sharon, and Raz Kupferman c. The metric description of elasticity in residually stressed soft materials. *Soft Matter review*, 2013.
- [35] Philippe G. Ciarlet. *AN INTRODUCTION TO DIFFERENTIAL GEOMETRY WITH APPLICATIONS TO ELASTICITY*. Springer, 2005.
- [36] Mingming Zhang, Doron Grossman, Dganit Danino, and Eran Sharon. Shape and fluctuations of frustrated self-assembled nano ribbons. *nat com*, 2019.
- [37] Gregory M. Grason. Frustration and packing in curved-filament assemblies: from isometric to isomorphic bundles. *Soft Matter*, 9:6761–6772, 2013.
- [38] Shahaf Armon, Hillel Aharoni, Michael Moshe, and Eran Sharon. Shape selection in chiral ribbons: from seed pods to supramolecular assemblies. *Soft matter*, 10(16):2733–2740, 2014.
- [39] Frank A Ferrone and Hofrichter. The polymerization of sickle hemoglobin in solutions and cells. *Experientia*, 49(2):110–117, 1993.
- [40] Rebecca Nelson and David Eisenberg. Structural models of amyloid-like fibrils. *Advances in protein chemistry*, 73:235–282, 2006.
- [41] Liam D Aubrey, Ben JF Blakeman, Liisa Lutter, Christopher J Serpell, Mick F Tuite, Louise C Serpell, and Wei-Feng Xue. Quantification of amyloid fibril polymorphism by nano-morphometry reveals the individuality of filament assembly. *Communications Chemistry*, 3(1):1–10, 2020.
- [42] Martin Lenz and Thomas A Witten. Geometrical frustration yields fibre formation in self-assembly. *Nature physics*, 13(11):1100–1104, 2017.
- [43] Branko Grünbaum and Geoffrey C Shephard. Tilings by regular polygons. *Mathematics Magazine*, 50(5):227–247, 1977.
- [44] Craig Rottman and Michael Wortis. Statistical mechanics of equilibrium crystal shapes: Interfacial phase diagrams and phase transitions. *Physics Reports*, 103(1):59–79, 1984.
- [45] Hyunjune Sebastian Seung and David R Nelson. Defects in flexible membranes with crystalline order. *Physical Review A*, 38(2):1005, 1988.
- [46] Iwan Jensen and Anthony J Guttmann. Statistics of lattice animals (polyominoes) and polygons. *Journal of Physics A: Mathematical and General*, 33(29):L257, 2000.

- [47] Miranda Lundy and Alistair Mees. Convergence of an annealing algorithm. *Mathematical programming*, 34(1):111–124, 1986.
- [48] Arti Vashist, Ajeet Kaushik, Anujit Ghosal, Jyoti Bala, Roozbeh Nikkhah-Moshaie, Waseem A Wani, Pandiaraj Manickam, and Madhavan Nair. Nanocomposite hydrogels: advances in nanofillers used for nanomedicine. *Gels*, 4(3):75, 2018.
- [49] Can Hui Yang, Mei Xiang Wang, Hussain Haider, Jian Hai Yang, Jeong-Yun Sun, Yong Mei Chen, Jinxiong Zhou, and Zhigang Suo. Strengthening alginate/polyacrylamide hydrogels using various multivalent cations. *ACS applied materials & interfaces*, 5(21):10418–10422, 2013.
- [50] Niels Holten-Andersen, Matthew J Harrington, Henrik Birkedal, Bruce P Lee, Phillip B Messersmith, Ka Yee C Lee, and J Herbert Waite. pH-induced metal-ligand cross-links inspired by mussel yield self-healing polymer networks with near-covalent elastic moduli. *Proceedings of the National Academy of Sciences*, 108(7):2651–2655, 2011.
- [51] Shengtong Sun, Li-Bo Mao, Zhouyue Lei, Shu-Hong Yu, and Helmut Cölfen. Hydrogels from amorphous calcium carbonate and polyacrylic acid: bio-inspired materials for “mineral plastics”. *Angewandte Chemie International Edition*, 55(39):11765–11769, 2016.
- [52] ML Oyen. Mechanical characterisation of hydrogel materials. *International Materials Reviews*, 59(1):44–59, 2014.
- [53] Laurence Ramos and Christian Ligoure. Structure of a new type of transient network: Entangled wormlike micelles bridged by telechelic polymers. *Macromolecules*, 40(4):1248–1251, 2007.
- [54] Olivier Ronsin, C Caroli, and Tristan Baumberger. Glass-like dynamics of the strain-induced coil/helix transition on a permanent polymer network. *The Journal of chemical physics*, 144(6):064904, 2016.
- [55] Ana C Borges, Christian Eyholzer, Fabien Duc, Pierre-Etienne Bourban, Philippe Tingaut, Tanja Zimmermann, Dominique P Pioletti, and Jan-Anders E Månson. Nanofibrillated cellulose composite hydrogel for the replacement of the nucleus pulposus. *Acta biomaterialia*, 7(9):3412–3421, 2011.
- [56] Ovijit Chaudhuri, Luo Gu, Max Darnell, Darinka Klumpers, Sidi A Bencherif, James C Weaver, Nathaniel Huebsch, and David J Mooney. Substrate stress relaxation regulates cell spreading. *Nature communications*, 6(1):1–7, 2015.

- [57] Davoud Mozhdehi, James A Neal, Scott C Grindy, Yves Cordeau, Sergio Ayala, Niels Holten-Andersen, and Zhibin Guan. Tuning dynamic mechanical response in metallopolymer networks through simultaneous control of structural and temporal properties of the networks. *Macromolecules*, 49(17):6310–6321, 2016.
- [58] Michael P Howard, Zachary M Sherman, Adithya N Sreenivasan, Stephanie A Valenzuela, Eric V Anslyn, Delia J Milliron, and Thomas M Truskett. Effects of linker flexibility on phase behavior and structure of linked colloidal gels. *The Journal of Chemical Physics*, 154(7):074901, 2021.
- [59] Qigang Wang, Justin L Mynar, Masaru Yoshida, Eunji Lee, Myongsoo Lee, Kou Okuro, Kazushi Kinbara, and Takuzo Aida. High-water-content mouldable hydrogels by mixing clay and a dendritic molecular binder. *Nature*, 463(7279):339–343, 2010.
- [60] Jun Fu. Strong and tough hydrogels crosslinked by multi-functional polymer colloids. *Journal of Polymer Science Part B: Polymer Physics*, 56(19):1336–1350, 2018.
- [61] Georg E Fantner, Emin Oroudjev, Georg Schitter, Laura S Golde, Philipp Thurner, Marquesa M Finch, Patricia Turner, Thomas Gutsmann, Daniel E Morse, Helen Hansma, et al. Sacrificial bonds and hidden length: unraveling molecular mesostructures in tough materials. *Biophysical journal*, 90(4):1411–1418, 2006.
- [62] Scott C Grindy, Robert Learsch, Davoud Mozhdehi, Jing Cheng, Devin G Barrett, Zhibin Guan, Phillip B Messersmith, and Niels Holten-Andersen. Control of hierarchical polymer mechanics with bioinspired metal-coordination dynamics. *Nature materials*, 14(12):1210–1216, 2015.
- [63] Francisco J Martinez-Veracoechea and Daan Frenkel. Designing super selectivity in multivalent nano-particle binding. *Proceedings of the National Academy of Sciences*, 108(27):10963–10968, 2011.
- [64] Yin Zhang, Xiaojin He, Rebecca Zhuo, Ruojie Sha, Jasna Brujic, Nadrian C Seeman, and Paul M Chaikin. Multivalent, multiflavored droplets by design. *Proceedings of the National Academy of Sciences*, 115(37):9086–9091, 2018.
- [65] Andreas Herrmann. Dynamic combinatorial/covalent chemistry: a tool to read, generate and modulate the bioactivity of compounds and compound mixtures. *Chemical Society Reviews*, 43(6):1899–1933, 2014.

- [66] Aleksandr V Zhukhovitskiy, Mingjiang Zhong, Eric G Keeler, Vladimir K Michaelis, Jessie EP Sun, Michael JA Hore, Darrin J Pochan, Robert G Griffin, Adam P Willard, and Jeremiah A Johnson. Highly branched and loop-rich gels via formation of metal–organic cages linked by polymers. *Nature chemistry*, 8(1):33–41, 2016.
- [67] Udo Seifert. Rupture of multiple parallel molecular bonds under dynamic loading. *Physical Review Letters*, 84(12):2750, 2000.
- [68] German Alberto Parada and Xuanhe Zhao. Ideal reversible polymer networks. *Soft Matter*, 14(25):5186–5196, 2018.
- [69] Fumihide Tanaka and Samuel Frederick Edwards. Viscoelastic properties of physically crosslinked networks: Part 1. non-linear stationary viscoelasticity. *Journal of Non-Newtonian Fluid Mechanics*, 43(2-3):247–271, 1992.
- [70] Shengchang Tang and Bradley D Olsen. Relaxation processes in supramolecular metallogels based on histidine–nickel coordination bonds. *Macromolecules*, 49(23):9163–9175, 2016.
- [71] Donghua Xu and Stephen L Craig. Scaling laws in supramolecular polymer networks. *Macromolecules*, 44(13):5465–5472, 2011.
- [72] Jean-Philippe Bouchaud. Anomalous relaxation in complex systems: from stretched to compressed exponentials. *Anomalous Transport*, pages 327–345, 2008.
- [73] Jack F Douglas and Joseph B Hubbard. Semiempirical theory of relaxation: Concentrated polymer solution dynamics. *Macromolecules*, 24(11):3163–3177, 1991.
- [74] Alessandra Bonfanti, Jonathan Louis Kaplan, Guillaume Charras, and Alexandre Kabla. Fractional viscoelastic models for power-law materials. *Soft Matter*, 16(26):6002–6020, 2020.
- [75] Richard G Palmer, Daniel L Stein, Elihu Abrahams, and Philip Warren Anderson. Models of hierarchically constrained dynamics for glassy relaxation. *Physical Review Letters*, 53(10):958, 1984.
- [76] Yuval Mulla, FC MacKintosh, and Gijsje H Koenderink. Origin of slow stress relaxation in the cytoskeleton. *Physical Review Letters*, 122(21):218102, 2019.
- [77] Charles R Clark. A stopped-flow kinetics experiment for advanced undergraduate laboratories: formation of iron (iii) thiocyanate. *Journal of chemical education*, 74(10):1214, 1997.

- [78] Masao DOI and Samuel Frederick EDWARDS. *The Theory of Polymer Dynamics*. CLARENDON PRESS, 1994.
- [79] Nicolaas Godfried VAN KAMPEN. *STOCHASTIC PROCESSES IN PHYSICS AND CHEMISTRY*. Elsevier, 2007.
- [80] Pierre-Gilles De Gennes. Reptation of stars. *Journal de Physique*, 36(12):1199–1203, 1975.
- [81] GW Scott Blair and Jonathan Burnett. On the creep, recovery, relaxation and elastic "memory" of some renneted milk gels. *British Journal of Applied Physics*, 10(1):15, 1959.
- [82] Bavand Keshavarz, Thibaut Divoux, Sébastien Manneville, and Gareth H McKinley. Nonlinear viscoelasticity and generalized failure criterion for polymer gels. *ACS Macro Letters*, 6(7):663–667, 2017.
- [83] Martial Balland, Nicolas Desprat, Delphine Icard, Sophie Féréol, Atef Asnacios, Julien Browaeys, Sylvie Hénon, and François Gallet. Power laws in microrheology experiments on living cells: Comparative analysis and modeling. *Physical Review E*, 74(2):021911, 2006.
- [84] Michael et al. Kapnistos. Unexpected power-law stress relaxation of entangled ring polymers. *Nature materials*, 7(12):997–1002, 2008.
- [85] James Clerk Maxwell F.R.S. On the calculation of the equilibrium and stiffness of frames. *The London, Edinburgh, and Dublin Philosophical Magazine and Journal of Science*, 27(182):294–299, 1864.
- [86] Reinhard Höhler and Sylvie Cohen-Addad. Rheology of liquid foam. *Journal of Physics: Condensed Matter*, 17(41):R1041–R1069, sep 2005.
- [87] Alexandre Nicolas, Ezequiel E. Ferrero, Kirsten Martens, and Jean-Louis Barrat. Deformation and flow of amorphous solids: Insights from elastoplastic models. *Rev. Mod. Phys.*, 90:045006, Dec 2018.
- [88] Yunior Cabrales Fontela, Harindranath Kadavath, Jacek Biernat, Dietmar Riedel, Eckhard Mandelkow, and Markus Zweckstetter. Multivalent cross-linking of actin filaments and microtubules through the microtubule-associated protein tau. *Nature communications*, 8(1):1–12, 2017.
- [89] Ben Fabry, Geoffrey N Maksym, James P Butler, Michael Glogauer, Daniel Navajas, and Jeffrey J Fredberg. Scaling the microrheology of living cells. *Physical Review Letters*, 87(14):148102, 2001.

- [90] Christiane Caroli, Olivier Ronsin, and Anaël Lemaître. Glass-like stress relaxation of a permanent gelatin network as a signature of pretransitional helix-coil fluctuations. *The Journal of Chemical Physics*, 2018.
- [91] Kaori Nakaya-Yaegashi, Laurence Ramos, Hervé Tabuteau, and Christian Ligoure. Linear viscoelasticity of entangled wormlike micelles bridged by telechelic polymers: An experimental model for a double transient network. *Journal of Rheology*, 52(2):359–377, 2008.

Titre: Élasticité des bio-matériaux auto-assemblés

Mots clés: Rhéologie, auto-assemblage, élasticité, biophysique.

Résumé: Les systèmes biologiques sont entièrement auto-assemblés, à la fois à l'échelle moléculaire et cellulaire. Pour réussir la forme et la structure de chaque protéine par exemple, doit être précisément contrôlée. La moindre erreur conduit à des maladies telles qu'Alzheimer où des protéines s'agrègent entre elles pour former des structures fibreuses. À une échelle plus large les cellules ont besoin de sonder la réponse mécanique de leur environnement -la matrice extra cellulaire- et d'adapter leur propre rigidité pour être capables de s'orienter collectivement. Dans cette thèse nous étudions deux modèles différents. Dans la première partie, nous étudions l'agrégation de protéines au-delà des détails microscopiques. En considérant

l'assemblage de particules élastiques, nous sommes capables de comprendre la formation générique de structures fibreuses. Dans la seconde partie, nous modélisons la réponse dynamique d'une catégorie d'hydrogel qui suscite beaucoup d'intérêt en raison de leur compatibilité biologique. Les ingénieurs en matériaux sont aujourd'hui capables de synthétiser des matériaux aux propriétés surprenantes, néanmoins comprendre l'origine de ces propriétés émergentes peut s'avérer compliqué. Nous modélisons la réponse dynamique des hydrogels connectés par de gros agents réticulants multivalent. Ceci nous permet de reproduire les résultats expérimentaux et d'en comprendre l'origine.

Title: Elasticity of self assembling bio-materials

Keywords: Rheology, Elasticity, self-assembly, biophysics

Abstract: Self organization is crucial for the wealth of living systems, both at the molecular and cellular level. To correctly achieve their role, a tight control over the shape and structure of the protein, for instance, is required. Any mistake can lead to various diseases like Alzheimer, where proteins aggregate into fibrous structures. On a larger scale, cells need to probe the mechanical response of their environment -the extra cellular matrix- and to adapt their own rigidity to collectively orientate. In this thesis, we are looking at two different models. In the first part, we study protein aggregation beyond the microscopical details. By considering

elastic assembling particles, we are able to derive generic laws and understand the persistent formation of fibers. In the second part, we model the dynamical response of a fashionable class of hydrogels for their biocompatibility. Material engineers are now able to synthesize materials with more and more subtle behavior, although understanding certain emergent properties -such as non-exponential relaxation- can be a major challenge. We design a simple model for the dynamical response of hydrogels connected by large multivalent crosslinkers. We are able to account for experimental results, and rationalize their origin.